

Early Stages in Cosmic Structure Formation

by

Kristin M. Burgess

Submitted to the Department of Physics
in partial fulfillment of the requirements for the degree of

Doctor of Philosophy

at the

MASSACHUSETTS INSTITUTE OF TECHNOLOGY

September 2004

© Kristin M. Burgess, MMIV. All rights reserved.

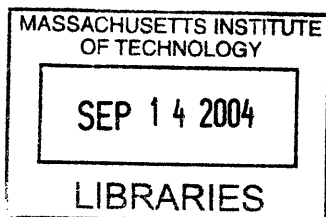
The author hereby grants to MIT permission to reproduce and distribute publicly
paper and electronic copies of this thesis document in whole or in part.

Author
Department of Physics
August 12, 2004

Certified by
Alan H. Guth
V. F. Weisskopf Professor of Physics
Thesis Supervisor

Certified by
Scott Burles
Assistant Professor
Thesis Supervisor

Accepted by
Thomas Greytak
Professor of Physics
Associate Department Head for Education



ARCHIVES :



Early Stages in Cosmic Structure Formation

by
Kristin M. Burgess

Submitted to the Department of Physics
on August 12, 2004, in partial fulfillment of the
requirements for the degree of
Doctor of Philosophy

Abstract

This thesis investigates the origin and evolution of large scale structure in the universe. We approach these questions from two different angles in two related but independent projects. The outcomes of these two investigations jointly contribute to our understanding of the large scale structure of the universe because the structures we see filling our universe today have their origins in the spectrum of density perturbations emerging from the inflationary era. The first project consists of two calculations of the density perturbation spectrum generated by a particular model of inflation called supernatural inflation. We compute the resulting power spectrum from a 1D numerical simulation and compare it with the predictions of an untested analytic approximation (Randall et al. 1996). We find that the results from these two calculations agree qualitatively. In the second project, using observations of the Lyman- α forest in the spectra of quasars, we characterize the redshift dependence of the flux probability distribution function of the Lyman- α forest in terms of an underlying lognormal model. We find that the lognormal model is good description of the underlying density distribution for redshifts $z > 3$. Our independent measurements of the optical depth agree with previous standard results.

Thesis Supervisor: Alan H. Guth
Title: V. F. Weisskopf Professor of Physics

Thesis Supervisor: Scott Burles
Title: Assistant Professor of Physics

Acknowledgments

There are many people at MIT who I owe thanks to for their help, support, advice, and unfaltering friendship. In particular I would like to thank:

My two fantastic advisors, Alan Guth and Scott Burles. My path through MIT has been circuitous, and at times a little unpredictable, but you have both given me invaluable guidance while still allowing me the freedom to chose my own direction. Alan, I cannot imagine anyone better to learn cosmology from than you, and I hope after all these years some of your beautiful physics intuition and impeccable attention to detail has worn off on me. Scott, you have done more to teach me how to be a sharp physicist than the rest of MIT combined and you have helped me to discover the astronomer inside me — I would not be where I am today without your help. I am fortunate to have found you both.

Several other physics professors also deserve special thanks. Ed Bertschinger, Paul Schechter, and Scott Hughes have been great sources of wisdom and advice. Each in your own way, you have all been additional mentors and advisors to me and you have made a difference in my life.

The postdocs and my fellow grad students are of course the daily source for help with whatever life unfolds. I especially want to thank Justin Kasper, Hsiao-Wen Chen, and Rob Simcoe for their endless stream of knowledge and their encouragement. Owing to my split personality in the physics department, there are many, many grad students who have been a large part of my experiences at MIT. In particular, Adam Bolton, Adrienne Juett, John Fregeau, Nick Morgan, Michelle Povinelli, and Yoav Bergner: life would have been much more difficult, and fewer a CBC beer enjoyed, without your companionship. Also, thank you to all the WIPs, past and present, for the tight community you provided all these years.

I am honored to have been supported by the Whiteman Fellowship for the last five years. With deep gratitude I would like to thank the sponsor of this fellowship, Dr. George Elbaum — I hope we stay in touch for years to come.

A huge thanks to my parents, and my most excellent brother Andreas, for their love and their unwavering encouragement. You are all the best family anyone could possibly have! And finally I want to thank Jim McBride, for everything and then some. You have given me more than I can possibly describe here, and I would be lost without you too.

Contents

List of Figures	8
List of Tables	9
Preface	10
1 The Inflationary Universe	13
1.1 The Dynamics of Inflation	13
1.1.1 Equations of Motion	14
1.1.2 Time Delay Formulation	14
1.1.3 The Power Spectrum	15
1.2 Supernatural Inflation	15
2 Density perturbations in Supernatural Inflation	17
2.1 Overview	17
2.2 Numerical Integration of the Mode Functions	17
2.2.1 Obtaining the Equations Governing Mode Function Evolution	19
2.2.2 The Initial Conditions	20
2.2.3 When to Begin the Integration?	23
2.3 Formalism of Constructing the Inflaton Field	24
2.3.1 Setup	25
2.3.2 Operator Normalization	26
2.4 The Monte Carlo Approach	29
2.4.1 Calculating $\phi(k, t)$ and $\phi(x, t)$	30
2.4.2 Advancing $\phi(x, t)$ in Time	30
2.4.3 Finding the Time Delay Field	32
2.4.4 The Power Spectrum in the Monte Carlo Case	32
2.5 The Analytic Approach	34
2.5.1 Calculating ϕ_{rms}	34
2.5.2 Calculating $\Delta\phi(k, t)$	35
2.5.3 The Power Spectrum in the Analytic Case	35
2.6 Comparing the Results of the Monte Carlo and Analytic Methods	35
3 Evolution of Structure in the Lyman-α Forest	39
3.1 The Lyman- α forest in the Spectra of Quasars	39
3.2 The SDSS Data Set	40
3.2.1 Normalizing by the Mean Spectrum	40
3.2.2 Correcting the SDSS Noise Estimates	41

3.2.3	The Flux Probability Distribution Function	42
3.3	The Lognormal Model	43
3.3.1	The Shape of the PDF	46
3.4	Fitting the Model	47
3.4.1	Generating Model Flux Points	48
3.4.2	Modeling the Noise	48
3.4.3	Applying a Signal to Noise Cut	49
3.5	Results of the Fit	50
3.6	Recovering Physical Parameters	72
3.6.1	Inferring $\sigma_{\ln}(z)$	72
3.6.2	Inferring $\tau_0(z)$	73
3.7	Conclusions	76
A	FFT Normalization Conventions	77
A.1	Setup	77
A.2	Monte Carlo Calculation	78
A.3	Analytic Approach	79
B	PCA Normalization	81
B.1	Useful Relations	81
B.2	Normalize Each Spectrum by its Median	81
B.3	Construct First Median Spectrum Template	81
B.4	Fit Median Template to Remove Tilt and Offset	82
B.5	Second Pass at Median Normalization and Fitting	83
B.6	Bspline to Construct Redshift-dependent Template	83
B.7	Third Pass at Fit Tilt and Offset, with Bspline Median	84
B.8	Do PCA Fit	84

List of Figures

1-1	The inflaton potential $V(\phi)$ for different values of the field ψ	16
2-1	Size of the leading six terms in the expansion of δR and $\delta\theta$	22
2-2	Integration starting time	23
2-3	Error from beginning integration too late	24
2-4	Modes approaching the common trajectory	31
2-5	Error in fit to common trajectory	32
2-6	Average trajectory and the resulting best fit.	33
2-7	An example time delay distribution	33
2-8	The final computed power spectra	36
2-9	The final computed power spectra, shifted	37
3-1	The Lyman- α forest region of a high-resolution quasar spectrum	40
3-2	Average χ^2 as a function of $\bar{\sigma}$	42
3-3	Example flux PDFs.	43
3-4	Number of pixels in each redshift bin	44
3-5	The shape of the flux PDF as the parameters in the model are varied.	47
3-6	Model flux PDF before and after adding noise	49
3-7	Signal to noise dependence of best fit values of A and B	50
3-8	χ^2 per degree of freedom for the best fit lognormal model	52
3-9	Best fit A and B for the fourth signal to noise quartile	53
3-10	The lognormal fit for $z \sim 2.2$	54
3-11	The lognormal fit for $z \sim 2.3$	55
3-12	The lognormal fit for $z \sim 2.4$	56
3-13	The lognormal fit for $z \sim 2.5$	57
3-14	The lognormal fit for $z \sim 2.6$	58
3-15	The lognormal fit for $z \sim 2.7$	59
3-16	The lognormal fit for $z \sim 2.8$	60
3-17	The lognormal fit for $z \sim 3.0$	61
3-18	The lognormal fit for $z \sim 3.1$	62
3-19	The lognormal fit for $z \sim 3.2$	63
3-20	The lognormal fit for $z \sim 3.4$	64
3-21	The lognormal fit for $z \sim 3.5$	65
3-22	The lognormal fit for $z \sim 3.7$	66
3-23	The lognormal fit for $z \sim 3.8$	67
3-24	The lognormal fit for $z \sim 4.0$	68
3-25	The lognormal fit for $z \sim 4.1$	69
3-26	The lognormal fit for $z \sim 4.3$	70

3-27	The lognormal fit for $z \sim 4.6$	71
3-28	Lognormal model parameter σ_{\ln} for the two limiting values of α	73
3-29	Lognormal model parameter τ_0 for the two limiting values of α	74
3-30	τ_0 and τ_{eff} , compared to other measurements	75
B-1	First median composite, median1	82
B-2	An example spectrum before and after tilt.	83
B-3	The difference between median1 and median2	84
B-4	An example spectrum at each stage in the normalization process.	86

List of Tables

2.1	Values of $\Delta\tau(k/H)$ for the Monte Carlo and analytic calculations	38
3.1	Redshift bin characteristics.	44
3.2	Best fit lognormal parameters and their errors	51
3.3	Derived values for τ_0 and σ_{\ln}	72

Preface

One of the most peculiar features of the observable universe as a whole is how it appears to be so smooth on very large scales and yet be filled with so much structure on smaller scales. The theory of inflation describes a period of rapid expansion in the very early universe and provides a possible explanation for the origin of both of these phenomena. Inflation's exponential expansion flattened away any initial inhomogeneity, while quantum fluctuations in the energy density were imprinted onto the density perturbation spectrum emerging from the inflationary phase and provided the seeds for large scale structure.

While the general predictions of inflationary theory are well-supported by current cosmological observations, the details of the theory and an understanding of the transition from the inflationary phase to the one we find the universe in today are not well understood. This thesis approaches these questions from two very different angles in two independent projects.

First, through detailed calculations of the density perturbation spectrum generated by a particular model of inflation called supernatural inflation we address the primordial origin of the fluctuations which give rise to observed large scale structure. This project is described in chapters 1 and 2.

Second, using observations of the Lyman- α forest in the spectra of quasars we study the subsequent evolution of the distribution of matter in the universe. In particular, we characterize the redshift dependence of the flux probability distribution function in the Lyman- α forest in terms of a simple underlying model for the density distribution. This project is described in chapter 3.

Chapter 1

The Inflationary Universe

The theory of inflation (Guth 1981; Linde 1982) provides the most complete picture we have of the early universe and receives strong support from recent high-precision measurements of the cosmic microwave background (Spergel et al. 2003). Inflation is characterized by a period of rapid expansion in the very early (10^{-35} sec) universe. This type of expansion is caused by the repulsive gravity effects generated by a scalar field, often called the inflaton field. As the scalar field evolves, the universe is driven into a period of exponential expansion.

The inflationary picture has had remarkable success in explaining several key features of the universe. Inflation drives the universe towards an otherwise improbable flat geometry (critical density) and also smoothes out large scale inhomogeneities without the need for acausal physics. Additionally, inflation provides the seeds for large scale structure by imprinting quantum fluctuations in the spectrum of density perturbations emerging from the inflationary epoch. All these predictions are borne out in our observations of the cosmic microwave background.

Although the general predictions of inflation are supported by current cosmological observations, the exact mechanisms of the theory are not yet well understood. Many different inflationary models have been introduced, with substantial variation in the precise details, yet no single model has emerged with overwhelming acceptance. A major shortcoming of most inflationary models is known as the fine tuning problem: in order to guarantee sufficient inflation as well as the correct magnitude of density perturbations, parameters in the inflaton potential must be fixed at unnaturally small values (generically of order 10^{-12}). While nothing in the theory prevents this from being the case, without an accompanying explanation this seems uncomfortably implausible. Much work has gone into searching for viable mechanisms to generate this small parameter naturally.

1.1 The Dynamics of Inflation

In conventional inflationary models, inflation ends when the inflaton field rolls down the hill of its potential energy diagram. The field is subject to quantum fluctuations, however, which can be treated as small perturbations about the classical solution of the equations of motion. These perturbations imply that the field rolls slightly faster in some places than in others, resulting in differing amounts of inflation, and ultimately in density perturbations.

1.1.1 Equations of Motion

We work in de Sitter space described by the metric

$$ds^2 = g_{\mu\nu} dx^\mu dx^\nu = -dt^2 + e^{2Ht} dx^2 \quad (1.1)$$

where H is the expansion rate. The inflaton field $\phi(x, t)$ is described by the Lagrangian density for a single scalar field,

$$\mathcal{L} = e^{3Ht} \left[\frac{1}{2} \dot{\phi}^2 - \frac{1}{2} e^{-2Ht} (\nabla\phi)^2 - V(\phi) \right], \quad (1.2)$$

for some potential $V(\phi)$. The resulting equations of motion are

$$\ddot{\phi} + 3H\dot{\phi} - e^{-2Ht} \nabla^2 \phi = \frac{\partial V}{\partial \phi}. \quad (1.3)$$

1.1.2 Time Delay Formulation

To study the density perturbations generated by quantum fluctuations in the inflaton field we use the time-delay approach of Guth and Pi (1982, 1985). Begin by writing the field as the sum of a homogeneous (classical) term, ϕ_0 , and a quantum fluctuation, $\delta\phi$,

$$\phi(x, t) = \phi_0(t) + \delta\phi(x, t). \quad (1.4)$$

Substituting this expression into Eq. (1.3) we find that the homogeneous piece satisfies

$$\ddot{\phi}_0 + 3H\dot{\phi}_0 = \left. \frac{\partial V}{\partial \phi} \right|_{\phi_0}. \quad (1.5)$$

Taking the time derivative of Eq. (1.5) results in the relation

$$\ddot{\phi}_0 + 3H\ddot{\phi}_0 = \dot{\phi}_0 \left. \frac{\partial^2 V}{\partial \phi^2} \right|_{\phi_0}. \quad (1.6)$$

Meanwhile, the perturbation satisfies

$$\ddot{\delta\phi} + 3H\dot{\delta\phi} - e^{-2Ht} \nabla^2 \delta\phi = \delta\phi \left. \frac{\partial^2 V}{\partial \phi^2} \right|_{\phi_0}. \quad (1.7)$$

The spatial gradient term in the above expression is exponentially damped and at late enough times will vanish; we will work in this limit. We now see that the time derivative of the homogeneous solution, $\dot{\phi}_0$, and the fluctuation, $\delta\phi$, satisfy the same differential equation:

$$\frac{d^2}{dt^2}(\dot{\phi}_0) + 3H \frac{d}{dt}(\dot{\phi}_0) = \dot{\phi}_0 \left. \frac{\partial^2 V}{\partial \phi^2} \right|_{\phi_0} \quad (1.8a)$$

$$\frac{d^2}{dt^2}(\delta\phi) + 3H \frac{d}{dt}(\delta\phi) = \delta\phi \left. \frac{\partial^2 V}{\partial \phi^2} \right|_{\phi_0}. \quad (1.8b)$$

The second order equation has two linearly independent solutions, but it can be shown that one of these solutions damps very quickly. Hence at late times both $\dot{\phi}_0$ and $\delta\phi$ are

proportional to the undamped solution, and are therefore proportional to each other. We choose to write the (time-independent, but position-dependent) proportionality factor as a time delay field $-\delta\tau(x)$, so that

$$\delta\phi(x, t) = -\delta\tau(x) \dot{\phi}_0(t). \quad (1.9)$$

In other words, to first order in $\delta\tau$, the effect of the fluctuations is to produce a position-dependent time delay in the evolution of the homogeneous field:

$$\phi(x, t) = \phi_0(t - \delta\tau(x)). \quad (1.10)$$

Thus, the problem of calculating the spectrum of perturbations in the inflaton field reduces to the (hopefully simpler) problem of calculating the distribution of time delays and making use of the relation in Eq. (1.9). It is important to remember that this is an asymptotic time delay defined for times sufficiently late that the spatial gradient term in Eq. (1.7) can be neglected.

1.1.3 The Power Spectrum

The relationship between the asymptotic time delay field at the end of inflation and the resulting density perturbation in the post-inflation universe is discussed by Guth and Pi (1982) and Olson (1976). Here we simply quote the results. The Fourier transform of the fluctuations of the density field are proportional to the Fourier transform of the time delay field,

$$\frac{\tilde{\delta\rho}}{\rho}(k) = 2\sqrt{2}H \delta\tilde{\tau}(k). \quad (1.11)$$

Typically, this expression is evaluated at the (k -dependent) time at which the particular wavenumber k is crossing the horizon (this is when the fluctuation will have frozen in).

We will define the power spectrum as the correlation function of the Fourier transform of the time delay field, $\Delta\tau(k)$, where the correlation function is defined as follows. Given a stochastic function $f(x)$, we measure the mean fluctuations of wavenumber k by

$$\Delta f(k) \equiv \left[\frac{k}{2\pi} \int dx e^{ikx} \langle f(x)f(0) \rangle \right]^{\frac{1}{2}}. \quad (1.12)$$

In Chapter 2 we calculate $\Delta\tau(k)$ for a model of inflation called supernatural inflation, and the above expression is applied to our particular case. The rest of the details will be deferred until that discussion.

1.2 Supernatural Inflation

Supernatural inflation is a supersymmetric hybrid inflationary model proposed in 1995 by Randall, Soljatic and Guth (Randall et al. 1996). This model attempts to solve the fine tuning problem by linking the small numbers in the inflationary potential to existing small parameters in theories of spontaneous supersymmetry breaking. As with other hybrid inflation models (Linde 1994), it becomes possible to separate the physics that determines

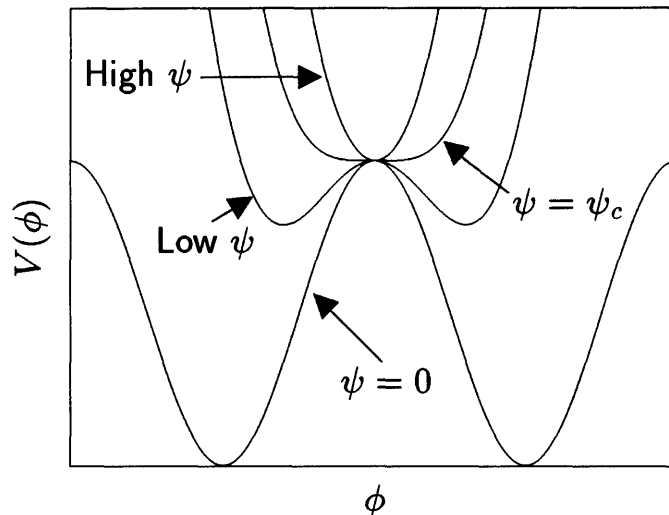


Figure 1-1: The inflaton potential $V(\phi)$ for different values of the field ψ .

the rate of exponential expansion and the physics that determines the magnitude of density perturbations.

Supernatural inflation accomplishes this through the use of two coupled scalar fields. In this case, the potential energy function of the inflaton field (ϕ) changes due to the evolution of a second field (ψ), behaving as though it had a time-dependent mass term (see Fig. 1-1). Initially, the inflaton field is at rest at the minimum of its potential energy function $V(\phi)$. But the evolution of the second field changes the qualitative shape of this potential energy function and the inflaton field eventually finds itself perched unstably atop a hill in the potential energy diagram. Quantum fluctuations then cause the inflaton field to roll down this hill. This results in fluctuations in the value of the field, and causes inflation to end at slightly different times in different places. It is in this way that inflation leads to spatial fluctuations in the energy density emerging from the inflationary phase.

But in contrast to other models where the dynamics of the scalar field can be treated classically, in the case of supernatural inflation the initial instability of the field is caused by quantum fluctuations. Thus the quantum fluctuations cannot be treated as small perturbations about a classical solution, and therefore new methods have to be developed. The problem of determining the variation in the amount of inflation from place to place becomes nonlinear, and the only known analytic estimates are based on untested approximations. Our work has focused on comparing these analytic estimates to numerical simulations of the theory.

Chapter 2

Density perturbations in Supernatural Inflation

2.1 Overview

In the original supernatural inflation paper (Randall et al. 1996) the authors made an untested approximation so as to be able to solve analytically for the density perturbations; the goal of this chapter is to test the validity of that approach. Traditionally one can solve for the fluctuations about the classical solution of the inflaton field, however for the present model there is no classical solution. The proposed idea is to let the RMS value of the fluctuations play the part of the classical variable. However, it is unclear how to quantify the validity of this approach, and so the intent of this project is to calculate numerically the perturbation spectrum and to compare with that obtained from this analytic method.

We can only do the numerical calculation in one dimension. However, if the ansatz holds in one dimension, so that the perturbation spectrum calculated analytically is consistent with the one computed numerically in one dimension, we have a substantial reason to believe the results it would give in three dimensions are also right. Throughout this Chapter we specialize all formulae to the particular case of one-dimension ($n_d = 1$) unless explicitly stated otherwise.

2.2 Numerical Integration of the Mode Functions

We assume a fixed background de Sitter space, with a scale factor given by

$$R(t) = e^{Ht} . \tag{2.1}$$

The scalar field ϕ is then described by the Lagrangian density

$$\mathcal{L}_\phi = e^{Ht} \left[\frac{1}{2} \dot{\phi}^2 - \frac{1}{2} e^{-2Ht} (\nabla\phi)^2 - \frac{1}{2} m_\phi^2(t) \phi^2 \right] \tag{2.2}$$

where we are allowing a time-dependent mass term. The mass is actually controlled by the ψ field, which in our approximation will also be described as a free scalar field, but this

time one with a fixed mass:

$$\mathcal{L}_\psi = e^{Ht} \left[\frac{1}{2} \dot{\psi}^2 - \frac{1}{2} e^{-2Ht} (\nabla \psi)^2 - \frac{1}{2} m_\psi^2 \psi^2 \right]. \quad (2.3)$$

The expressions for the Lagrangian densities are valid up to an additive constant, which is defined to have whatever value is needed to sustain a Hubble constant H . We will treat H as a constant.

The equations of motion for ϕ are given by

$$\frac{\partial}{\partial t} \left(\frac{\partial \mathcal{L}}{\partial \dot{\phi}} \right) + \frac{\partial}{\partial x^i} \left(\frac{\partial \mathcal{L}}{\partial (\partial_i \phi)} \right) = \frac{\partial \mathcal{L}}{\partial \phi} \quad (2.4a)$$

$$\frac{\partial}{\partial t} (e^{Ht} \dot{\phi}) - \frac{\partial}{\partial x^i} (e^{Ht} e^{-2Ht} \partial_i \phi) = -e^{Ht} m_\phi^2(t) \phi \quad (2.4b)$$

or finally

$$\ddot{\phi} + n_d H \dot{\phi} - e^{-2Ht} \nabla^2 \phi = -m_\phi^2(t) \phi. \quad (2.5)$$

Similarly,

$$\ddot{\psi} + n_d H \dot{\psi} - e^{-2Ht} \nabla^2 \psi = -m_\psi^2 \psi. \quad (2.6)$$

We approximate the ψ field as homogeneous and slow-rolling, so that the $\ddot{\psi}$ term is negligible, and therefore

$$\psi(t) = \text{const} \times e^{-(m_\psi^2/H)t}. \quad (2.7)$$

The value of the constant is arbitrary, since it merely fixes the origin of time. We choose the constant so that $\psi = \psi_c$ at $t = 0$, where ψ_c is the value of ψ such that $m_\phi^2(t) = 0$. Thus,

$$\psi(t) = \psi_c e^{-(m_\psi^2/n_d H)t}. \quad (2.8)$$

We switch to definitions in which H is scaled out,

$$N \equiv Ht, \quad (2.9)$$

$$\mu_\psi \equiv m_\psi/H, \quad (2.10)$$

and so

$$\psi(t) = \psi_c e^{-\mu_\psi^2 N}. \quad (2.11)$$

For notational convenience further define the quantity

$$\tilde{\mu}_\psi^2 \equiv r \left(\frac{1}{2} - \sqrt{\frac{1}{4} - \frac{m_\psi^2}{H^2}} \right). \quad (2.12)$$

We will take $m_\phi^2(t)$ to have a term proportional to ψ^r , where for the numerical simula-

tions we will take $r = 4$. We can then write

$$m_\phi^2(t) = -m_0^2 \left[1 - \left(\frac{\psi(t)}{\psi_c} \right)^r \right] \quad (2.13)$$

$$= -m_0^2 \left[1 - e^{-(r\mu_\psi^2 N)} \right]. \quad (2.14)$$

Scaling again by H , we define

$$\mu_\phi \equiv m_0/H. \quad (2.15)$$

2.2.1 Obtaining the Equations Governing Mode Function Evolution

We quantize the field following the formalism of Guth and Pi (1985). The setup of the lattice will be described in detail in section 2.3. As described more fully in that section, we expand the field $\phi(x, t)$ in terms of quantum creation and annihilation operators, and the mode functions $u(k, t)$. Eq. (2.40) defines the relation between the field $\phi(x, t)$, whose behavior is governed by its equation of motion Eq. (2.5), and the mode function $u(k, t)$, which we will numerically integrate.

The equation of motion for the mode function $u(k, t)$ is

$$\ddot{u} + \dot{u} + e^{-2N} \tilde{k}^2 u = \mu_\phi^2 \left[1 - e^{-\tilde{\mu}_\psi^2 N} \right] u \quad (2.16)$$

where the dimensionless wavenumber is

$$\tilde{k} \equiv \frac{|\vec{k}|}{H}. \quad (2.17)$$

We define the functions $R(k, t)$ and $\theta(r, t)$ such that

$$u(k, t) \equiv \frac{1}{\sqrt{2\tilde{k}H}} R(k, t) e^{i\theta(k, t)} \quad (2.18)$$

which allows us to separate the real and imaginary parts of the differential equation,

$$\ddot{R} - R\dot{\theta}^2 + \dot{R} + e^{-2N} \tilde{k}^2 R = \mu_\phi^2 \left[1 - e^{-\tilde{\mu}_\psi^2 N} \right] R, \quad (2.19a)$$

$$2i\dot{R}\dot{\theta} + iR\ddot{\theta} + iR\dot{\theta} = 0. \quad (2.19b)$$

The second equation can be integrated, and matched with the early time solution, to give an expression for $\dot{\theta}$

$$\dot{\theta} = -\frac{\tilde{k}e^{-N}}{R^2}, \quad (2.20)$$

which we substitute back into Eq. (2.19a) to give a single, second order differential equation for R :

$$\ddot{R} - \frac{e^{-2N} \tilde{k}^2}{R^3} + \dot{R} + e^{-2N} \tilde{k}^2 R = \mu_\phi^2 \left[1 - e^{-\tilde{\mu}_\psi^2 N} \right] R. \quad (2.21)$$

We would rather not solve a second order differential equation, so using Hamilton's

method we split this into two, coupled, first order equations. Let $\dot{R} \equiv S$, so that

$$\dot{S} = \ddot{R} = -\dot{R} + R \left[\mu_\phi^2 \left(1 - e^{-\tilde{\mu}_\psi^2 N} \right) - \tilde{k}^2 e^{-2N} \right] + \frac{\tilde{k}^2 e^{-2N}}{R^3}. \quad (2.22)$$

The equations to be solved are thus:

$$\frac{dR}{dN} = \dot{R} \quad (2.23a)$$

$$\frac{d\theta}{dN} = -\frac{\tilde{k}e^{-N}}{R^2}, \quad (2.23b)$$

$$\frac{d\dot{R}}{dN} = -\dot{R} + R \left[\mu_\phi^2 \left(1 - e^{-\tilde{\mu}_\psi^2 N} \right) - \tilde{k}^2 e^{-2N} \right] + \frac{\tilde{k}^2 e^{-2N}}{R^3}. \quad (2.23c)$$

Note that these equations are cast entirely in terms of dimensionless quantities. They completely specify the mode functions, as a function of time, once two initial conditions are specified; this is the topic of the next section.

2.2.2 The Initial Conditions

At early times the term proportional to \tilde{k}^2 in Eq. (2.16) dominates over the term proportional to μ_ϕ^2 . Dropping the latter results in a differential equation which has an analytic solution, so we use this asymptotic early-time solution as the initial condition for our numerical solution of the full equation.

The equation describing the early-time behavior is solved by a Bessel function. We evaluate the Bessel function at asymptotically early times and find that the initial condition for R is that

$$R(N \rightarrow -\infty) = 1. \quad (2.24)$$

However, to begin integrating early enough that this initial condition is accurate would require starting so early that the equation is difficult (and in some regimes impossible) to numerically integrate. The function R behaves like a simple harmonic oscillator with a time dependent spring constant — the spring gets stiffer and stiffer in the past, so that tiny perturbations about the minimum result in large oscillations. This in turn makes it even more important to start with the field precisely at the minimum of its potential, so the earlier you begin integrating the more accurate the initial condition must be.

We solve this problem by including higher order terms in the Taylor expansion of the early-time solution so that the initial condition is sufficiently accurate even at “late” times when it is straightforward to integrate Eq. (2.23). Let the solution at early-times be:

$$R(N) = 1 + \delta R(N) \quad (2.25)$$

and substitute this into Eq. (2.21). By a clever grouping of terms, one can generate successively higher order corrections to the initial condition Eq. (2.24). The expansion we work with is:

$$\delta R(N) = \delta R_{22} + \delta R_{24} + \delta R_{26} + \delta R_{44} + \delta R_{46} + \delta R_{66}. \quad (2.26)$$

Denoting terms by double subscripts, indicating the power of μ_ϕ and the power of e^N ,

respectively, these terms are found to be:

$$\delta R_{22} = \mu_\phi^2 \frac{e^{2N}}{4\tilde{k}^2} \left[1 - e^{-\tilde{\mu}_\psi^2 N} \right] \quad (2.27a)$$

$$\delta R_{24} = \mu_\phi^2 \frac{e^{4N}}{16\tilde{k}^4} \left[e^{-\tilde{\mu}_\psi^2 N} (2 - \tilde{\mu}_\psi^2)(3 - \tilde{\mu}_\psi^2) - 6 \right] \quad (2.27b)$$

$$\delta R_{26} = -\mu_\phi^2 \frac{e^{6N}}{64\tilde{k}^6} \left[e^{-\tilde{\mu}_\psi^2 N} (2 - \tilde{\mu}_\psi^2)(3 - \tilde{\mu}_\psi^2)(4 - \tilde{\mu}_\psi^2)(5 - \tilde{\mu}_\psi^2) - 120 \right] \quad (2.27c)$$

$$\delta R_{44} = 5\mu_\phi^4 \frac{e^{4N}}{32\tilde{k}^4} \left[1 - e^{-\tilde{\mu}_\psi^2 N} \right]^2 \quad (2.27d)$$

$$\delta R_{46} = -\mu_\phi^4 \frac{e^{6N}}{64\tilde{k}^6} \left[e^{-2\tilde{\mu}_\psi^2 N} (2 - \tilde{\mu}_\psi^2)(37 - 14\tilde{\mu}_\psi^2) - e^{-\tilde{\mu}_\psi^2 N} (148 - 65\tilde{\mu}_\psi^2 + 9\tilde{\mu}_\psi^4) + 74 \right] \quad (2.27e)$$

$$\delta R_{66} = 15\mu_\phi^6 \frac{e^{6N}}{128\tilde{k}^6} \left[1 - e^{-\tilde{\mu}_\psi^2 N} \right]^3. \quad (2.27f)$$

Note that this expansion is only valid in the region where $\delta R < 1$. However, truncating the series after only six terms would become a bad approximation long before this inequality is violated so in practice we do not need to worry about approaching this regime.

A similar procedure can be applied in the case of θ . From the Bessel function describing the asymptotic early-time solution we see that the initial condition for the angular component of the mode function is

$$\theta(N \rightarrow -\infty) = \tilde{k}e^{-N} - \pi/2. \quad (2.28)$$

Since the dynamics will not be affected by an overall phase redefinition, for simplicity we will drop the term $\pi/2$. As with R we expand the early-time solution as the asymptotic solution plus a correction

$$\theta(N) = e^{-N} \left(\tilde{k} + \delta\theta(N) \right) \quad (2.29a)$$

$$\simeq e^{-N} (\tilde{k} + \delta\theta_{22} + \delta\theta_{24} + \delta\theta_{44} + \delta\theta_{26} + \delta\theta_{46} + \delta\theta_{66}). \quad (2.29b)$$

At early times the differential equation for θ can be expanded as

$$\dot{\theta} = -\frac{\tilde{k}e^{-N}}{R^2} \quad (2.30a)$$

$$\simeq \tilde{k}e^{-N} (-1 + 2\delta R - 3\delta R^2 + 4\delta R^3) \quad (2.30b)$$

where in the last line we move the time dependence to the numerator by using the expansion

$$R^{-2} = (1 + \delta R)^{-2} = 1 - 2\delta R + 3\delta R^2 - 4\delta R^3 + \mathcal{O}(\delta R^4). \quad (2.31)$$

This can be integrated analytically after inserting the expansion for δR in Eq. (2.27). Using analogous notation to the previous case the leading terms are:

$$\delta\theta_{22} = \frac{\mu_\phi^2 e^{2N}}{2\tilde{k}} \left[1 - \frac{e^{-\tilde{\mu}_\psi^2 N}}{1 - \tilde{\mu}_\psi^2} \right] \quad (2.32a)$$

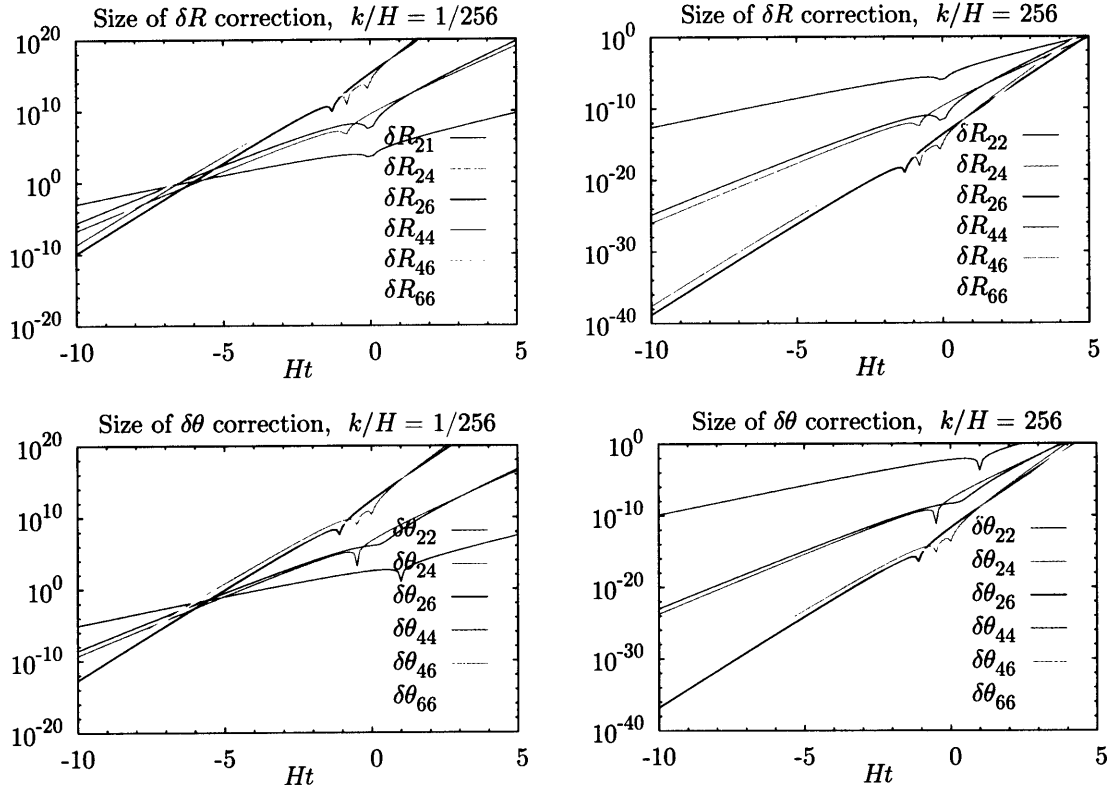


Figure 2-1: Size of the leading six terms in the expansion of δR and $\delta\theta$ for a representative small wavenumber $k/H = 0.004$ and large wavenumber $k/H = 256$.

$$\delta\theta_{24} = -\frac{\mu_\phi^2 e^{4N}}{8\tilde{k}^3} \left[2 - e^{-\tilde{\mu}_\psi^2 N} (2 - \tilde{\mu}_\psi^2) \right] \quad (2.32b)$$

$$\delta\theta_{44} = \frac{\mu_\phi^4 e^{4N}}{24\tilde{k}^3} \left[1 - \frac{6e^{-\tilde{\mu}_\psi^2 N}}{3 - \tilde{\mu}_\psi^2} + \frac{3e^{-2\tilde{\mu}_\psi^2 N}}{3 - 2\tilde{\mu}_\psi^2} \right] \quad (2.32c)$$

$$\delta\theta_{26} = -\frac{\mu_\phi^2 e^{6N}}{32\tilde{k}^5} \left[e^{-\tilde{\mu}_\psi^2 N} (2 - \tilde{\mu}_\psi^2)(3 - \tilde{\mu}_\psi^2)(4 - \tilde{\mu}_\psi^2) - 24 \right] \quad (2.32d)$$

$$\delta\theta_{46} = -\frac{\mu_\phi^4 e^{6N}}{160\tilde{k}^5} \left[56 - \frac{10e^{-\tilde{\mu}_\psi^2 N} (56 - 25\tilde{\mu}_\psi^2 + 3\tilde{\mu}_\psi^4)}{5 - \tilde{\mu}_\psi^2} + \frac{5e^{-2\tilde{\mu}_\psi^2 N} (2 - \tilde{\mu}_\psi^2)(28 - 11\tilde{\mu}_\psi^2)}{5 - 2\tilde{\mu}_\psi^2} \right] \quad (2.32e)$$

$$\delta\theta_{66} = \frac{\mu_\phi^6 e^{6N}}{80\tilde{k}^5} \left[1 - \frac{15e^{-N\tilde{\mu}_\psi^2}}{5 - \tilde{\mu}_\psi^2} + \frac{15e^{-2N\tilde{\mu}_\psi^2}}{5 - 2\tilde{\mu}_\psi^2} - \frac{5e^{-3N\tilde{\mu}_\psi^2}}{5 - 3\tilde{\mu}_\psi^2} \right]. \quad (2.32f)$$

The first six terms in the expansions for δR and $\delta\theta$ are plotted in Fig. 2-1.

The procedure is to determine R and θ by these formulae at early times when the expansions are sufficiently accurate, and then transition to numerical integration when the expansions begin to fail. The next section describes how to determine this transition time.

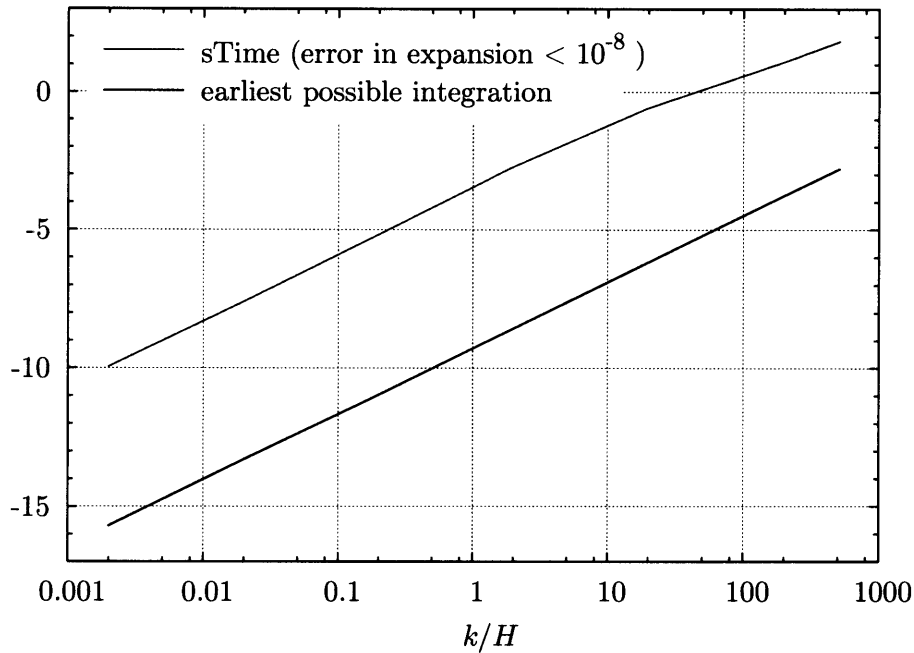


Figure 2-2: The transition time (`sTime`) after which the trajectories are computed by integration rather than by evaluating the initial condition expansion. Determined by finding the time the term $\delta\theta_{26}$ or $\delta R_{26} = 10^{-8}$. The “earliest possible integration time” is when the integrator first fails

2.2.3 When to Begin the Integration?

The corrections δR and $\delta\theta$ only provide a good approximation to the true solution of the mode function equation so long as the size of the correction is small, or more precisely, so long as the first omitted term in the expansion is negligible.

We determine the time when it necessary to transition to numerical integration by finding the time when the first neglected term reaches some specified value. In practice, we find that in the regime we are interested in the smallest of the six terms are δR_{26} and $\delta\theta_{26}$ (see Fig. 2-1; note that for the left-hand figures which show the low wavenumber, this transition time is well before the crossover around $Ht \sim -5$ when R_{26} ceases to be the smallest of the six terms). The size of the omitted term in each expansion is thus bounded by this value and so we locate the time when $\max[\delta R_{26}, \delta\theta_{26}]$ equals a predefined constant which we have chosen to be 10^{-8} . Fig. 2-2 shows, as a function of wavenumber, this time (which we call “`sTime`”) when it is necessary to transition to integration. Also shown in the figure is the earliest possible time the numerical integrator will function. Anytime between the two curves would be fine to use as the starting time, for computational efficiency we of course go with the latest acceptable time.

We aim for a numerical accuracy of 10^{-6} in the final determination of the power spectrum, so to be conservative we aim for an accuracy of 10^{-8} in the mode function integrations. For the function R this means we require the fractional error between the true solution and the numerically obtained solution to be $\Delta R/R < 10^{-8}$. In contrast, for the phase θ it is the absolute error $\Delta\theta < 10^{-8}$ that matters since it is the number modulo 2π which affects the dynamics.

Fig. 2-3 demonstrates that finding the trajectory by evaluating the early-time expan-

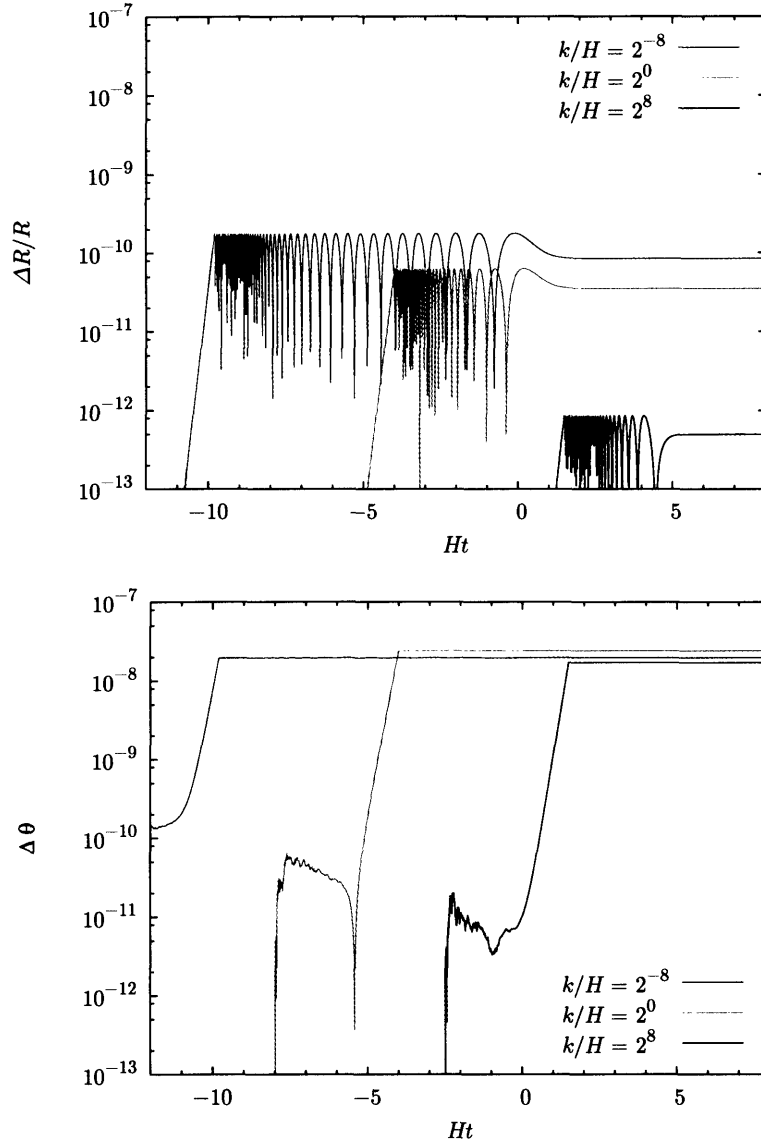


Figure 2-3: Errors in trajectories resulting from evaluating earlytime expansion for times earlier than $sTime$ rather than integrating directly. These curves resulted from setting the error tolerance (size of first neglected term) at 10^{-8} . The top plot shows the fractional error in R for a range of relevant modes, the bottom shows the absolute error in θ for the same modes.

sion up until the the time when $\max[\delta R_{26}, \delta\theta_{26}] = 10^{-8}$, then numerically integrating the remainder of the trajectory, is accurate to about one part in 10^8 compared to integrating the entire trajectory. In fact the $\delta\theta_{26}$ constraint is generally the more stringent of the two and so at $sTime$, δR_{26} is still smaller than 10^{-8} leading to an even smaller error in R .

2.3 Formalism of Constructing the Inflaton Field

We work on a one-dimensional lattice of fixed coordinate length b with Q independent points and periodic boundary conditions. This means that the position variables are restricted to

the locations

$$x_i = \frac{b}{Q} i \quad (2.33)$$

where the integer i which indexes the position can take on any of the Q values from 0 to $(Q - 1)$. Note that because of the boundary conditions, $x_0 = 0$ is identified with $x_Q = b$. In our calculation, Q will always be an even power of 2.

The corresponding allowed values for the wavenumber k are:

$$k_n = \frac{2\pi}{b} n \quad (2.34)$$

where the integer n can take on the Q values from $-\frac{Q}{2}$ to $(\frac{Q}{2} - 1)$. Again the periodic boundary condition identifies the first and last mode, $k_{-Q/2} = k_{Q/2}$, and we keep the former.

When it is necessary to convert between sums and integrals we use the relations

$$\int dx f(x) = \sum_x \Delta x f(x) = \left(\frac{b}{Q}\right) \sum_x f(x) \quad (2.35)$$

$$\int dk f(k) = \sum_k \Delta k f(k) = \left(\frac{2\pi}{b}\right) \sum_k f(k). \quad (2.36)$$

Our Fourier transform convention is

$$f(x) = \int dk e^{ikx} f(k) = \left(\frac{2\pi}{b}\right) \sum_k e^{ikx} f(k) \quad (2.37)$$

$$f(k) = \frac{1}{2\pi} \int dx e^{-ikx} f(x) = \left(\frac{1}{2\pi}\right) \left(\frac{b}{Q}\right) \sum_x e^{-ikx} f(x). \quad (2.38)$$

To convert to dimensionless quantities for the numerical calculation we measure the box size in Hubble lengths,

$$\tilde{b} \equiv bH, \quad (2.39)$$

when appropriate. Note that b is the coordinate (comoving) length of the box and so the physical size is equal to $b_{\text{phys}}(t) = be^{Ht}$.

2.3.1 Setup

For a complex scalar field $\phi(x, t)$ in one dimension

$$\phi(x, t) = \frac{1}{\sqrt{2\pi}} \left(\frac{2\pi}{b}\right)^{\frac{1}{2}} \sum_k \left[c(k) e^{ikx} u(k, t) + d^\dagger(k) e^{-ikx} u^*(k, t) \right]. \quad (2.40)$$

Here the summation over k is an abbreviation for summing from $n = -Q/2$ to $(Q - 2)/2$, the $u(k, t)$ are the mode functions computed in the previous section, and $c^\dagger(k)/c(k)$ and $d^\dagger(k)/d(k)$ are independent complex quantum mechanical creation/annihilation operators¹.

¹In the case of a real scalar field, the only difference is that d^\dagger would be replaced by c^\dagger in Eq. (2.41).

Note that the field $\phi(x, t)$ is dimensionless since u and \sqrt{b} have the same dimensions.

Since the sum is over both positive and negative values of k we are free to replace $-k \rightarrow k$ in the second term of the summation giving

$$\phi(x, t) = b^{-\frac{1}{2}} \sum_k e^{ikx} \left[c(k) u(k, t) + d^\dagger(-k) u^*(-k, t) \right]. \quad (2.41)$$

Now calculate the Fourier transform,

$$\phi(k, t) = \frac{1}{2\pi} \frac{b}{Q} \sum_x e^{-ikx} \phi(x, t) \quad (2.42a)$$

$$= \frac{1}{2\pi} \frac{b^{\frac{1}{2}}}{Q} \sum_x \sum_{k'} e^{-ikx} e^{ik'x} \left[c(k') u(k', t) + d^\dagger(-k') u^*(-k', t) \right] \quad (2.42b)$$

$$= \frac{1}{2\pi} \frac{b^{\frac{1}{2}}}{Q} \sum_{k'} Q \delta_{k, k'} \left[c(k') u(k', t) + d^\dagger(-k') u^*(-k', t) \right] \quad (2.42c)$$

$$= \frac{b^{\frac{1}{2}}}{2\pi} \left[c(k) u(k, t) + d^\dagger(-k) u^*(-k, t) \right]. \quad (2.42d)$$

Notice the following useful relation² obtained by equating the righthand sides of Eq. (2.42a) and Eq. (2.42d)

$$\frac{b^{\frac{1}{2}}}{Q} \sum_x e^{-ikx} \phi(x, t) = \left[c(k) u(k, t) + d^\dagger(-k) u^*(-k, t) \right]. \quad (2.43)$$

The field $\phi(k, t)$ has the dimensions of length. When we need it, the dimensionless version of this field will be:

$$\tilde{\phi}(k, t) \equiv H \phi(k, t). \quad (2.44)$$

2.3.2 Operator Normalization

We will now verify that as defined in Eq. (2.41) the quantum operators c and d are normalized correctly. We begin by finding an expression for $c(k)$. First, take the time derivative of Eq. (2.43)

$$\frac{b^{\frac{1}{2}}}{Q} \sum_x e^{-ikx} \dot{\phi}(x, t) = \left[c(k) \dot{u}(k, t) + d^\dagger(-k) \dot{u}^*(-k, t) \right]. \quad (2.45)$$

Next multiply Eq. (2.43) by $\dot{u}^*(-k, t)$ and Eq. (2.45) by $u^*(-k, t)$, and then subtract

$$\begin{aligned} \frac{b^{\frac{1}{2}}}{Q} \sum_x e^{-ikx} \left[\dot{u}^*(-k, t) \phi(x, t) - u^*(-k, t) \dot{\phi}(x, t) \right] = \\ c(k) \left[u(k, t) \dot{u}^*(-k, t) - \dot{u}(k, t) u^*(-k, t) \right]. \end{aligned} \quad (2.46)$$

It turns out that the quantity in the brackets on the right hand side is equal to the

²The following relations are also useful: $\sum_x e^{i(k-k')x} = Q \delta_{k, k'}$ and $\sum_k e^{i(x-x')k} = Q \delta_{x, x'}$.

Wronskian which we can calculate directly in this case. Following the method in Guth and Pi (1985), we consider the quantity

$$W(k, t) \equiv u(k, t) \frac{\partial u^*(-k, t)}{\partial t} - \frac{\partial u(k, t)}{\partial t} u^*(-k, t). \quad (2.47)$$

Then

$$\frac{\partial W(k, t)}{\partial t} = u(k, t) \frac{\partial^2 u^*(-k, t)}{\partial t^2} - \frac{\partial^2 u(k, t)}{\partial t^2} u^*(-k, t) \quad (2.48)$$

since the terms involving products of first derivatives cancel. Using Eq. (2.16) to replace the second derivatives, one finds

$$\frac{\partial W(k, t)}{\partial t} = -HW(k, t) \quad (2.49)$$

which is easily solved to give

$$W(k, t) = f(k)e^{-Ht} \quad (2.50)$$

where $f(k)$ is an arbitrary function of k .

Since $f(k)$ is independent of time, we can evaluate it for our choice of functions $u(k, t)$ by computing its value at asymptotically early times, when $u(k, t)$ is given by [I'm still missing the early-time DEQ equations]. Then using the Hankel function identity

$$H_\nu^{(1)}(z) \frac{d}{dz} H_\nu^{(2)}(z) - H_\nu^{(2)}(z) \frac{d}{dz} H_\nu^{(1)}(z) = -\frac{4i}{\pi z} \quad (2.51)$$

one finds for $k \neq 0$ that

$$W = ie^{-Ht}. \quad (2.52)$$

This is the one-dimensional analogue to the formula derived by Guth and Pi (1985) for the case $n_d = 3$, where they find $W = ie^{-3Ht}$.

We can now return to Eq. (2.46) and insert this expression for the bracketed term on the right hand side:

$$\frac{b^{\frac{1}{2}}}{Q} \sum_x e^{-ikx} \left[\dot{u}^*(-k, t) \phi(x, t) - u^*(-k, t) \dot{\phi}(x, t) \right] = c(k) \left[ie^{-Ht} \right]. \quad (2.53)$$

Thus,

$$c(k) = -ie^{Ht} \left(\frac{b^{\frac{1}{2}}}{Q} \right) \sum_x e^{-ikx} \left[\dot{u}^*(-k, t) \phi(x, t) - u^*(-k, t) \dot{\phi}(x, t) \right]. \quad (2.54)$$

We can apply a similar procedure to solve for the second operator,

$$d^\dagger(k) = ie^{Ht} \left(\frac{b^{\frac{1}{2}}}{Q} \right) \sum_x e^{ikx} \left[\dot{u}(-k, t) \phi(x, t) - u(-k, t) \dot{\phi}(x, t) \right], \quad (2.55)$$

or conjugating,

$$d(k) = -ie^{Ht} \left(\frac{b^{\frac{1}{2}}}{Q} \right) \sum_x e^{-ikx} \left[\dot{u}^*(-k, t) \phi^*(x, t) - u^*(-k, t) \dot{\phi}^*(x, t) \right]. \quad (2.56)$$

Note that $c(k)$ and $d(k)$ differ only in that $\phi \rightarrow \phi^*$.

We now verify that the normalization was chosen correctly by computing the various commutators. The Lagrangian density for the field $\phi(x, t)$ is:

$$\mathcal{L} = e^{Ht} \left[\dot{\phi}^* \dot{\phi} - e^{-2Ht} (\nabla \phi^*) (\nabla \phi) - m_\phi^2(t) |\phi^* \phi| \right]. \quad (2.57)$$

Note that the familiar factors of $\frac{1}{2}$ are missing, but that is simply because this is a complex field. It is equivalent to writing $\mathcal{L}(\phi) = \mathcal{L}(\varphi_1) + \mathcal{L}(\varphi_2)$ where $\phi = \frac{1}{\sqrt{2}}(\varphi_1 + i\varphi_2)$. Replacing the usual integral with a sum, we obtain the Lagrangian

$$L = e^{Ht} \left(\frac{b}{Q} \right) \sum_x \left[\dot{\phi}^* \dot{\phi} - e^{-2Ht} (\nabla \phi^*) (\nabla \phi) - m_\phi^2(t) |\phi^* \phi| \right]. \quad (2.58)$$

The canonical momentum for a complex field is given by

$$\pi(x) \equiv \frac{\partial L}{\partial \dot{\phi}(x)} = e^{Ht} \left(\frac{b}{Q} \right) \dot{\phi}^*(x). \quad (2.59)$$

The canonical commutator,

$$[\phi(x), \pi(x')] = i\delta_{x,x'}, \quad (2.60)$$

implies that

$$[\phi(x), \dot{\phi}^*(x')] = [\phi^*(x), \dot{\phi}(x')] = ie^{-Ht} \left(\frac{Q}{b} \right) \delta_{x,x'}. \quad (2.61)$$

For the complex field case we will need another variation of this commutator. Expanding out the field in terms of two independent real fields as before, $\phi = \frac{1}{\sqrt{2}}(\varphi_1 + i\varphi_2)$, we find

$$[\phi(x), \dot{\phi}^*(x')] = \phi \dot{\phi} - \dot{\phi} \phi \quad (2.62a)$$

$$= \frac{1}{2} \left((\varphi_1 + i\varphi_2)(\dot{\varphi}_1 + i\dot{\varphi}_2) - (\dot{\varphi}_1 + i\dot{\varphi}_2)(\varphi_1 + i\varphi_2) \right) \quad (2.62b)$$

$$= \frac{1}{2} \left([\varphi_1, \dot{\varphi}_1] - [\varphi_2, \dot{\varphi}_2] + i[\varphi_1, \dot{\varphi}_2] + i[\varphi_2, \dot{\varphi}_1] \right) \quad (2.62c)$$

$$= \frac{1}{2} \left([\varphi_1, \dot{\varphi}_1] - [\varphi_2, \dot{\varphi}_2] \right) \quad (2.62d)$$

$$= 0 \quad (2.62e)$$

where we have used the fact that the crossterm commutators vanish since the fields are independent.

We are now finally ready to compute the commutator of the creation/annihilation op-

erators. To simplify the following expressions we adopt the notation $u_{-k} \equiv u(-k, t)$.

$$[c(k), c^\dagger(k')] = e^{2Ht} \frac{b}{Q^2} \sum_{x, x'} e^{ik'x'} e^{-ikx} \left\{ (\dot{u}_{-k}^* \phi_x - u_{-k}^* \dot{\phi}_x) (\dot{u}_{-k'} \phi_{x'} - u_{-k'} \dot{\phi}_{x'}) - \right. \\ \left. (\dot{u}_{-k'} \phi_{x'} - u_{-k'} \dot{\phi}_{x'}) (\dot{u}_{-k}^* \phi_x - u_{-k}^* \dot{\phi}_x) \right\} \quad (2.63a)$$

$$= e^{2Ht} \frac{b}{Q^2} \sum_{x, x'} e^{ik'x'} e^{-ikx} \left(-u_{-k'} \dot{u}_{-k}^* [\phi_x, \dot{\phi}_{x'}] + \dot{u}_{-k'} u_{-k}^* [\phi_{x'}, \dot{\phi}_x] \right) \quad (2.63b)$$

$$= e^{2Ht} \frac{b}{Q^2} \sum_{x, x'} e^{ik'x'} e^{-ikx} \left(i e^{-Ht} \frac{Q}{b} \delta_{x, x'} \right) (-u_{-k'} \dot{u}_{-k}^* + \dot{u}_{-k'} u_{-k}^*) \quad (2.63c)$$

$$= i e^{Ht} \frac{1}{Q} \sum_x e^{i(k'-k)x} (-u_{-k'} \dot{u}_{-k}^* + \dot{u}_{-k'} u_{-k}^*) \quad (2.63d)$$

$$= i e^{Ht} \frac{1}{Q} \delta_{k, k'} Q (-i e^{-Ht}) \quad (2.63e)$$

$$= \delta_{k, k'}. \quad (2.63f)$$

In Eq. (2.63d) we again used the Wronskian³. Next compute the mixed term:

$$[c(k), d^\dagger(k')] = e^{2Ht} \frac{b}{Q^2} \sum_{x, x'} e^{ik'x'} e^{-ikx} \left\{ (\dot{u}_{-k}^* \phi_x - u_{-k}^* \dot{\phi}_x) (\dot{u}_{-k'} \phi_{x'} - u_{-k'} \dot{\phi}_{x'}) - \right. \\ \left. (\dot{u}_{-k'} \phi_{x'} - u_{-k'} \dot{\phi}_{x'}) (\dot{u}_{-k}^* \phi_x - u_{-k}^* \dot{\phi}_x) \right\} \quad (2.64a)$$

$$= e^{2Ht} \frac{b}{Q^2} \sum_{x, x'} e^{ik'x'} e^{-ikx} \left(-u_{-k'} \dot{u}_{-k}^* [\phi_x, \dot{\phi}_{x'}] + \dot{u}_{-k'} u_{-k}^* [\phi_{x'}, \dot{\phi}_x] \right) \quad (2.64b)$$

$$= 0 \quad (2.64c)$$

by Eq. (2.62). Applying a similar procedure to the remaining combinations, one finds that the other combinations also produce the expected result and we see that the normalization is indeed correct. In summary,

$$[c(k), c^\dagger(k')] = [d(k), d^\dagger(k')] = \delta_{k, k'} \quad (2.65)$$

$$[c(k), d(k')] = [c(k), d^\dagger(k')] = [c^\dagger(k), d(k')] = [c^\dagger(k), d^\dagger(k')] = 0. \quad (2.66)$$

2.4 The Monte Carlo Approach

In this section we calculate the time delay directly by following the individual mode trajectories.

³Note that $W(-k) = W(k)$ since in fact W does not depend on k .

2.4.1 Calculating $\phi(k, t)$ and $\phi(x, t)$

Having computed the value of each mode function u_k at a given time we construct $\phi(k, t)$ as follows.

The mode functions (Eq. (2.18)) are:

$$u(k, t) = \frac{R(k, t) e^{i\theta(k, t)}}{\sqrt{2|k|}}. \quad (2.67)$$

Note that the mode function only depends on the magnitude of k , so it is fine to replace $u(-k, t) \rightarrow u(k, t)$ and we have from Eq. (2.42)

$$\phi(k, t) = \frac{b^{\frac{1}{2}}}{2\pi} \left(c(k)u(k, t) + d^\dagger(-k)u^*(k, t) \right). \quad (2.68)$$

The quantum operators are formed from Gaussian random numbers (a_i),

$$c = a_1 + ia_2 \quad (2.69)$$

$$d^\dagger = a_3 - ia_4. \quad (2.70)$$

These random numbers are independent of time; a set of four a_i 's are drawn once for each k . They are chosen from a Gaussian distribution with width $\sigma = 0.5$, since the normalization of c gives: $1 = \langle \mathbf{0} | c^\dagger c | \mathbf{0} \rangle = \langle (a_1 - ia_2)(a_1 + ia_2) \rangle = \langle a_1^2 + a_2^2 \rangle = 2\langle a^2 \rangle$, resulting in $\langle a^2 \rangle = \frac{1}{2}$. After multiplying out all of the products and collecting real and imaginary terms, we find:

$$\Im[\phi(k, t)] = \frac{1}{2\pi} \sqrt{\frac{b}{2|k|}} R \left[(a_2 - a_4) \cos \theta + (a_1 - a_3) \sin \theta \right] \quad (2.71a)$$

$$\Re[\phi(k, t)] = \frac{1}{2\pi} \sqrt{\frac{b}{2|k|}} R \left[(a_1 + a_3) \cos \theta - (a_2 + a_4) \sin \theta \right]. \quad (2.71b)$$

The dimensionless counterparts, $\tilde{b} \equiv bH$, $\tilde{\phi}_k \equiv \phi_k H$, $\tilde{u} \equiv u\sqrt{H}$, and $N = Ht$ give

$$\Im[\tilde{\phi}(\tilde{k}, N)] = \frac{1}{2\pi} \sqrt{\frac{\tilde{b}}{2\tilde{k}}} R \left[(a_2 - a_4) \cos \theta + (a_1 - a_3) \sin \theta \right] \quad (2.72a)$$

$$\Re[\tilde{\phi}(\tilde{k}, N)] = \frac{1}{2\pi} \sqrt{\frac{\tilde{b}}{2\tilde{k}}} R \left[(a_1 + a_3) \cos \theta - (a_2 + a_4) \sin \theta \right]. \quad (2.72b)$$

To compute $|\phi(x, t)| \equiv \left(\Re[\phi(x, t)]^2 + \Im[\phi(x, t)]^2 \right)^{\frac{1}{2}}$ we use a standard fast Fourier transform routine from Numerical Recipes.

2.4.2 Advancing $\phi(x, t)$ in Time

The field $\phi(x, t)$ can be computed straightforwardly by computing the values of the mode functions u_k at a series of different times, then computing the FFT of the complex components of $\phi(k, t)$. Each new time step would require an additional FFT and knowledge of $\phi(x, t)$ at some previous time provides no help in finding the amplitude of the field at some new time owing to the non-linear dependence on k in the Fourier transform.

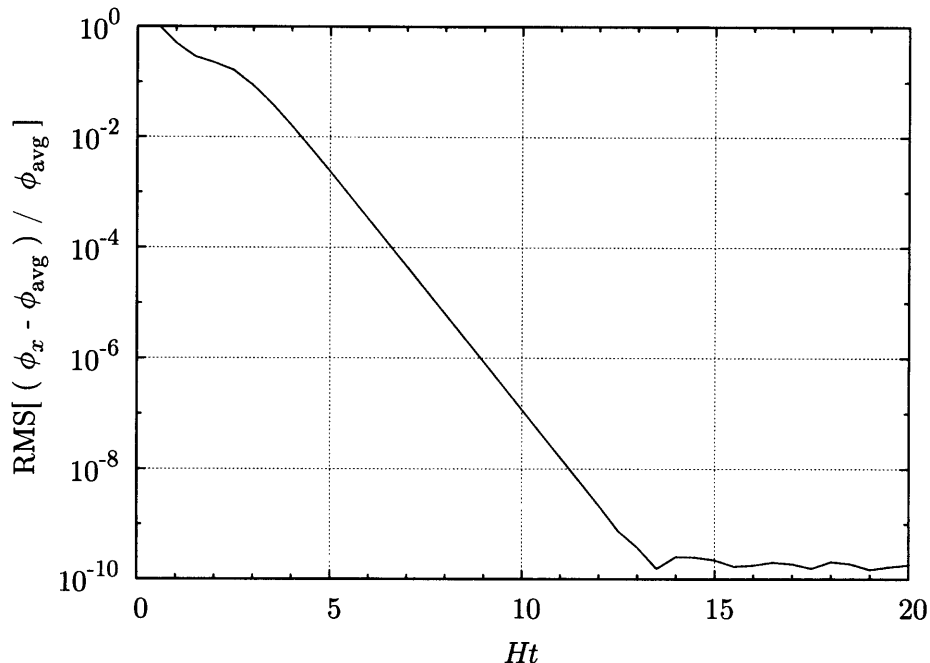


Figure 2-4: The RMS of the distribution of fractional errors between individual $\phi(x, t)$ trajectories and the average. We see that to high accuracy ($> 10^{-8}$) they have reached the common trajectory by a time of $N = 12$. Note that the flattening out after $N > 14$ is simply due to the fact that the trajectories were only saved to ten digits of precision.

However the situation in practice is significantly better. The k -dependence in the equation of motion (Eq. (2.16)) enters via a term proportional to e^{-2Ht} . This means that at late enough times the k -dependence drops out and from that point forward the modes evolve identically. Of course the amplitude of each mode function entering this regime will be a complicated function of the full k -dependent dynamics earlier on in the trajectory, but it means that at late enough times the subsequent behavior is quite simple (in fact, nearly exponential). Since the k -dependence drops out of u , it will also drop out of $\phi(x, t)$.

To be specific, for some time $N > N_{\text{late}}$ the field at each point x evolves via

$$\frac{\phi(x, N)}{\phi(x, N_{\text{late}})} = f(N), \text{ independent of } x. \quad (2.73)$$

The goal is to find both the function $f(N)$ and the time N_{late} after which $f(N)$ accurately advances $\phi(x, N_{\text{late}})$ forward in time. Once we know that, we simply need integrate each mode up to N_{late} , perform a single FFT, and then employ $f(N)$ to determine $\phi(x, N)$ at any subsequent time.

To determine this time when the trajectories reach the stage of k -independent evolution, compare various individual $\phi(x, t)$ trajectories to the average trajectory. The spread of values relative to this average field $\phi_{\text{avg}}(N) = \sum_x \phi(x, N)/Q$ decreases at time increases, and by a time of $N = 12$ the deviations are well within our tolerated error. Fig. 2-4 shows the evolution of this spread.

We determine the function $f(N)$ by fitting the exponential of a high order polynomial to the average trajectory $\phi_{\text{avg}}(N)$. To achieve an accuracy of 10^{-6} it turns out we need a

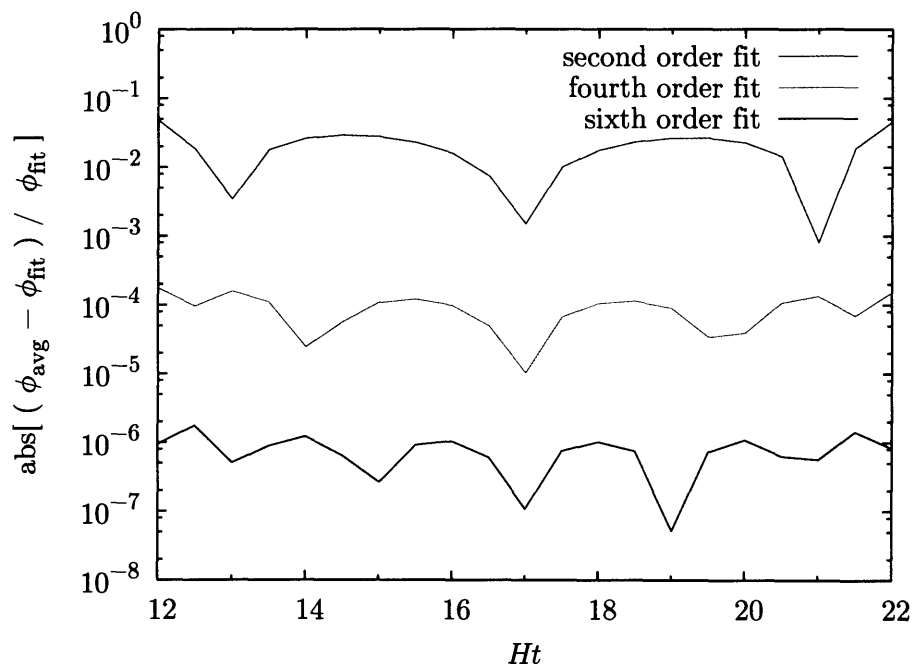


Figure 2-5: This is for fit performed over the range $N = 12 - 22$. Average absolute value of relative error is $< 10^{-6}$ in this range. Note that outside of this range the fit diverges and so it is not meant to be extended to later times.

sixth order polynomial,

$$f(N) = 10^{(c_0 + c_1 N + c_2 N^2 + c_3 N^3 + c_4 N^4 + c_5 N^5 + c_6 N^6)}. \quad (2.74)$$

Fig. 2-5 shows the accuracy attained using various order polynomials, and Fig. 2-6 shows the average trajectory and the resulting best fit.

2.4.3 Finding the Time Delay Field

As a result of the previous section, we can easily determine $\phi(x, t)$ at any late time. The next step is to compare the amplitude to the value of some specified constant ϕ_{end} which defines the “end” of inflation. The position-dependent time $\tau(x)$ when $|\phi(x, \tau)| = \phi_{\text{end}}$ is the desired time delay field.

What we actually need to do is invert the function in Eq. (2.74) so that given a value of $\phi(x, N_{\text{late}})$ it will return the time you would need to advance to in order for the amplitude to be equal to ϕ_{end} . This is done using a simple Newton-Raphson root finding routine. Fig. 2-7 shows an example distribution of time delays resulting from this procedure.

2.4.4 The Power Spectrum in the Monte Carlo Case

Functionally, each “run” will give a single instance of the time delay field $\tau(x)$ which we FFT to $\tau(k)$. We need many instances of $\tau(k)$ (each using a new set of random numbers) and then can find, as a function of k , the RMS value.

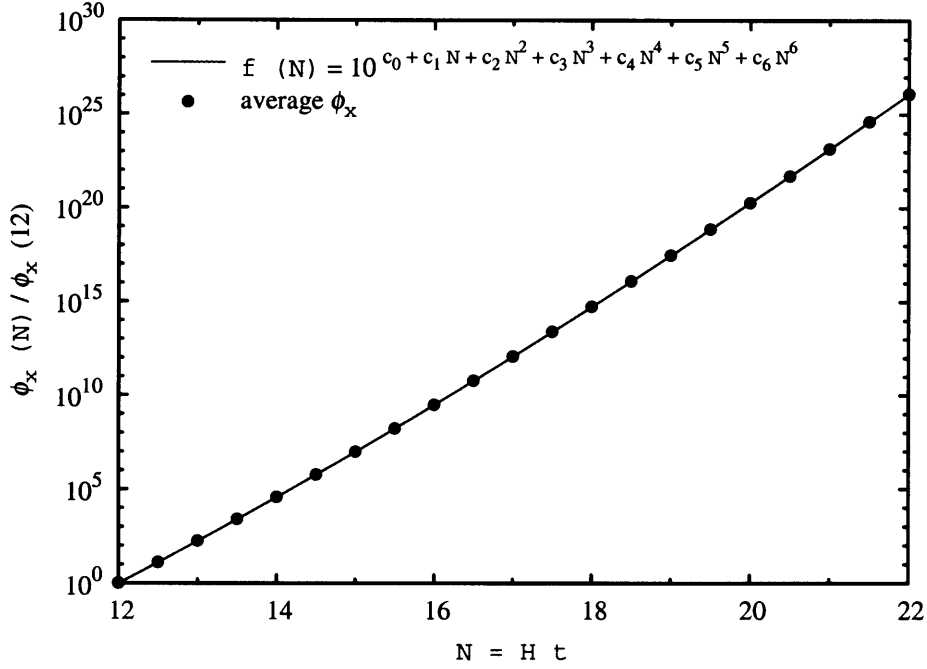


Figure 2-6: Average trajectory and the resulting best fit.

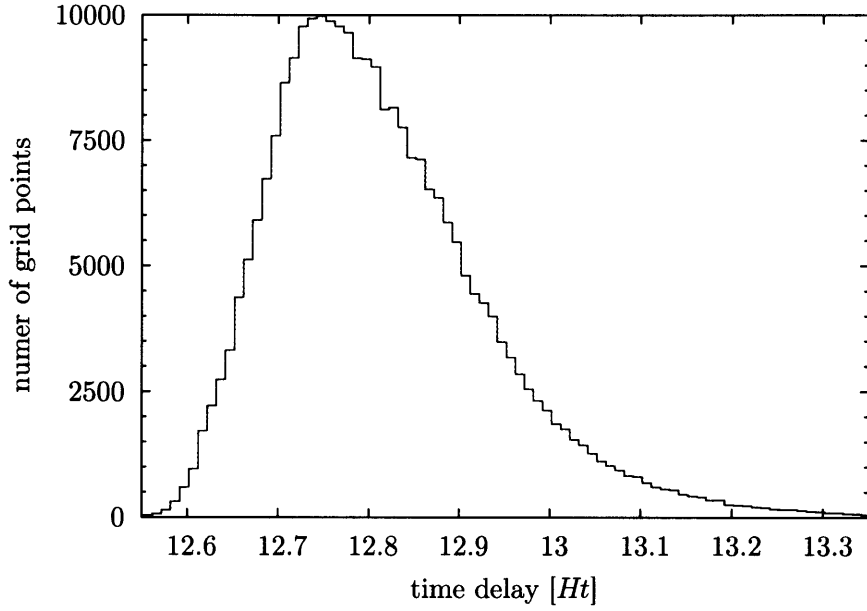


Figure 2-7: An example time delay distribution from a single run with a lattice size of $Q = 2^{18}$ points and $\phi_{\text{end}} = 10^{18}$.

The power spectrum derived using Monte Carlo approach is then computed by

$$\Delta\tau_{\text{mc}}(k) = \left[\frac{2\pi k}{b} \langle |\tau(k)|^2 \rangle \right]^{\frac{1}{2}}. \quad (2.75)$$

The derivation of this formula is given in Appendix A.

2.5 The Analytic Approach

Our goal is to compare the power spectrum obtained using the method described in the previous section with the power spectrum obtained using the analytic method described below.

2.5.1 Calculating ϕ_{rms}

In the analytic approach we let the RMS value of the classical wave packet play the role of the homogeneous solution $\phi_0(t)$ about which to study perturbations,

$$\phi_{\text{rms}}(t) \equiv \sqrt{\langle \phi^* \phi \rangle}. \quad (2.76)$$

This notation is shorthand for $\langle \mathbf{0} | \phi^*(x) \phi(x) | \mathbf{0} \rangle$ where $|\mathbf{0}\rangle$ is the vacuum state. We can use Eq. (2.41) to expand this expression:

$$\langle \phi^* \phi \rangle = b^{-1} \sum_k \sum_{k'} e^{-ikx} e^{ik'x} \langle \mathbf{0} | \left(c_k^\dagger u_k^* + d_{-k} u_{-k} \right) \left(c_{k'} u_{k'} + d_{-k'}^\dagger u_{-k'}^* \right) | \mathbf{0} \rangle. \quad (2.77)$$

The operators c and d are annihilation operators. Terms which contain an annihilation operator acting on the vacuum will vanish, $d|\mathbf{0}\rangle = 0$, and likewise $\langle \mathbf{0} | d^\dagger = \langle \mathbf{0} | d^\dagger = 0$. The only term in the expansion of the product that does not involve annihilating the vacuum is the term containing $d d^\dagger$ and we can use the commutator in Eq. (2.65) to reorder the operators:

$$\langle \mathbf{0} | \left(c_k^\dagger u_k^* + d_{-k} u_{-k} \right) \left(c_{k'} u_{k'} + d_{-k'}^\dagger u_{-k'}^* \right) | \mathbf{0} \rangle = u_k u_{k'}^* \langle \mathbf{0} | d_{-k} d_{-k'}^\dagger | \mathbf{0} \rangle \quad (2.78a)$$

$$= u_k u_{k'}^* \langle \mathbf{0} | \left[d_{-k}, d_{-k'}^\dagger \right] + d_{-k'}^\dagger d_{-k} | \mathbf{0} \rangle \quad (2.78b)$$

$$= u_k u_{k'}^* \langle \mathbf{0} | \delta_{-k, -k'} | \mathbf{0} \rangle \quad (2.78c)$$

$$= |u_k|^2 \delta_{k, k'}. \quad (2.78d)$$

Combining the two previous equations we find

$$\phi_{\text{rms}}(t) = \left(b^{-1} \sum_k |u(k, t)|^2 \right)^{\frac{1}{2}} = \left(\frac{1}{b} \sum_k \frac{R(k, t)^2}{2|k|} \right)^{\frac{1}{2}}. \quad (2.79)$$

Next we calculate the time derivative,

$$\dot{\phi}_{\text{rms}}(t) \equiv \frac{d\phi_{\text{rms}}}{dt} \quad (2.80a)$$

$$= \frac{1}{\sqrt{2b}} \frac{1}{2} \left(\sum_k \frac{R(k, t)^2}{|k|} \right)^{-\frac{1}{2}} \frac{d}{dt} \left(\sum_k \frac{R(k, t)^2}{|k|} \right) \quad (2.80b)$$

$$= \frac{1}{\sqrt{2b}} \left(\sum_k \frac{R(k, t)^2}{|k|} \right)^{-\frac{1}{2}} \left(\sum_k \frac{R(k, t) \dot{R}(k, t)}{|k|} \right). \quad (2.80c)$$

These sums can be carried out numerically from the same mode function integrations used in the Monte Carlo method.

2.5.2 Calculating $\Delta\phi(k, t)$

The final step is to calculate the correlation in the field $\phi(k, t)$. The details are given in Appendix A, and the result is

$$\Delta\phi(k) = \left[\frac{2\pi k}{b} \langle \phi^*(k) \phi(k) \rangle \right]^{\frac{1}{2}} = \frac{R(k, t)}{2\sqrt{\pi}}. \quad (2.81)$$

2.5.3 The Power Spectrum in the Analytic Case

Putting these results together we obtain

$$\Delta\tau_{\text{ana}}(k) = \frac{\Delta\phi(k, t)}{\dot{\phi}_{\text{rms}}(t)} \Big|_{t=t_{\text{end}}(k)} \quad (2.82a)$$

$$= \sqrt{\frac{b}{2\pi}} R(k, t_{\text{ana}}) \left(\sum_k \frac{R(k, t_{\text{ana}})^2}{|k|} \right)^{\frac{1}{2}} \left(\sum_k \frac{R(k, t_{\text{ana}}) \dot{R}(k, t_{\text{ana}})}{|k|} \right)^{-1}. \quad (2.82b)$$

The time that the right hand side should be evaluated at, t_{ana} , not entirely obvious. We use the mean time that inflation was found to “end” in the Monte Carlo simulation (which of course depends on ϕ_{end}). In practice the range of ending times is a narrow enough distribution that there is only a small change in the resulting power spectrum over this range of time.

2.6 Comparing the Results of the Monte Carlo and Analytic Methods

Fig. 2-8 shows the result of computing the power spectrum by each method. Numerical values are also listed in Table 2.1. The results agree qualitatively. The striking thing about the particular way the two curves disagree is that applying a multiplicative offset to both axes happens to align the curves to a remarkable degree. Fig. 2-9 shows the result of applying the transformation $k_{\text{shift}} = 2.19k$, and $\Delta\tau_{\text{shift}} = 0.625\Delta\tau$, to the analytic curve. We are actively investigating the connection between the parameters in the theory and the observed offset in hopes of understanding the physical root of the shift.

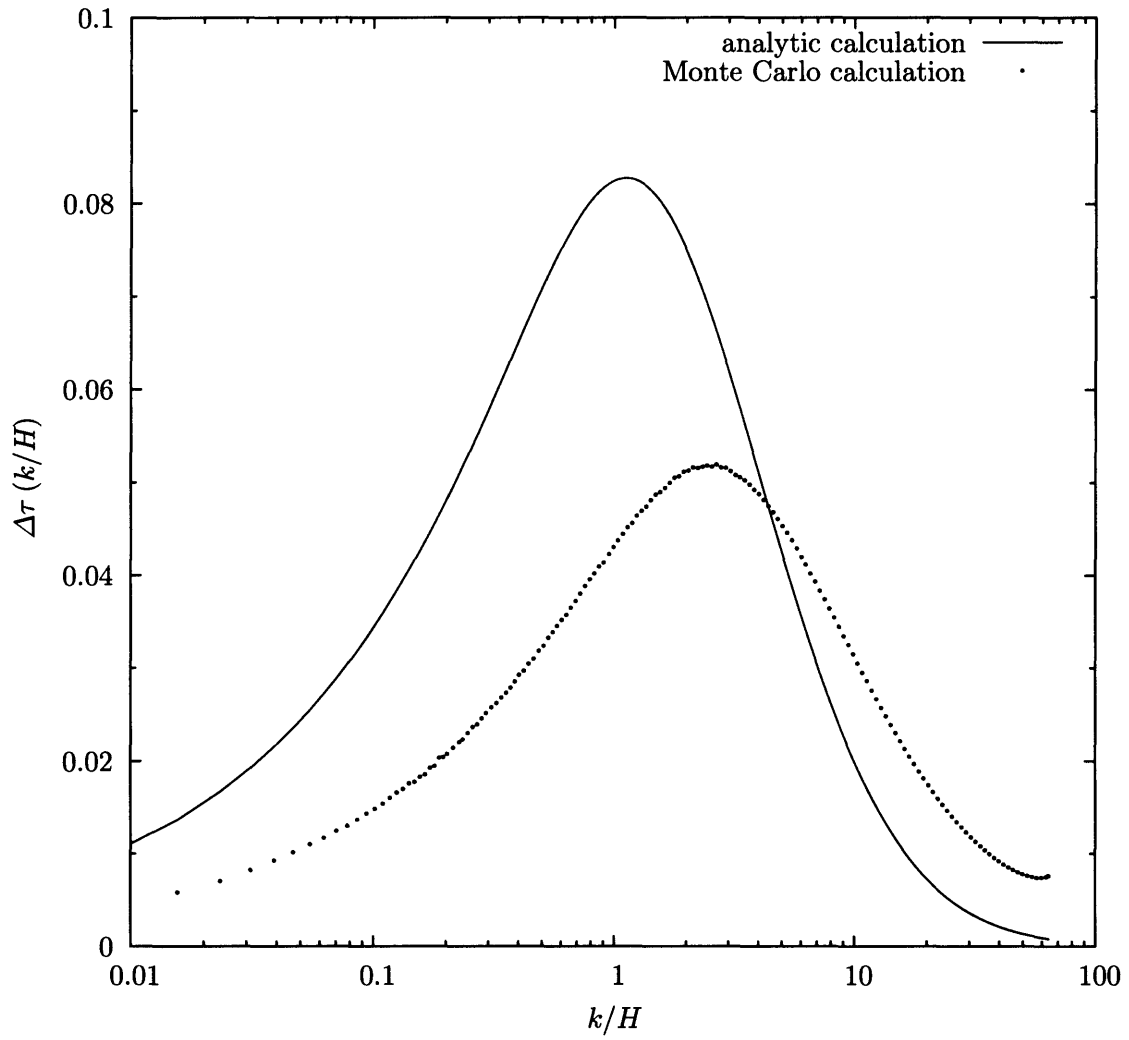


Figure 2-8: The final computed power spectra. These curves result from a lattice with $Q = 2^{18}$ points and the numerical simulation was run 5000 times and averaged.

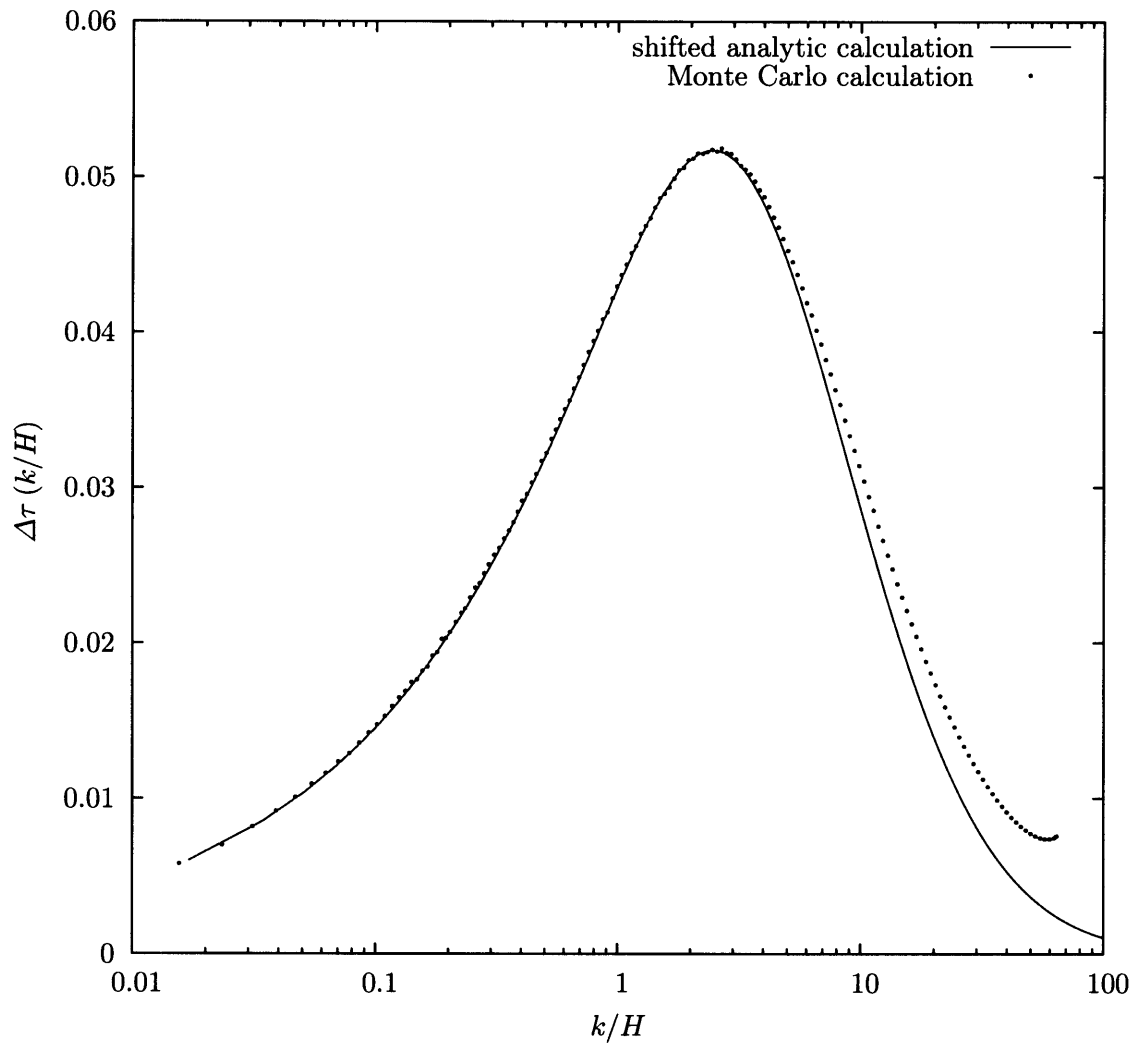


Figure 2-9: The result of shifting the analytic curve from Fig. 2-8 in log-space until the peaks line up and scaling the amplitude so the peak heights match: $k_{\text{shift}} = 2.19 k$, and $\Delta\tau_{\text{shift}} = 0.625 \Delta\tau$.

k/H	MC	analytic
0.0156	0.0059	0.0136
0.0234	0.0070	0.0167
0.0312	0.0083	0.0192
0.0428	0.0096	0.0225
0.0585	0.0112	0.0254
0.0741	0.0126	0.0288
0.0935	0.0143	0.0332
0.125	0.0165	0.0382
0.167	0.0187	0.0441
0.222	0.0216	0.0500
0.292	0.0250	0.0568
0.382	0.0282	0.0640
0.502	0.0324	0.0709
0.666	0.0364	0.0771
0.880	0.0409	0.0813
1.16	0.0452	0.0826
1.52	0.0488	0.0804
2.01	0.0512	0.0747
2.66	0.0517	0.0663
3.51	0.0499	0.0561
4.63	0.0466	0.0454
6.10	0.0416	0.0351
8.05	0.0358	0.0260
10.6	0.0298	0.0185
14.0	0.0240	0.0126
18.5	0.0189	0.0083
24.4	0.0146	0.0052
32.2	0.0111	0.0032
42.5	0.0087	0.0019
56.1	0.0075	0.0011

Table 2.1: Values of $\Delta\tau(k/H)$ for the Monte Carlo and analytic calculations. These values correspond to the results plotted in Fig. 2-8.

Chapter 3

Evolution of Structure in the Lyman- α Forest

Historically, galaxy surveys have provided one of the only observational windows into the evolution of large scale structure. Modern astronomical techniques have now broadened this window significantly, and observations of the Lyman- α forest are probing structure in the universe at an earlier epoch and over a range of scales never before accessible. This provides a crucial link between the complex structure of galaxy clusters today and the early, smooth universe predicted by inflation and measured in the cosmic microwave background. The Lyman- α forest is poised to play a central roll in understanding how our universe underwent this transition.

3.1 The Lyman- α forest in the Spectra of Quasars

The Lyman- α forest arises from the scattering of UV photons from a background QSO by neutral hydrogen along our line of sight. Photons with energy equal to the Lyman- α transition (1215.67Å) are readily absorbed by the intervening neutral hydrogen, but the absorption features are spread out in the observed spectra because the photons redshift as they travel through the expanding universe. Consequently, each line of sight presents a one-dimensional map of density fluctuations in the universe (Rauch 1998). An example spectrum is shown in Fig. 3-1.

The observed flux in the Lyman- α forest region of a QSO spectrum is dependent both on the initial QSO emission (the underlying QSO continuum) and on the subsequent absorption of some fraction of these photons by intervening matter. If one knew the underlying QSO continuum, then it would be straightforward to normalize the observed flux by this continuum flux (the flux that would have been observed had there been no absorption along the line of sight). This “continuum normalized flux”, f_c , is directly related to τ , the optical depth of the gas that is scattering the Lyman- α photons and that we wish to study,

$$f_c = e^{-\tau}. \quad (3.1)$$

Note that $f_c = 1$ corresponds to flux equal to the continuum flux, or no Lyman- α absorption by intervening matter and therefore vanishing optical depth, $\tau = 0$. On the other hand, $f_c = 0$ corresponds to no transmission and $\tau \rightarrow \infty$.

Unfortunately it is not possible to measure directly the underlying QSO continuum in

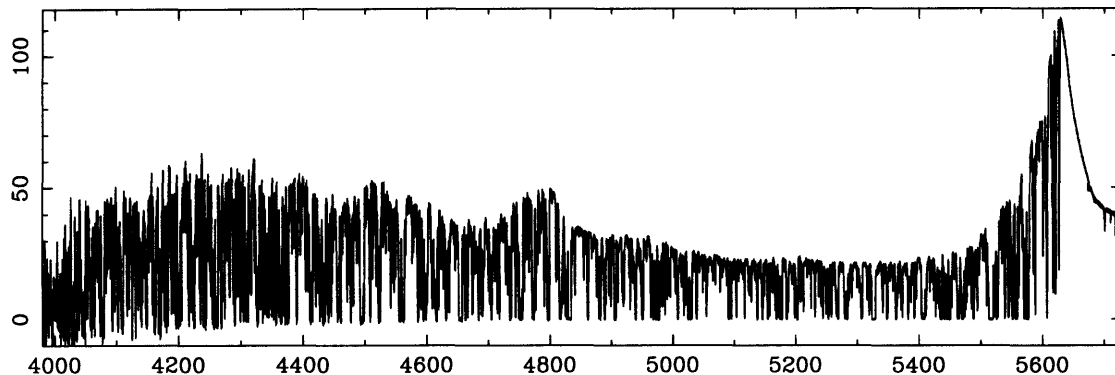


Figure 3-1: The Lyman- α forest region of a high-resolution quasar spectrum, $z_{\text{qso}} = 3.6$ (figure from Rauch (1998)). Flux is plotted versus observed wavelength [\AA].

the forest region, and so the above procedure is not nearly so straightforward to apply. The usual approach is to fit the slope of the continuum measured redward of Lyman- α , outside the region of the Lyman- α absorption (ie, to the right of the Lyman- α peak in Fig. 3-1), and then extrapolate this fit blueward of Lyman- α into the forest (for example, Croft et al. 2002; Bernardi et al. 2003). However, this method only provides an approximation to the true continuum and can easily introduce several different types of systematic errors. Furthermore, these techniques are best suited to samples containing moderate numbers of high-resolution spectra. As described in the section below, we work with a very large sample of intermediate-resolution spectra and implement an entirely different form of flux normalization.

3.2 The SDSS Data Set

We work with a sample of 5676 QSOs from the Sloan Digital Sky Survey¹ (SDSS) (York et al. 2000) and spanning the redshift range $2.3 < z_{\text{qso}} < 5.4$. We are limited to QSOs with redshift $z_{\text{qso}} > 2.3$ because only at these high redshifts has the Lyman- α forest shifted into the observed wavelength range of the SDSS spectrograph. All spectra are initially processed by the SDSS data reduction pipeline (Abazajian et al. 2004).

3.2.1 Normalizing by the Mean Spectrum

Rather than normalizing each spectrum relative to the QSO continuum, we normalize relative to an estimate of the mean spectrum based on knowledge of the entire sample. The details of this procedure are explained in Appendix B. The end result of this normalization process is that all flux values become flux as measured relative to the mean (rather than, for example, flux as measured relative to the QSO continuum). As a result, it would appear that we lose the ability to then measure the mean flux decrement in the forest. As we will see later in this chapter, however, this is not actually the case.

¹See <http://www.sdss.org/> for details of the Survey.

3.2.2 Correcting the SDSS Noise Estimates

In order to accurately model the underlying flux distribution it is crucial to have a correct characterization of the noise in the data. Though the SDSS data reduction pipeline computes a variance associated with every flux value, there is some evidence (Bolton et al. 2004; McDonald et al. 2004) these error estimates do not perfectly reflect the true errors in the data. We attempt to correct the SDSS noise estimates as follows.

Some of the QSOs in our sample were observed on multiple nights. In these cases we have two measurements of what should be identical spectra; the extent to which they differ reflects the error in the observed flux and provides a cross check on the reported uncertainty.

If all of the error estimates were correct we expect that the difference in measured flux from one observation to the next for a given pixel of a given spectrum would, on average, equal the corresponding error measurement. In other words, the distribution

$$\chi_i^2 = \frac{(f_{i_1} - f_{i_2})^2}{\sigma_{i_1}^2 + \sigma_{i_2}^2} \quad (3.2)$$

should average to unity. The above expression relates two separate observations of a given flux value, f_{i_1} and f_{i_2} , to their variances, $\sigma_{i_1}^2$ and $\sigma_{i_2}^2$. Of course any single value χ_i^2 will differ from unity. But averaged over all pixels in all lines of sight we expect $\langle \chi^2 \rangle = 1$ if the variances σ_i^2 correctly describe the errors. Systematic deviations from $\langle \chi^2 \rangle = 1$ are an indication that the values of σ need to be corrected before they accurately describe the noise.

In fact $\langle \chi^2 \rangle = 1.039$ averaged over 502 pairs and approximately 2000 pixels per line of sight. Thus, the next step is to calculate the mean χ^2 as a function of σ , since there is no reason to believe the distribution is necessarily flat. Then we determine the correction factor which we need to apply to each σ in order to achieve $\langle \chi^2 \rangle = 1$.

In the full data set each spectrum contains a single flux and variance measurement for each pixel (in the case of multiple observations of an object, the data will have been combined). Thus our correction function can only depend on this ‘‘combined variance’’, not on the individual variances σ_1^2 and σ_2^2 . The quantity closest to this combined variance is $\bar{\sigma}$, defined such that

$$\frac{1}{\bar{\sigma}^2} \equiv \frac{1}{\sigma_1^2} + \frac{1}{\sigma_2^2}, \quad \text{or} \quad \bar{\sigma} = \sqrt{\frac{\sigma_1^2 \sigma_2^2}{\sigma_1^2 + \sigma_2^2}}. \quad (3.3)$$

Fig. 3-2 shows χ^2 averaged over each $\bar{\sigma}$ interval, versus $\bar{\sigma}$. The error bars are $1/\sqrt{N}$ of the number of points in the bin. Let $S^2(\bar{\sigma})$ be the function which is the best fit to this distribution of $\chi^2(\bar{\sigma})$. For a piecewise linear fit, we find

$$S^2(\bar{\sigma}) = \begin{cases} 0.932 + 1.17\bar{\sigma} & (\bar{\sigma} < 0.0986) \\ 1.0474 & (\bar{\sigma} > 0.0986) \end{cases} \quad (3.4)$$

The corrected variance is

$$\sigma_{\text{corrected}}^2 = \sigma^2 S^2(\sigma). \quad (3.5)$$

Since in practice we work with inverse variance ($\text{invvar}=1/\sigma^2$), the correction becomes

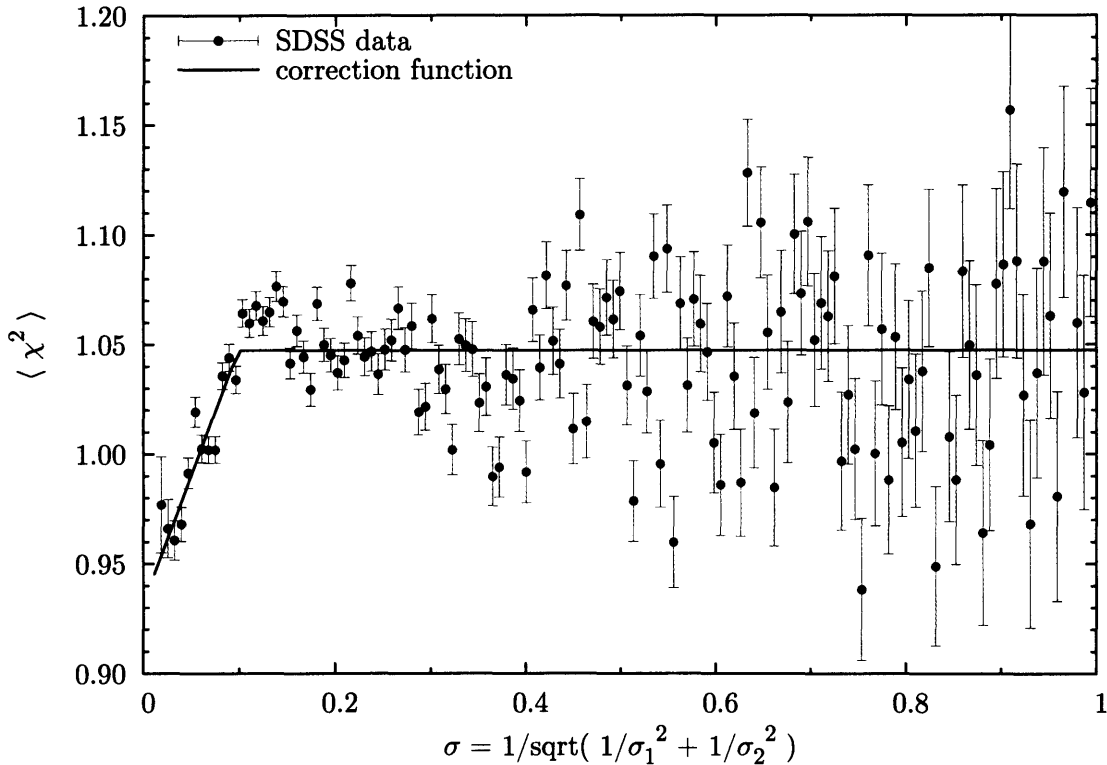


Figure 3-2: Average χ^2 as a function of $\bar{\sigma}$, demonstrating that corrections to the variances are warranted.

(notice the inequality flips):

$$S^2(\text{invvar}) = \begin{cases} 0.932 + 1.17 \text{ invvar}^{-0.5} & (\text{invvar} > 102.86) \\ 1.0474 & (\text{invvar} < 102.86) \end{cases} \quad (3.6)$$

Averaged over all multiple observations, we now find $\langle \chi^2 \rangle = 0.996$. From here on, when we speak of noise values we always mean noise as corrected with the above prescription.

3.2.3 The Flux Probability Distribution Function

The flux probability distribution function (PDF) of the Lyman- α forest is simply the distribution of the number of pixels of a given flux, as a function of flux. We include only data points in the Lyman- α forest region of each spectrum, dropping all pixels redward of Lyman- α (minus 5,000 km/s) = 1195.4Å, ie pixels in the continuum, and also dropping all pixels blueward of Lyman- β (plus 5,000 km/s) = 1042.8Å, ie pixels in the Lyman- β forest² (c.f. Dijkstra et al. (2004)). The 5,000 km/s buffers exclude intrinsic features in the proximity of the QSO.

In order to study the evolution of the PDF we first split the data into 18 separate redshift subsamples and then bin each set of fluxes to form the PDF histogram. We drop the points falling in the top 0.1% and in the bottom 0.1% of the flux distribution to avoid

²In this region of the forest we unfortunately cannot tell the difference between a Lyman- α absorber at redshift $1 + z_\alpha = \lambda_{\text{obs}}/\lambda_{\text{Ly}\alpha}$ and a Lyman- β absorber at redshift $1 + z_\beta = \lambda_{\text{obs}}/\lambda_{\text{Ly}\beta}$.

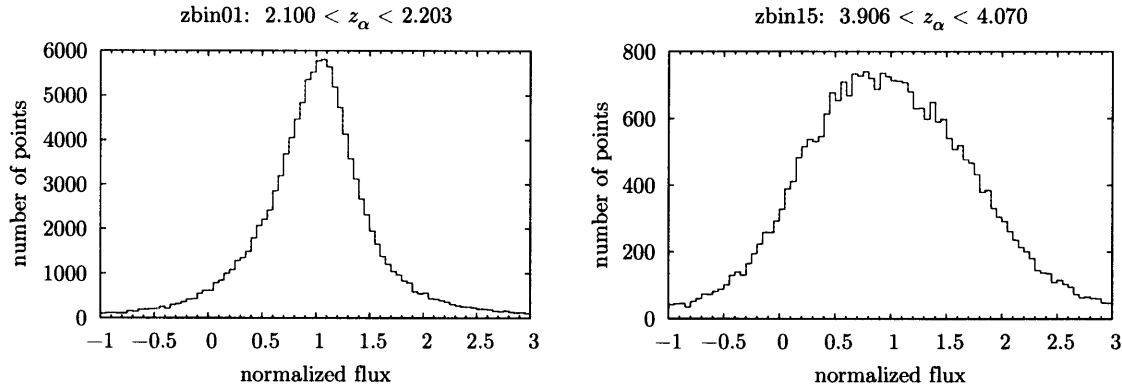


Figure 3-3: Example flux PDFs.

obvious outliers (such as unmasked cosmic rays), but the distributions appear to be very well-behaved in the tails so a more conservative cut is unnecessary. The size of each flux bin is fixed at 0.05 (in units of normalized flux), but the number of bins in each PDF varies with redshift subsample. The first and last flux bins are chosen to coincide with the location of the 0.1% cut, rounded to the next 0.05 bin-width position.

Example PDFs, one for a low redshift bin and one for a high redshift bin, are shown in Fig. 3-3. The data are split into redshift bins based not on the redshifts of the QSOs, z_{qso} , but rather based on the redshifts of the intervening Lyman- α absorbers. For an observed wavelength λ_{obs} , the redshift of the Lyman- α absorber z_{α} is found from

$$\frac{\lambda_{\text{obs}}}{\lambda_{\text{rest}}} = 1 + z_{\alpha} \quad (3.7)$$

where $\lambda_{\text{rest}} = 1215.7\text{\AA}$ for the Lyman- α transition. In this way we separate the pixels of each individual spectrum into redshift bins corresponding to Lyman- α absorption by the intergalactic medium (IGM) in these different redshift shells.

Table 3.1 lists the redshift range of each of the 18 bins and the average redshift, and also gives the number of Lyman- α forest pixels falling in each bin. We estimate the average signal to noise (per pixel) for each line of sight based on the continuum portion of the spectrum (so that a single number describes the signal to noise for the entire line of sight). For each redshift bin, the median value of this signal to noise estimate is also listed. The size of each redshift bin grows as $(1+z)$ so that each bin has a fixed width in velocity space (approximately 10,000 km/s). Fig. 3-4 shows the redshift distribution of the individual Lyman- α forest flux points. Note that the dip at $z \simeq 2.5$ is a result of the SDSS QSO target selection procedure and not indicative of a drop in the actual QSO population.

The goal of the remainder of this chapter is to describe a model for the flux resulting from a distribution of density fluctuations in the IGM that reproduces the flux PDF of the SDSS data.

3.3 The Lognormal Model

Many authors have suggested that that the diffuse intergalactic medium can be modeled by a lognormal distribution of density fluctuations of the dark matter (Bi and Davidsen

zbin	z_{avg}	z_{min}	z_{max}	N_{pts}	median SN
01	2.169	2.100	2.203	194306	8.26
02	2.255	2.203	2.310	293870	7.99
03	2.363	2.310	2.420	238322	7.56
04	2.477	2.420	2.534	220385	6.36
05	2.594	2.534	2.652	236990	5.73
06	2.713	2.652	2.774	266796	5.51
07	2.835	2.774	2.900	260918	5.36
08	2.962	2.900	3.030	226204	5.28
09	3.095	3.030	3.164	190223	5.41
10	3.231	3.164	3.303	158210	5.51
11	3.374	3.303	3.446	141928	5.65
12	3.517	3.446	3.595	120897	5.65
13	3.667	3.595	3.748	97307	5.57
14	3.821	3.748	3.906	63703	5.43
15	3.984	3.906	4.070	47540	4.71
16	4.144	4.070	4.239	30490	4.06
17	4.316	4.239	4.413	20206	3.54
18	4.580	4.413	5.303	20773	3.17

Table 3.1: Redshift bin characteristics: redshift ranges, number of points per bin, and median signal to noise.

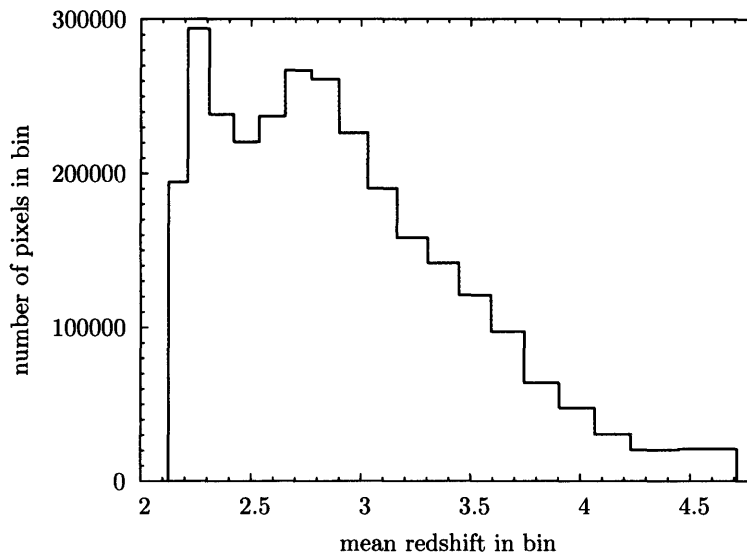


Figure 3-4: Number of pixels in each redshift bin. See Table 3.1 for further details.

1997; Nusser and Haehnelt 1999; Gnedin and Hui 1996). With the further assumption of photoionization equilibrium, the distribution of flux values in the Lyman- α forest is described by three quantities: the optical depth at mean density, the equation of state parameter, and the variance of the density field. This section describes how to model the flux PDF with these three physical parameters.

Following the method of Nusser and Haehnelt (1999), a lognormal distribution of density, ρ/ρ_0 , is found from the Gaussian (zero mean, unit variance) distributed ν by

$$\nu = \frac{\ln[\rho/\rho_0] - \mu}{\sigma}. \quad (3.8)$$

Solving for the density and imposing the condition $\langle \rho \rangle = \rho_0$ gives the constraint $\mu + \sigma^2/2 = 0$. Substituting $\mu = -\sigma^2/2$ into Eq. (3.8) then gives an expression for the lognormal density field in terms of the Gaussian-distributed ν ,

$$\rho/\rho_0 = \exp(\sigma\nu - \sigma^2/2). \quad (3.9)$$

As there are several different quantities in this thesis all referred to as “ σ ”, from here on we attach a subscript as a reminder that this σ is the lognormal model parameter: σ_{\ln} .

Under the assumption of photoionization equilibrium, the optical depth τ and density are related by the equation of state parameter α ,

$$\tau = \tau_0 \left(\frac{\rho}{\rho_0} \right)^\alpha. \quad (3.10)$$

Lastly, we relate the optical depth to resulting transmitted flux:

$$f = \exp(-\tau) \quad (3.11a)$$

$$= \exp(-\tau_0 [\exp(\sigma_{\ln}\nu - \sigma_{\ln}^2/2)]^\alpha) \quad (3.11b)$$

$$= \exp(-\tau_0 \exp[-\alpha\sigma_{\ln}^2/2] \exp[\alpha\sigma_{\ln}\nu]). \quad (3.11c)$$

From the grouping of the three parameters α , σ_{\ln} , and τ_0 in the above expression it is clear that there are not actually three independent degrees of freedom in this model. A natural grouping of terms suggests writing the flux distribution in terms of the two parameters $x \equiv \tau_0 \exp[-\alpha\sigma_{\ln}^2/2]$ and $y \equiv \alpha\sigma_{\ln}$,

$$f = \exp(-xe^{y\nu}), \quad (3.12)$$

but the x and y parameters turn out to be highly correlated and in practice a more orthogonal parameterization is preferable. Unfortunately there is not a single combination which remains orthogonal throughout the relevant range of parameter values, but a good compromise are the particular combinations

$$A \equiv \frac{\alpha\sigma_{\ln}^2}{2} - \ln[\tau_0] - \ln[\alpha\sigma_{\ln}] \quad (3.13a)$$

$$B \equiv \frac{\alpha\sigma_{\ln}^2}{2} - \ln[\tau_0] + \ln[\alpha\sigma_{\ln}]. \quad (3.13b)$$

The underlying physical model constrains the value of the equation of state parameter to fall in the range

$$2 \geq \alpha \geq 1.53. \quad (3.14)$$

At early times the gas obeys an isothermal equation of state ($\alpha = 2$), while at late times the behavior is that of an ideal gas ($\alpha = 1.53$). The redshift over which this transition occurs

is not precisely known but it is safe to assume that α is bounded by Eq. (3.14). This extra constraint will allow us to derive ranges for τ_0 and σ_{\ln} given the two constraints obtained from fitting the model.

For a value of α we invert Eq. (3.13) to obtain τ_0 and σ_{\ln} in terms of the fit parameters A and B ,

$$\sigma_{\ln} = \exp\left(-\frac{1}{2}[A - B]\right) \frac{1}{\alpha} \quad (3.15a)$$

$$\tau_0 = \exp\left(-\frac{1}{2}[A + B]\right) \exp(\alpha\sigma_{\ln}^2/2). \quad (3.15b)$$

To propagate errors on the fitted values of A and B to errors on τ_0 and σ_{\ln} , use the standard error propagation formula

$$\sigma_x^2 = \sigma_u^2 \left(\frac{\partial x}{\partial u}\right)^2 + \sigma_v^2 \left(\frac{\partial x}{\partial v}\right)^2 + 2\sigma_{uv}^2 \left(\frac{\partial x}{\partial u}\right) \left(\frac{\partial x}{\partial v}\right). \quad (3.16)$$

Given errors on A and B and their correlation, we compute the error in the two physical parameters by

$$\sigma_{\sigma_{\ln}}^2 = \frac{1}{4}\sigma_{\ln}^2(\sigma_A^2 + \sigma_B^2 - 2\sigma_{AB}^2) \quad (3.17)$$

and

$$\sigma_{\tau_0}^2 = \frac{1}{4}\tau_0^2 \left(\sigma_A^2 \left[1 + \frac{2e^\Delta}{\alpha} + \frac{e^{2\Delta}}{\alpha^2}\right] + \sigma_B^2 \left[1 - \frac{2e^\Delta}{\alpha} + \frac{e^{2\Delta}}{\alpha^2}\right] + \sigma_{AB}^2 \left[1 - \frac{e^{2\Delta}}{\alpha^2}\right] \right). \quad (3.18)$$

For clarity we have substituted $\Delta \equiv (B - A)$ in the above expression.

3.3.1 The Shape of the PDF

The previous section describes how to generate a distribution of flux points specified by the parameters A and B starting from a distribution of Gaussian random number (ν). It is illustrative to solve for the equation describing the resulting flux probability distribution, though in practice not the approach we will be able to use. As will be described in section 3.4.2 we will need to add noise to the individual flux points in the model distribution and this complicated transformation ruins any hope for an analytic distribution function.

However, it is still useful to see the shape of the underlying flux distribution before this noise is added. Using the probability transformation $P(f) = P(\nu) |d\nu/df|$ and the form of the Gaussian probability distribution function for zero mean and unit variance,

$$P(\nu) = \frac{1}{\sqrt{2\pi}} \exp(-\nu^2/2), \quad (3.19)$$

we find

$$P(f) = \left| \frac{1}{f \ln[f] \alpha \sigma_{\ln} \sqrt{2\pi}} \right| \exp \left\{ \frac{-(\ln[-\ln[f]] - \ln[\tau_0 \exp[-\alpha\sigma_{\ln}^2/2]])^2}{2\alpha^2 \sigma_{\ln}^2} \right\}. \quad (3.20)$$

Fig. 3-5 shows how varying the parameters of the fit effects the shape of the PDF.

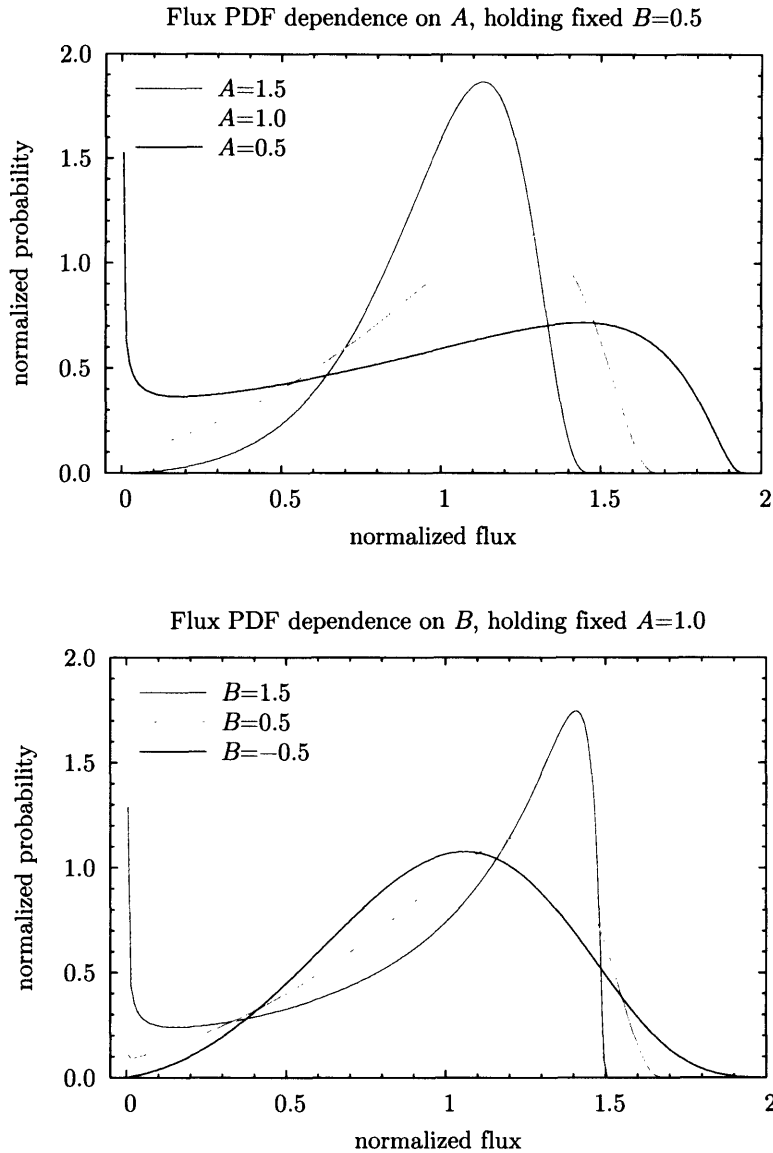


Figure 3-5: The shape of the flux PDF as the two parameters in the model are varied. The green curves are identical in both plots and show the PDF for $A = 1.0$, $B = 0.5$. The red curves show the distribution for values of A or B near the maximum value attained in this model, and the blue curves the minimum.

3.4 Fitting the Model

For each redshift bin described in Table 3.1 we find the best fit values of the fit parameters A and B by finding the values that minimize χ^2 between the PDF of the data and a model PDF. The fit is performed using a Levenberg-Marquardt minimization routine from Numerical Recipes (Press et al. 1992). There are several steps to generating this model PDF, each described below.

3.4.1 Generating Model Flux Points

We begin by drawing flux points from the distribution described by Eq. (3.11) for a given A and B . Remember that this equation is written in terms of the Gaussian random variable ν so this can be achieved by generating a random ν and then finding the corresponding flux by evaluating Eq. (3.11). To facilitate including noise, as will be described below, we generate the same number of model flux points as there are data points in a given redshift bin.

In practice, rather than repeatedly drawing random values for ν we evaluate the inverse error function at equally spaced intervals. This produces a set of ν 's which map out a Gaussian probability distribution but are smooth rather than statistically noisy from the finite sample size.

The last step is to normalize each flux value by the mean of the distribution. This is analogous to the procedure of normalizing the SDSS spectra by the mean spectrum as described in section 3.2.1, in the sense that now both the data and the model PDFs describe flux values measured relative to the mean. Throughout this chapter “normalized flux” refers to exactly this,

$$f_{\text{normalized}} \equiv \frac{f}{\langle f \rangle} = f \left(\frac{1}{N} \sum_{i=1}^N f_i \right)^{-1}, \quad (3.21)$$

where the average is taken over all (N) Lyman- α flux points in a redshift bin.

3.4.2 Modeling the Noise

In order to meaningfully compare the model flux distribution to the SDSS data, we need to correctly include in the model a representation of the noise present in the observations. Since changing the magnitude of the noise on each data point in the flux distribution results in the PDF changing in nearly the same way it would from changing parameters of the underlying lognormal model (primarily, the variance of the density field itself), a correct representation of the noise in the data is crucial. This is the motivation for the variance corrections described in section 3.2.2. We will revisit the issue of testing the success of the noise characterization in the next section.

The noise in the SDSS observations is complicated enough that a noise model would have to include, at minimum, shot noise, a component dependent on which line of sight a given pixel came from, and a (probably flux-dependent) component describing errors in the data reduction and spectral extraction. Though it is more cumbersome, a much more accurate approach is to use the set of (corrected) variances from the data points in the PDF and map each individual variance onto one of the points in the model distribution. To allow for flux dependence in the errors, we first sort the flux values in each distribution. Thus, the largest flux point in the model distribution is assigned the error from the largest flux point in the data set, and so on. When we assign an error to a point in the model distribution this amounts to replacing what would have been a delta-function in the PDF histogram with a Gaussian contributing fractional counts to each flux bin in the histogram – the flux is smeared out in the PDF according to its assigned error. The standard deviation of this Gaussian is just the uncertainty of the corresponding flux value. While this approach does require supplying large data files containing each individual flux variance (nearly 3 million values in total) it incorporates all of the information available to describe the noise. We

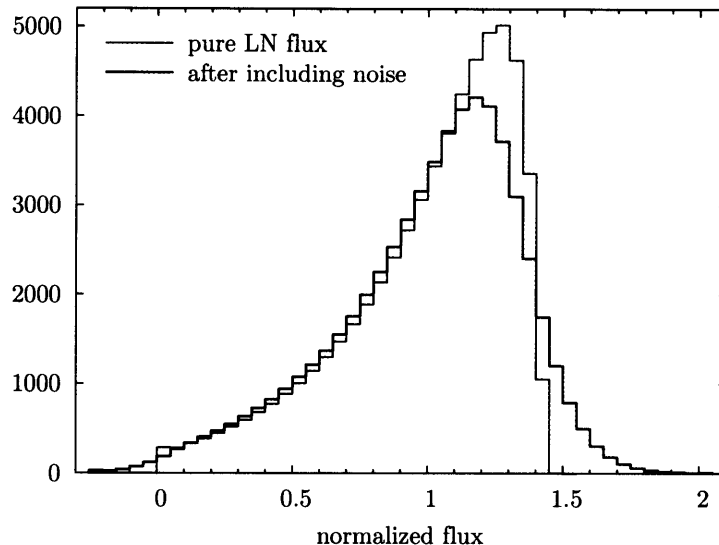


Figure 3-6: Flux PDF resulting from best fit lognormal model to redshift bin 05, before (red curve) and after (blue curve) adding noise.

assume individual uncertainties are Gaussian and that noise correlates with flux but nothing further about the underlying noise distribution.

Fig. 3-6 shows an example of how adding noise changes the underlying lognormal PDF (red curve) to the full PDF (blue curve) appropriate for comparing to the SDSS data.

3.4.3 Applying a Signal to Noise Cut

In order to quantify the degree to which the results of the fit are affected by the noise in the data, we split the points in each redshift bin into quartiles based on the estimated signal to noise of each line of sight. Flux points from spectra in the bottom 25th percentile of signal to noise for that redshift bin were put into the first quartile, flux points from spectra with signal to noise between the 25th percentile and the median were put into the second quartile, points between the median and 75th percentile into the third quartile, and the highest signal to noise spectra into the fourth quartile. Pixels from a given line of sight were kept together, so the quartiles each have approximately $N/4$ points but not exactly. The signal to noise for a line of sight is calculated from the continuum portion of the spectrum not from the Lyman- α forest points directly, but is very representative of the relative quality of the forest data from one line of sight to the next.

We performed the fit on each quartile independently, the results are shown in Fig. 3-7. For clarity the error bars are omitted from the plot, but see Fig. 3-9 for an indication of their size. It is clear that the low-quality half of the data set produces a biased fit, but the agreement is reasonable between the third and fourth quartile (with signal to noise above the median) indicating that the fit has stabilized. We chose to work with only the fourth (highest signal to noise) quartile from here on, but we will use the difference between the fit to the third and fourth quartile as an estimate of the systematic error in the fit.

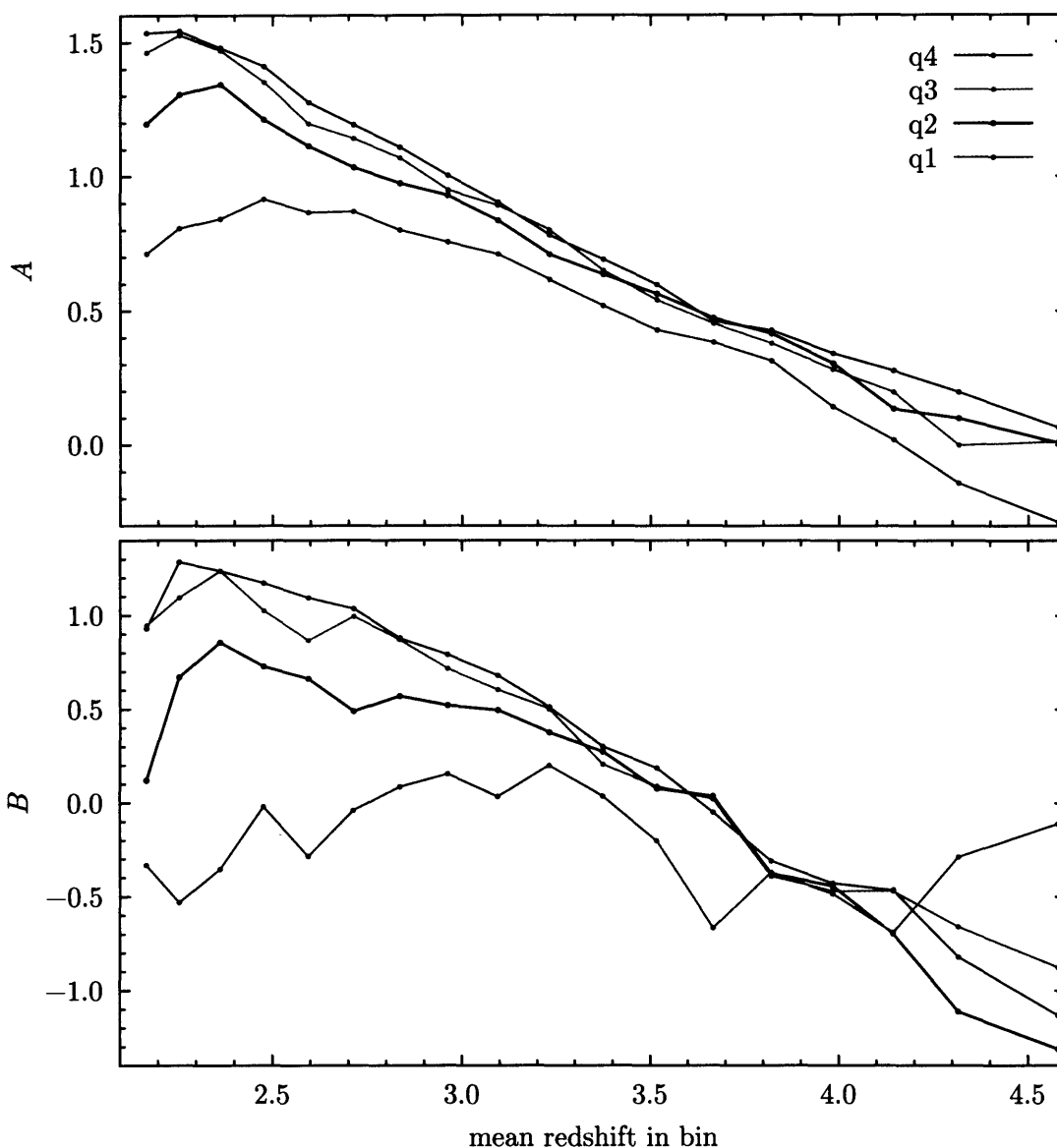


Figure 3-7: Best fit values of A and B obtained by dividing each redshift bin into four signal to noise quartiles and performing the fit separately on each.

3.5 Results of the Fit

The results of the fit on the highest signal to noise quartile of the data are presented in Table 3.2 and the goodness of fit is plotted in Fig. 3-8. Fig. 3-9 shows the best fit values of A and B as well as their errors. The double error bars denote the formal errors and then our estimate of how to increase them to account for the systematic uncertainty due to signal to noise effects and poor fitting. The short error bars show the statistical uncertainty in the fit and correspond to the errors labeled $\sigma^{(1)}$ in Table 3.2. The longer thin error bars show what we estimate the actual uncertainty in the measurement to be and correspond to the errors labeled $\sigma^{(2)}$ in Table 3.2. These corrected errors are based on comparing the fits

zbin	χ^2/dof	A	$\sigma_A^{(1)}$	$\sigma_A^{(2)}$	B	$\sigma_B^{(1)}$	$\sigma_B^{(2)}$	$\text{corr}(AB)$
01	7.070	1.521	0.008	0.043	1.001	0.037	0.111	0.651
02	10.193	1.543	0.006	0.031	1.329	0.025	0.074	0.687
03	9.255	1.460	0.005	0.027	1.280	0.022	0.066	0.653
04	8.857	1.392	0.005	0.028	1.210	0.022	0.067	0.634
05	8.498	1.257	0.005	0.027	1.116	0.022	0.065	0.613
06	8.127	1.172	0.004	0.024	1.038	0.019	0.058	0.562
07	4.118	1.094	0.004	0.022	0.895	0.019	0.057	0.477
08	2.806	0.989	0.004	0.023	0.776	0.020	0.059	0.414
09	1.567	0.893	0.004	0.017	0.671	0.021	0.040	0.345
10	1.608	0.772	0.005	0.019	0.500	0.024	0.044	0.253
11	1.289	0.687	0.005	0.020	0.303	0.025	0.048	0.143
12	0.869	0.599	0.006	0.023	0.181	0.028	0.053	0.085
13	1.230	0.468	0.007	0.027	-0.072	0.033	0.062	-0.053
14	0.827	0.435	0.009	0.036	-0.375	0.048	0.091	-0.150
15	0.804	0.346	0.010	0.040	-0.428	0.048	0.090	-0.249
16	1.209	0.275	0.013	0.050	-0.508	0.057	0.107	-0.213
17	0.845	0.210	0.016	0.062	-0.752	0.064	0.120	-0.286
18	1.148	0.090	0.019	0.072	-1.160	0.075	0.142	-0.346

Table 3.2: Best fit parameters and their errors. The two errors quoted for each parameter are (1) purely the statistical uncertainty of the fit and (2) also including an estimate of the systematic uncertainty due to signal to noise effects. Note that $\text{corr}(AB) \equiv \sigma_{AB}/(\sigma_A\sigma_B)$ and so the correction factors will cancel in the ratio.

from the third and fourth signal to noise quartiles and scaling the reported errors up until they equal the mean square deviation between the fits.

Figures 3-10 to 3-27 show the PDFs for all eighteen redshift bins (red data points) and their best fit lognormal models (black histograms). For comparison the underlying lognormal PDF without any noise added is also shown (blue curves). The residual plotted in the bottom panel of each figure is the difference between the data and the model in units of σ_{flux} , the estimated counting error in each flux bin. For a good fit one would expect roughly 67% of the points in this panel to fall within the dotted lines at 1σ — clearly not the case at low redshift, but generally true at high redshift. The total number of points in each redshift bin is approximately one quarter the number listed in Table 3.1 since these fits are only based on the fourth signal to noise quartile.

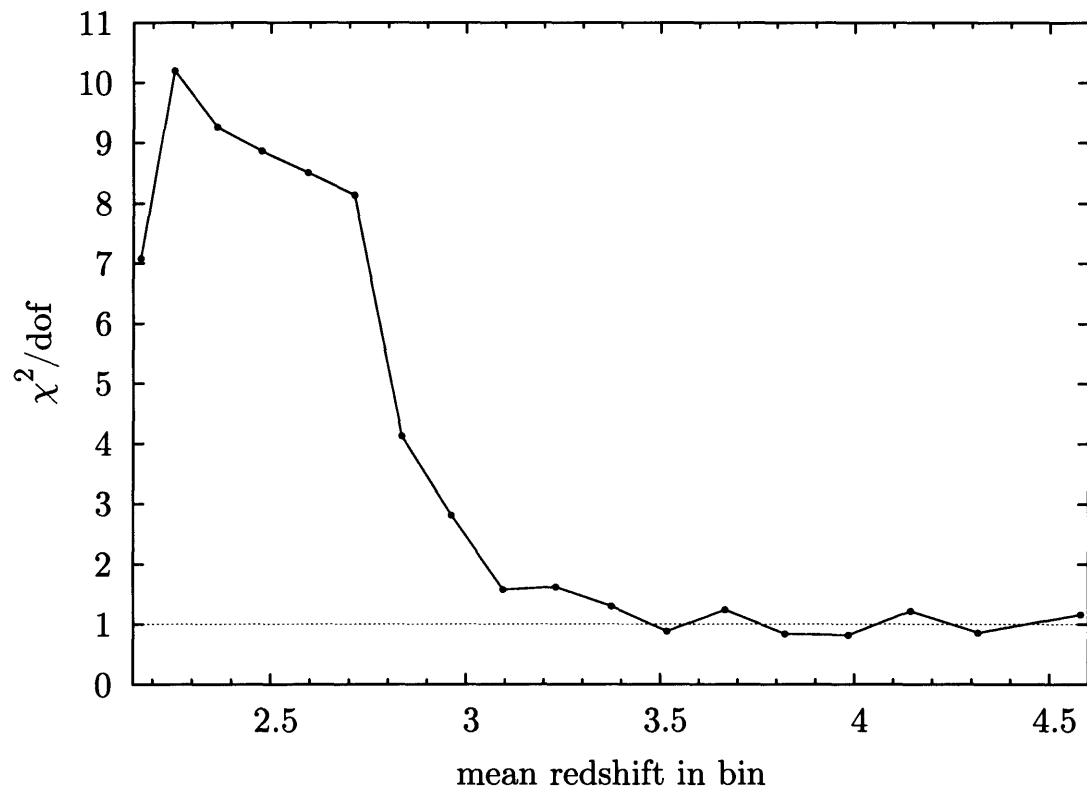


Figure 3-8: χ^2 per degree of freedom for the best fit lognormal model at each redshift bin. Clearly the model is not a good fit for redshifts $z < 3$.

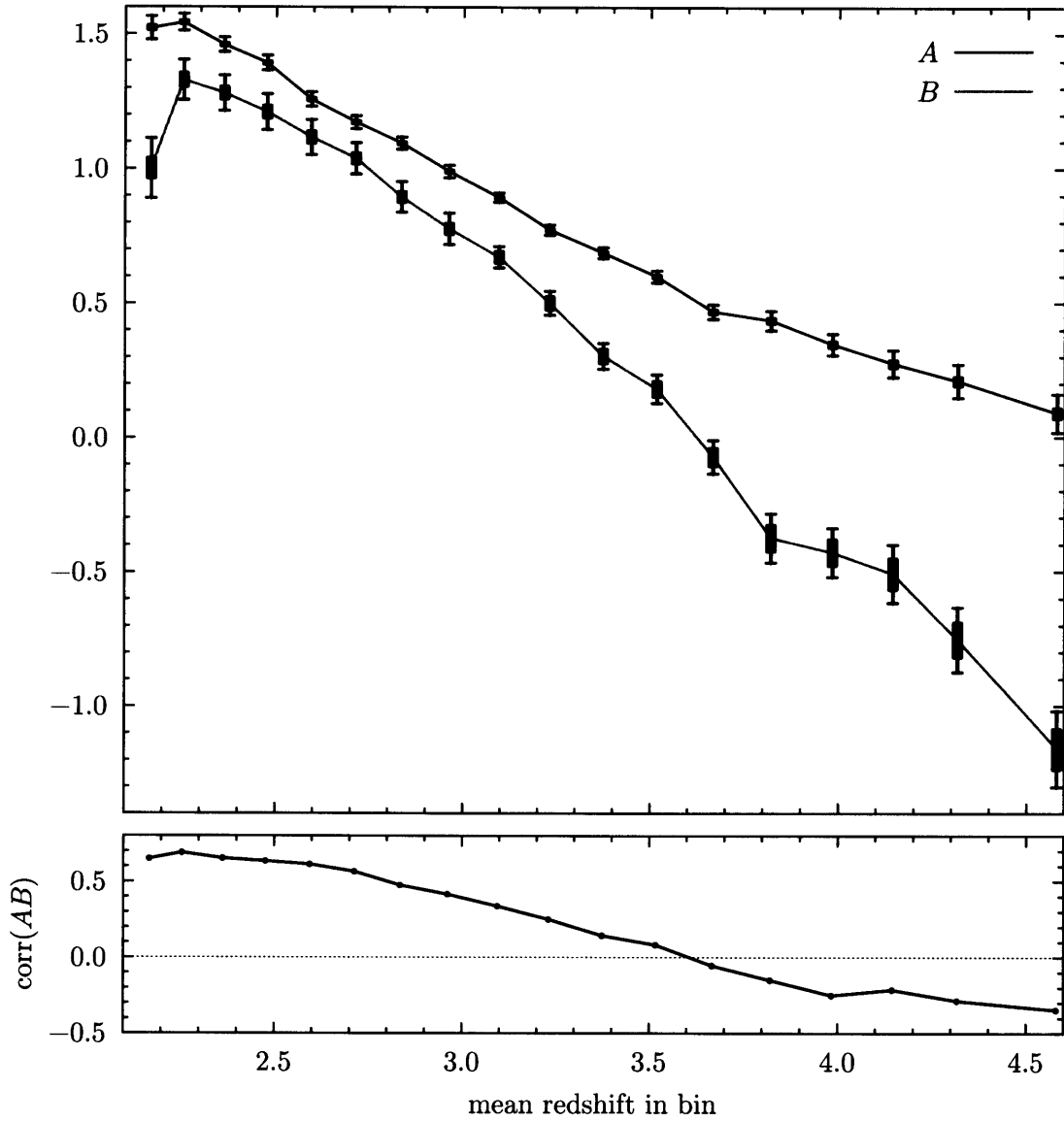


Figure 3-9: Best fit A and B for the fourth signal to noise quartile. The double error bars show the errors $\sigma^{(1)}$ and $\sigma^{(2)}$ from Table 3.2. The correlation between the parameters is $\text{corr}(AB) \equiv \sigma_{AB}/(\sigma_A \sigma_B)$.

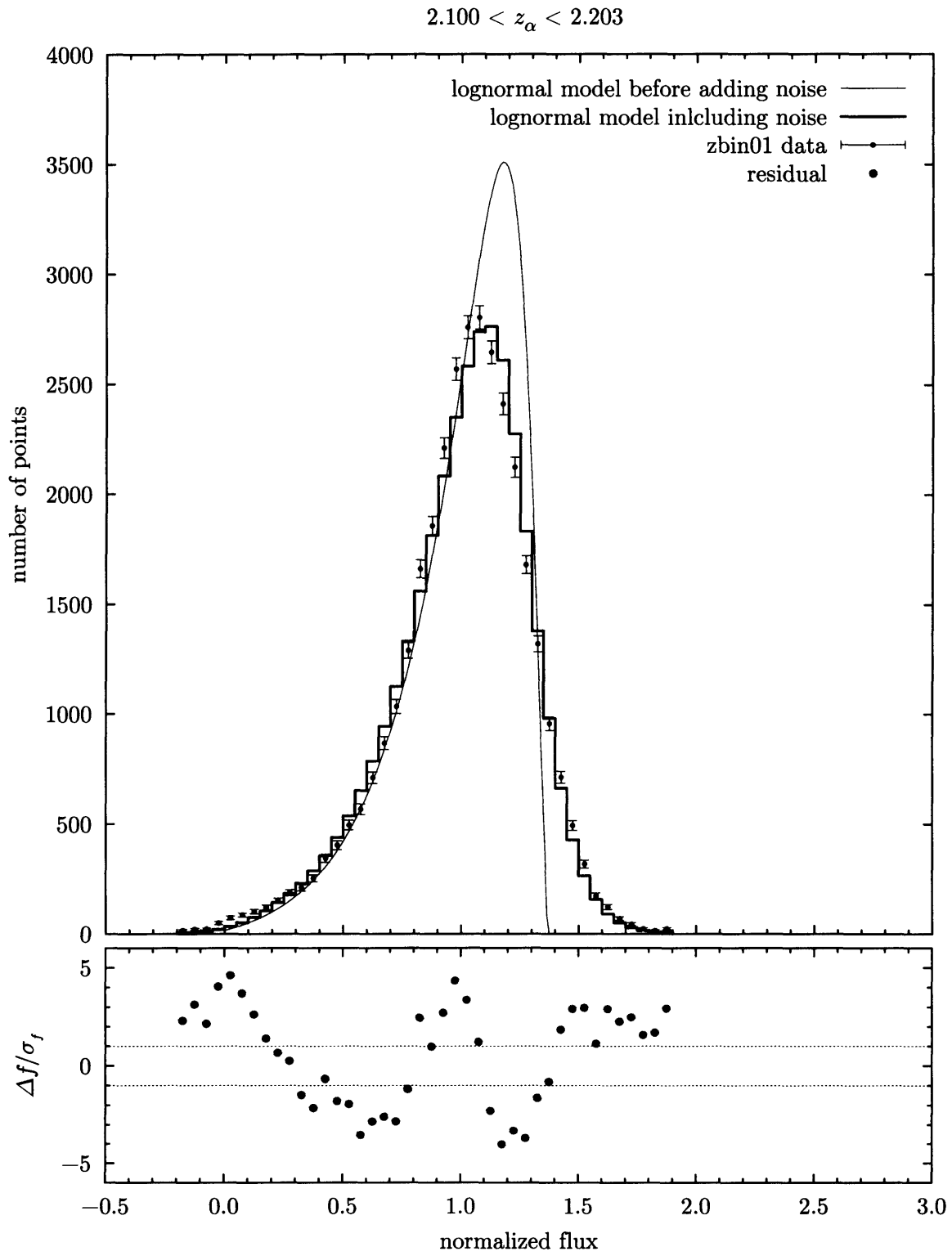


Figure 3-10: The lognormal fit for $z \sim 2.2$.

$2.203 < z_\alpha < 2.310$

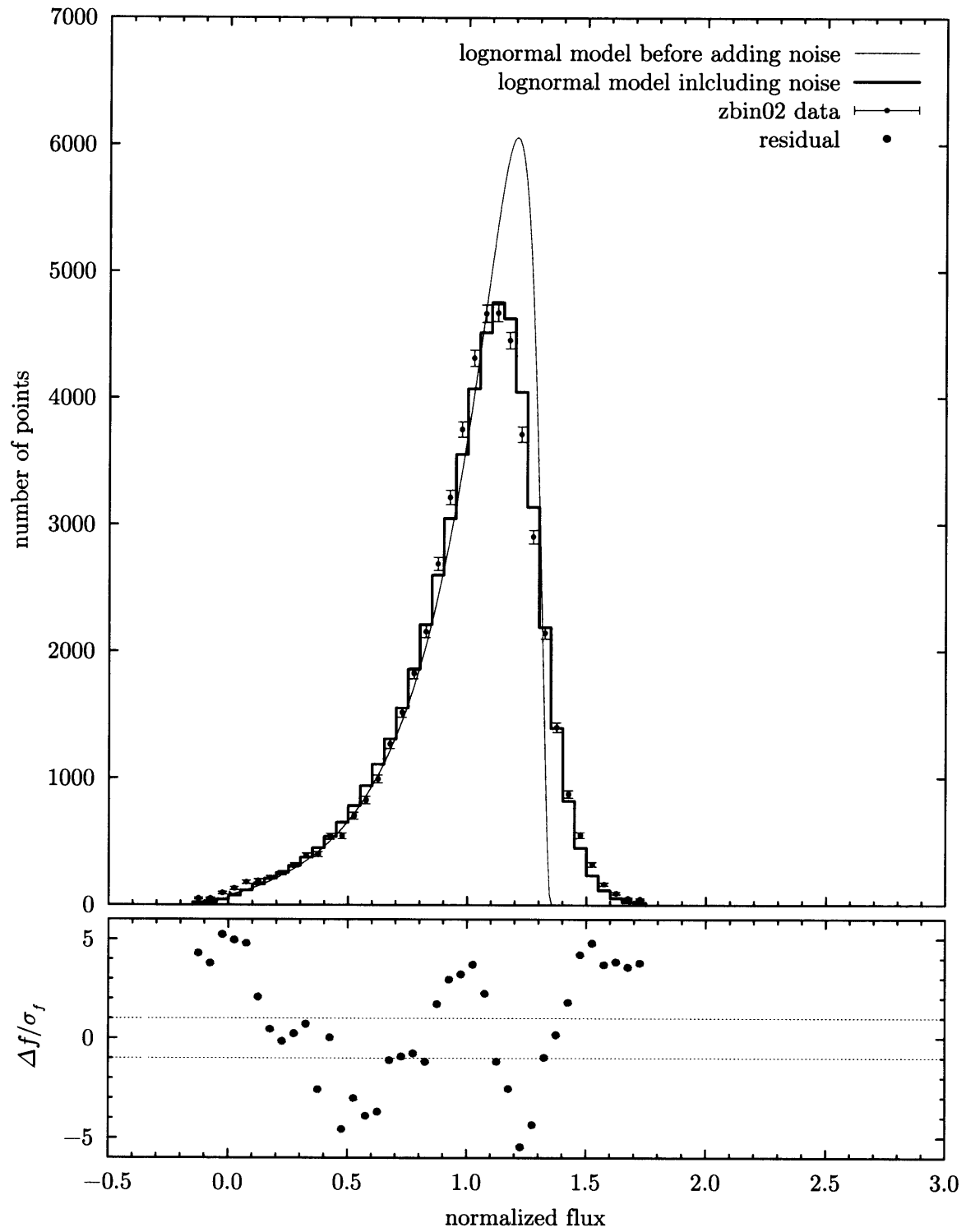


Figure 3-11: The lognormal fit for $z \sim 2.3$.

$2.310 < z_{\alpha} < 2.420$

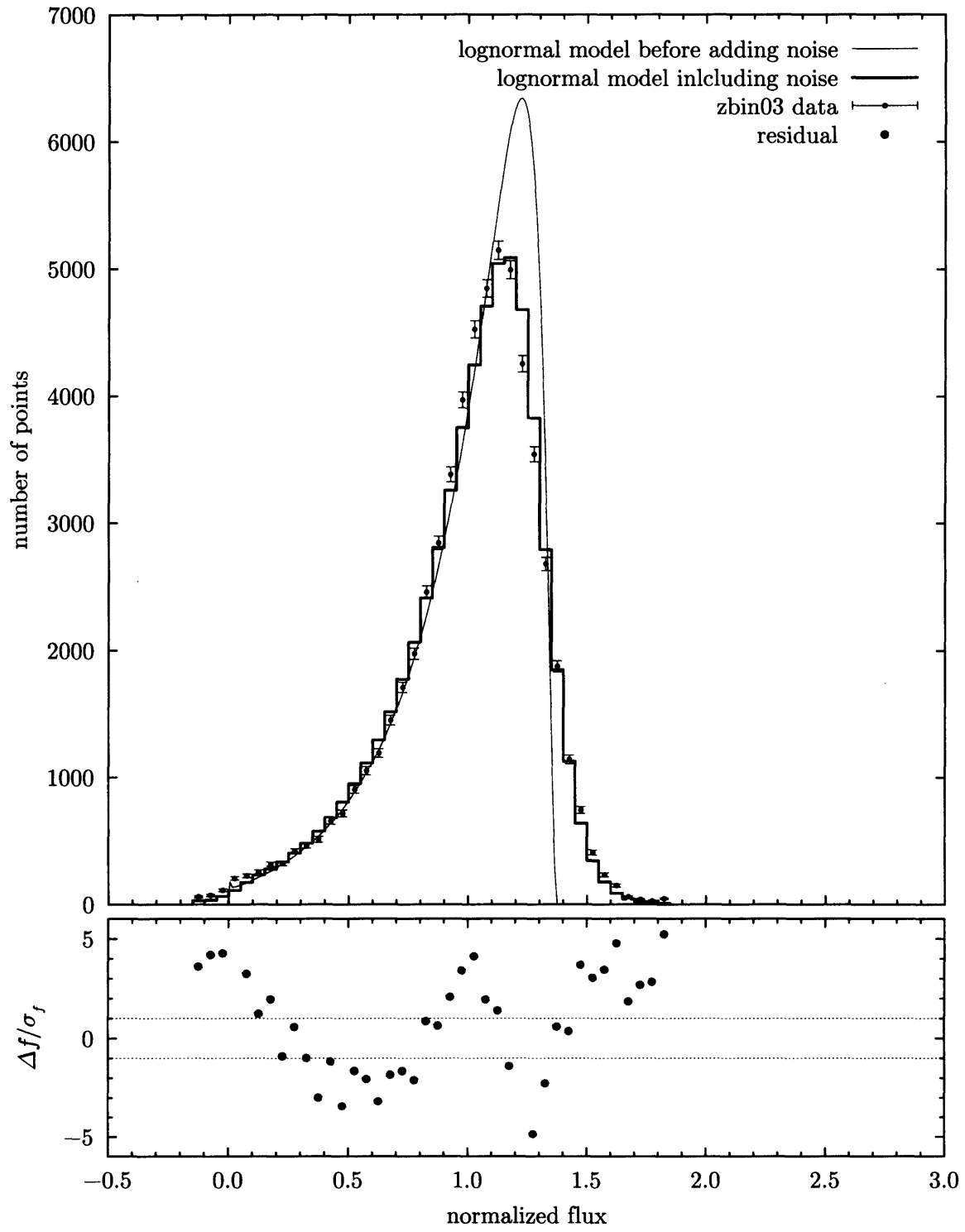


Figure 3-12: The lognormal fit for $z \sim 2.4$.

$2.420 < z_{\alpha} < 2.534$

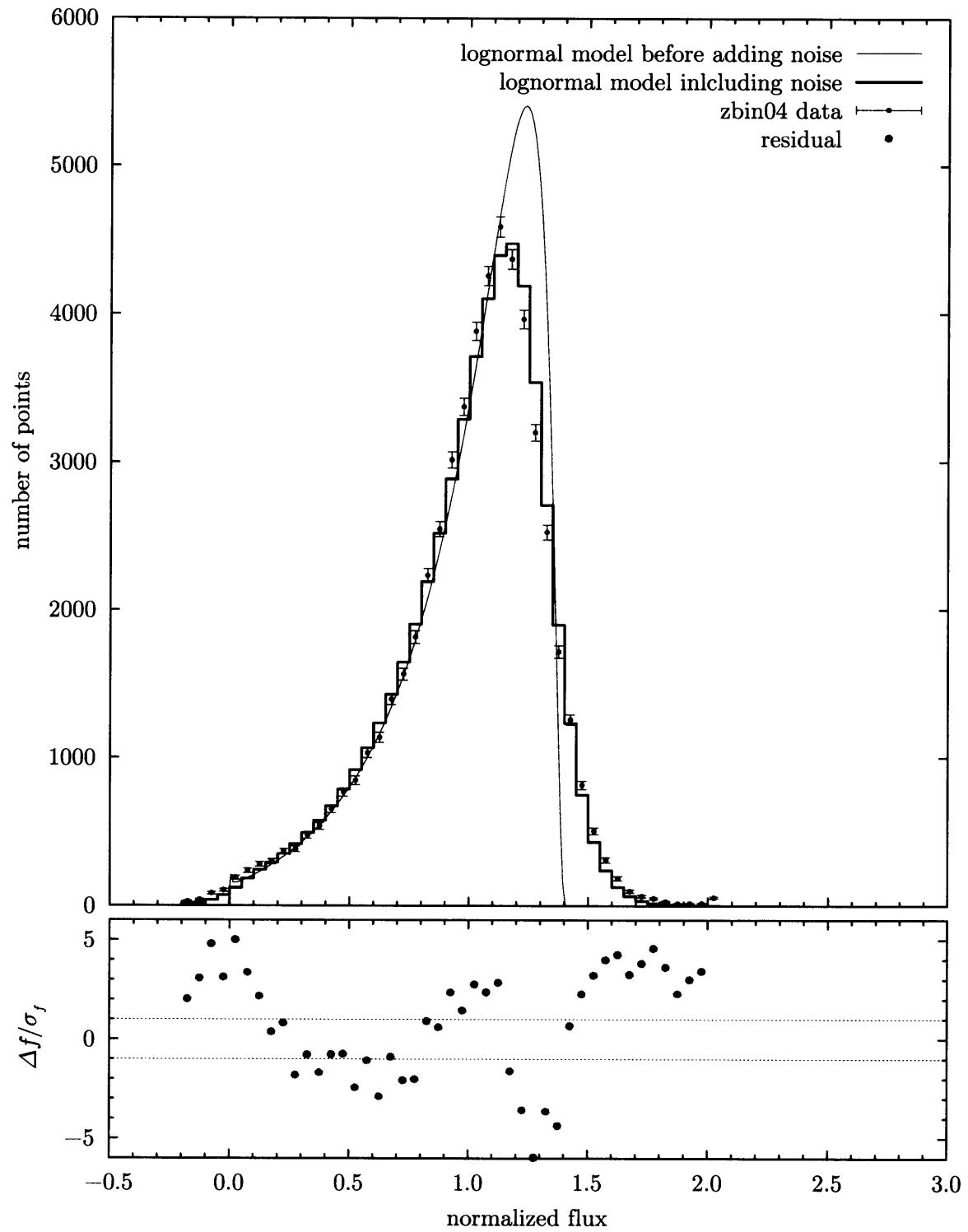


Figure 3-13: The lognormal fit for $z \sim 2.5$.

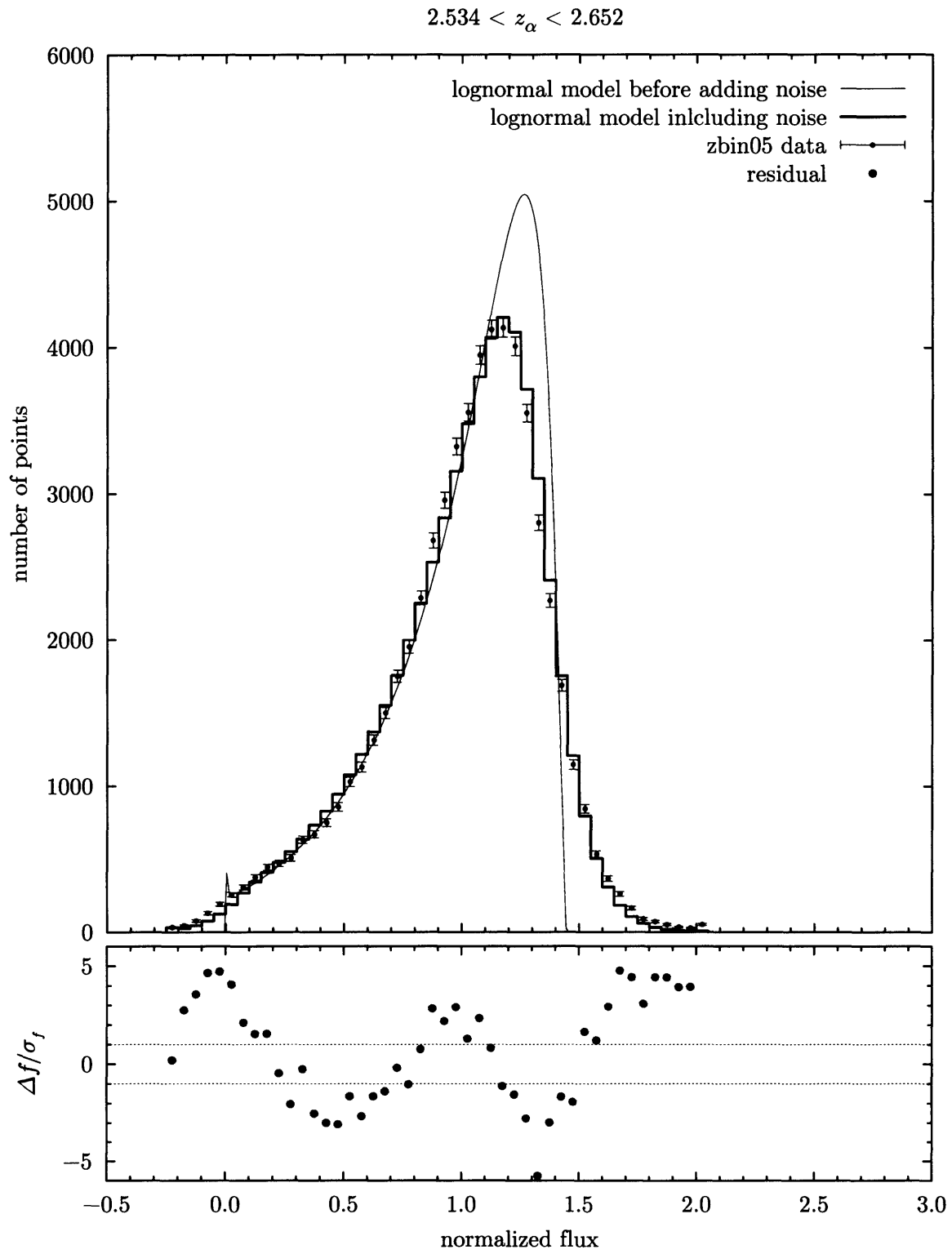


Figure 3-14: The lognormal fit for $z \sim 2.6$.

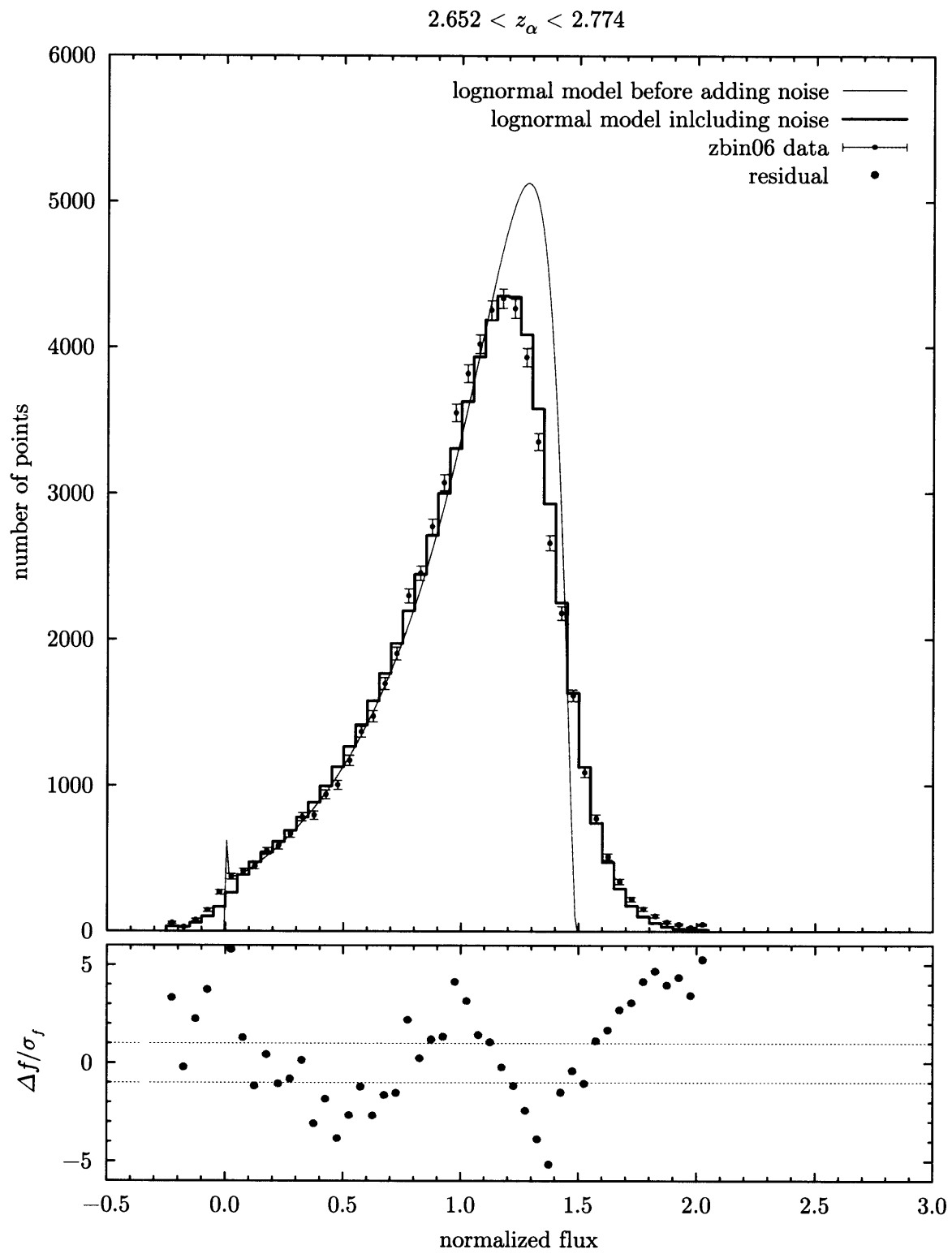


Figure 3-15: The lognormal fit for $z \sim 2.7$.

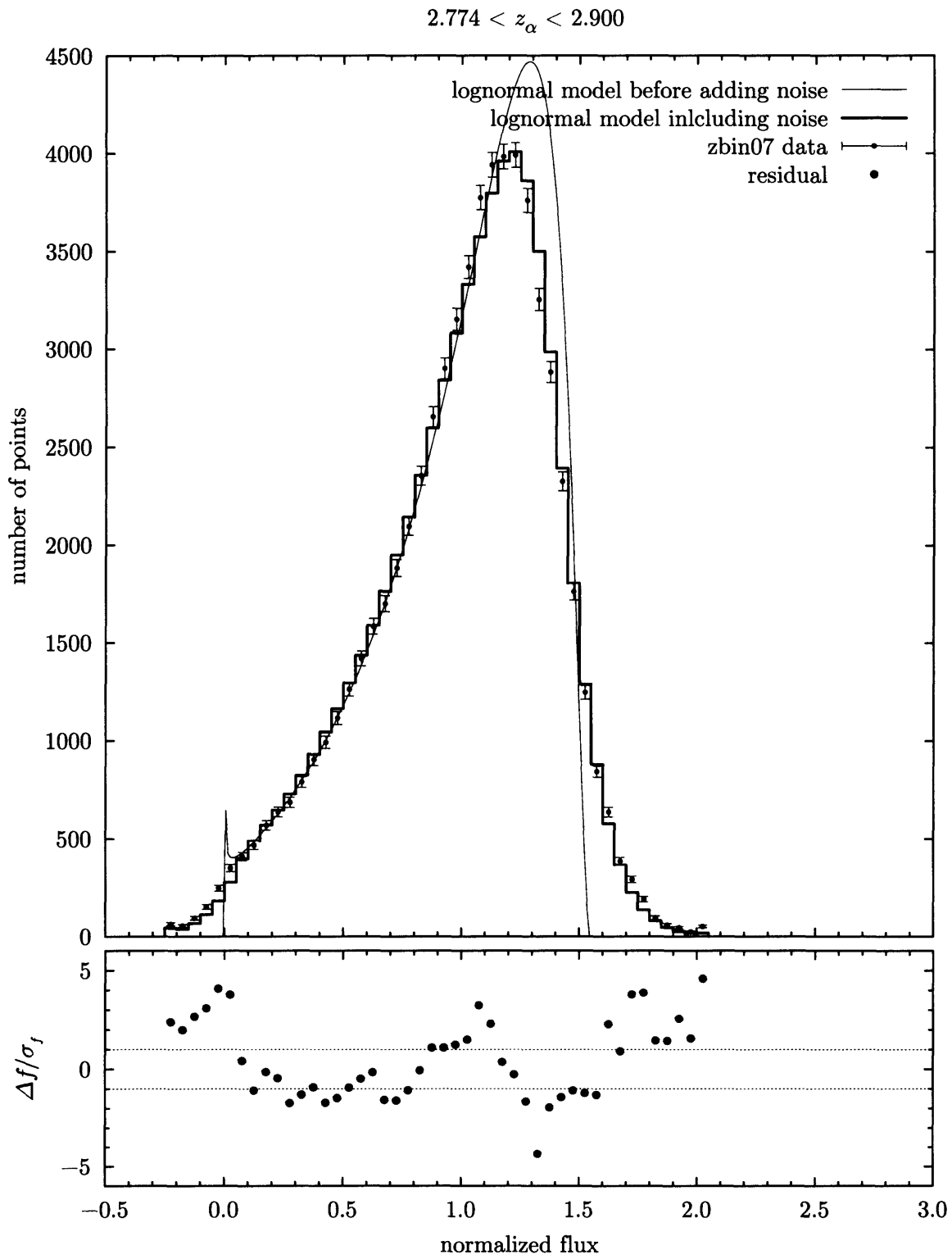


Figure 3-16: The lognormal fit for $z \sim 2.8$.

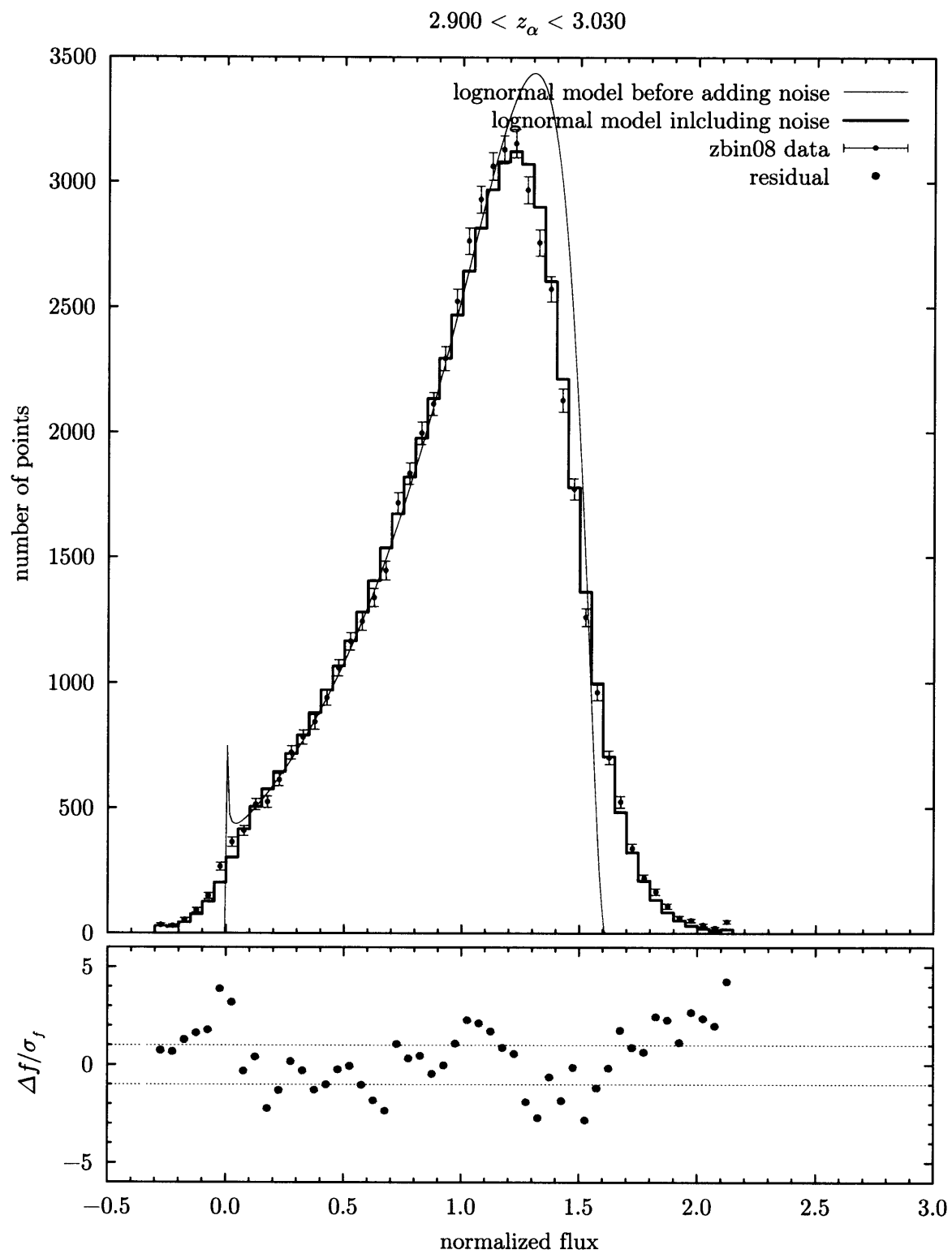


Figure 3-17: The lognormal fit for $z \sim 3.0$.

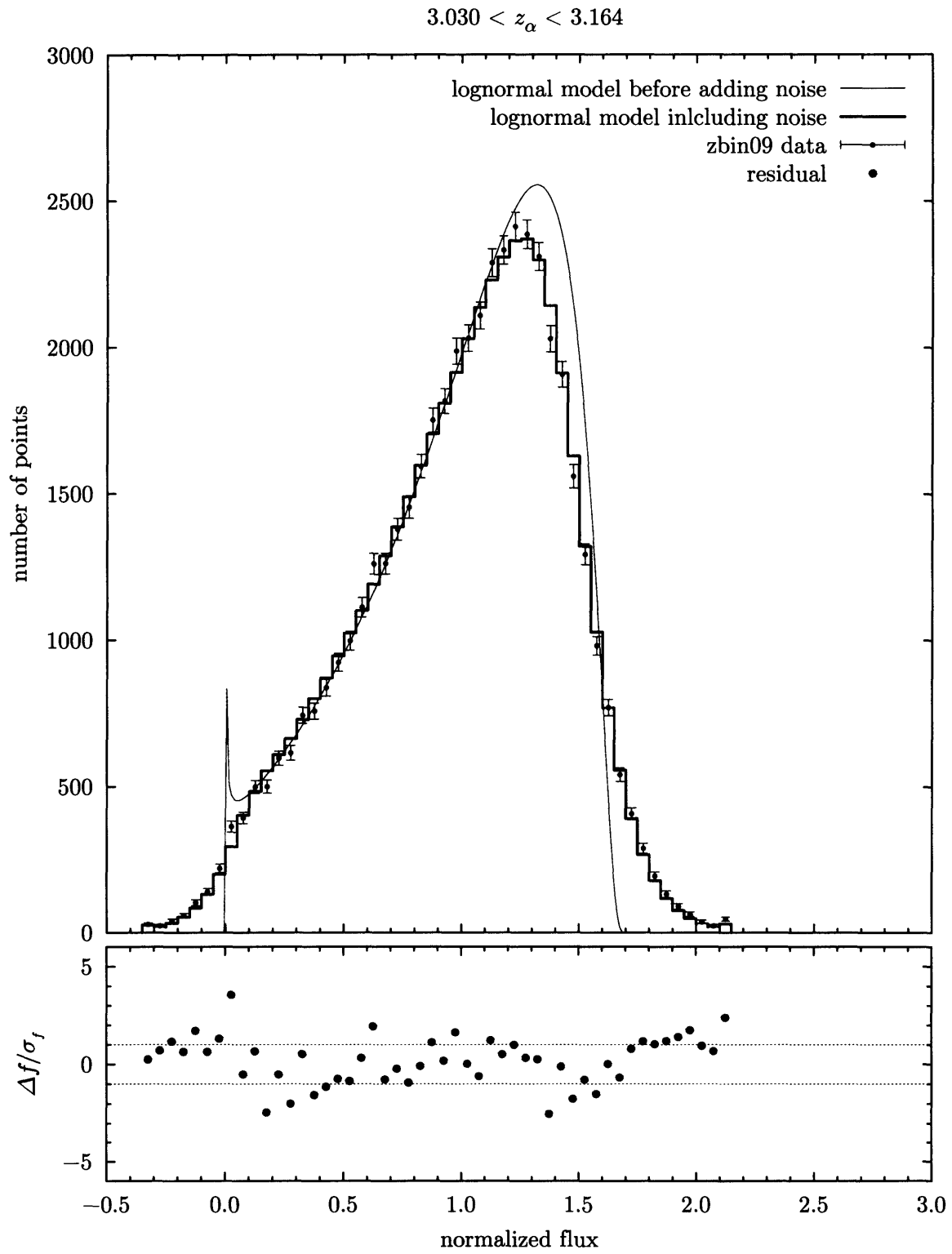


Figure 3-18: The lognormal fit for $z \sim 3.1$.

$3.164 < z_\alpha < 3.303$

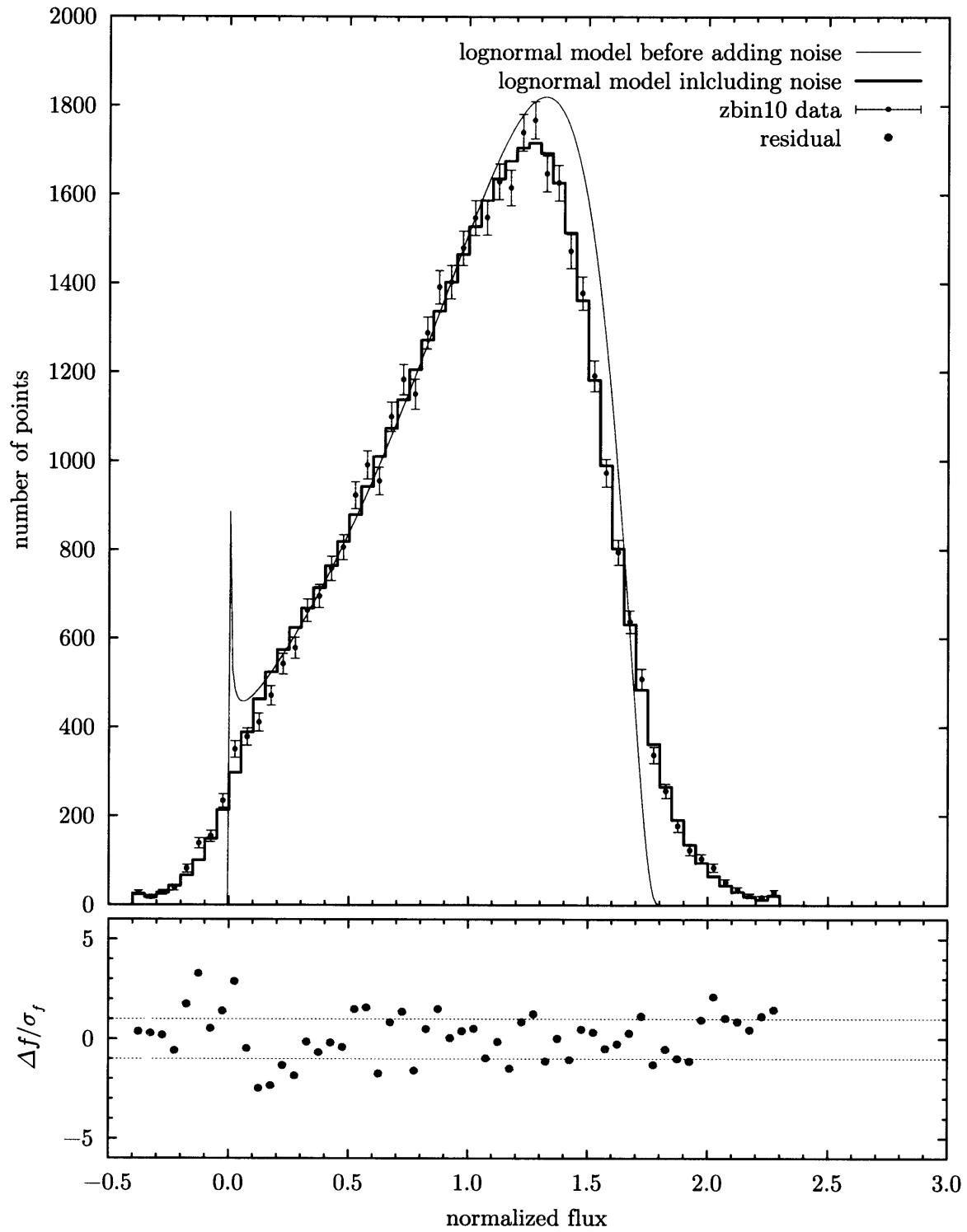


Figure 3-19: The lognormal fit for $z \sim 3.2$.

$3.303 < z_\alpha < 3.446$

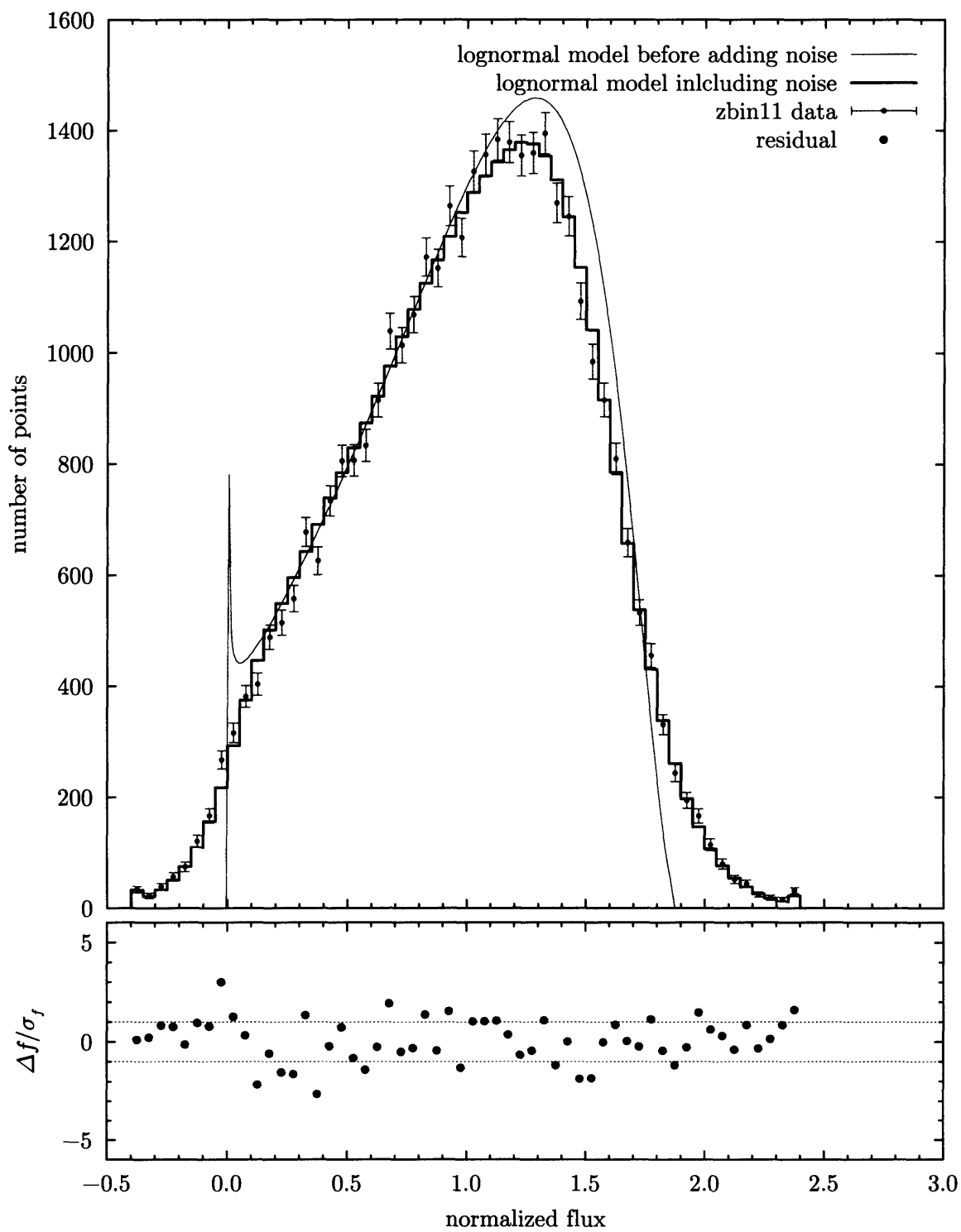


Figure 3-20: The lognormal fit for $z \sim 3.4$.

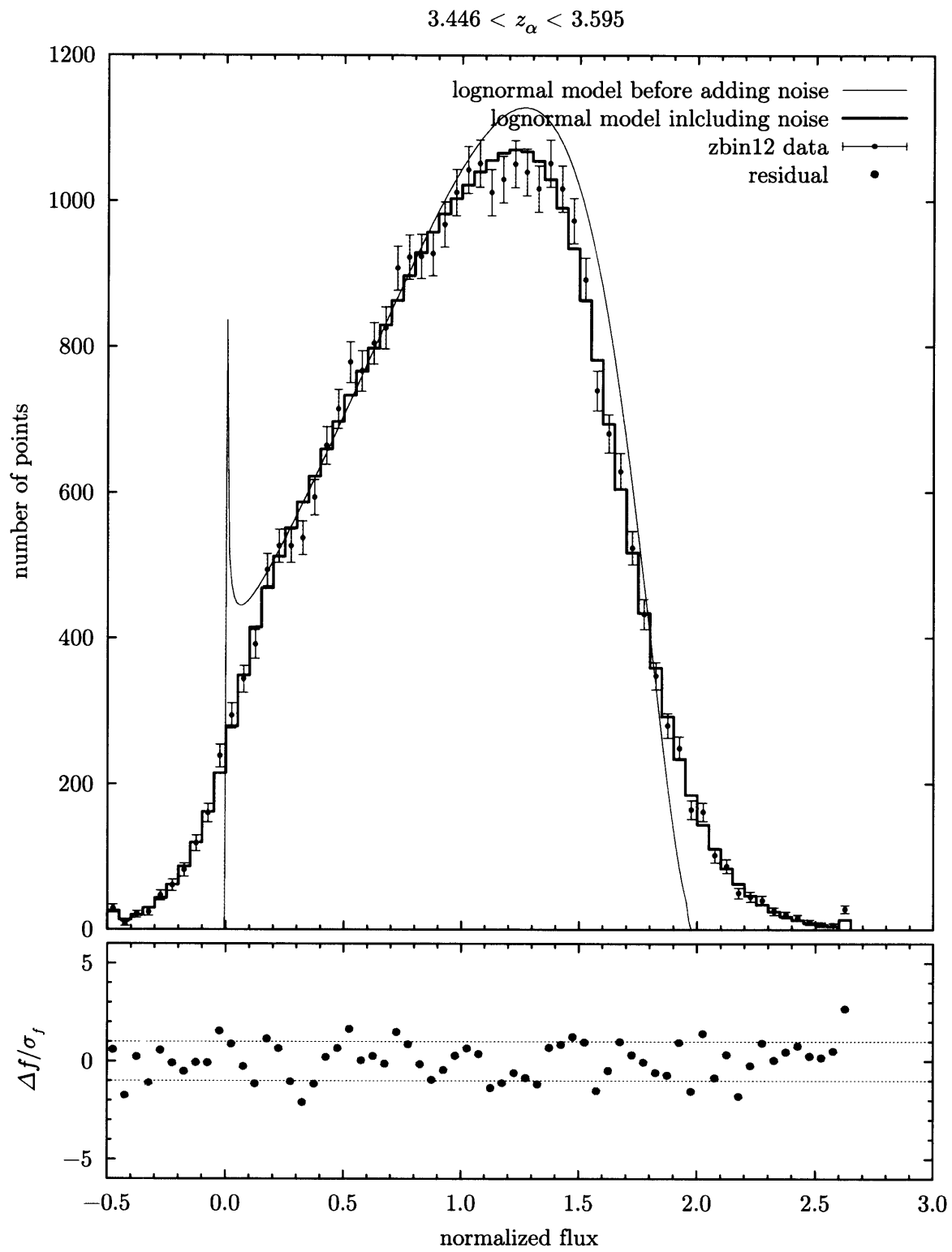


Figure 3-21: The lognormal fit for $z \sim 3.5$.

$3.595 < z_{\alpha} < 3.748$

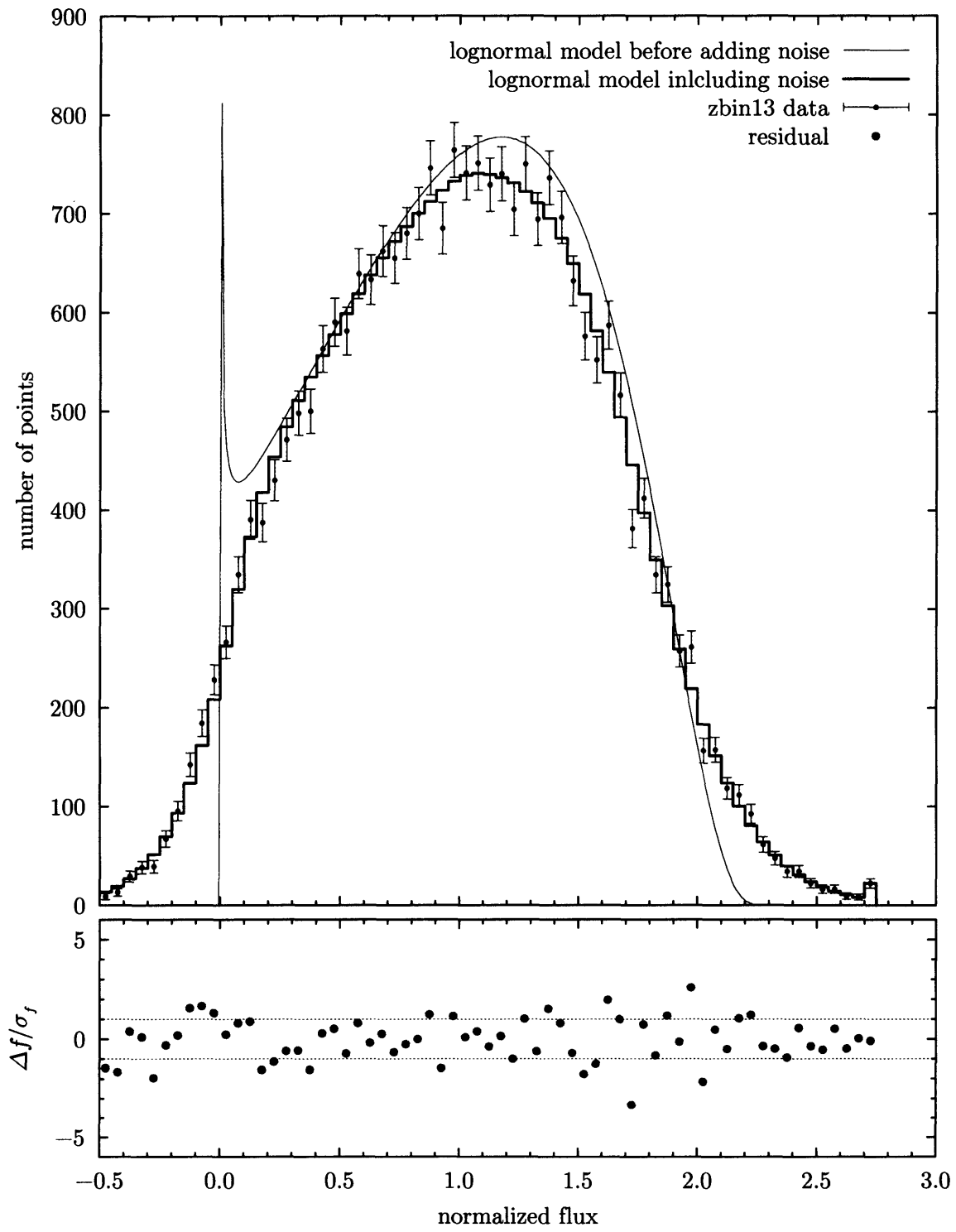


Figure 3-22: The lognormal fit for $z \sim 3.7$.

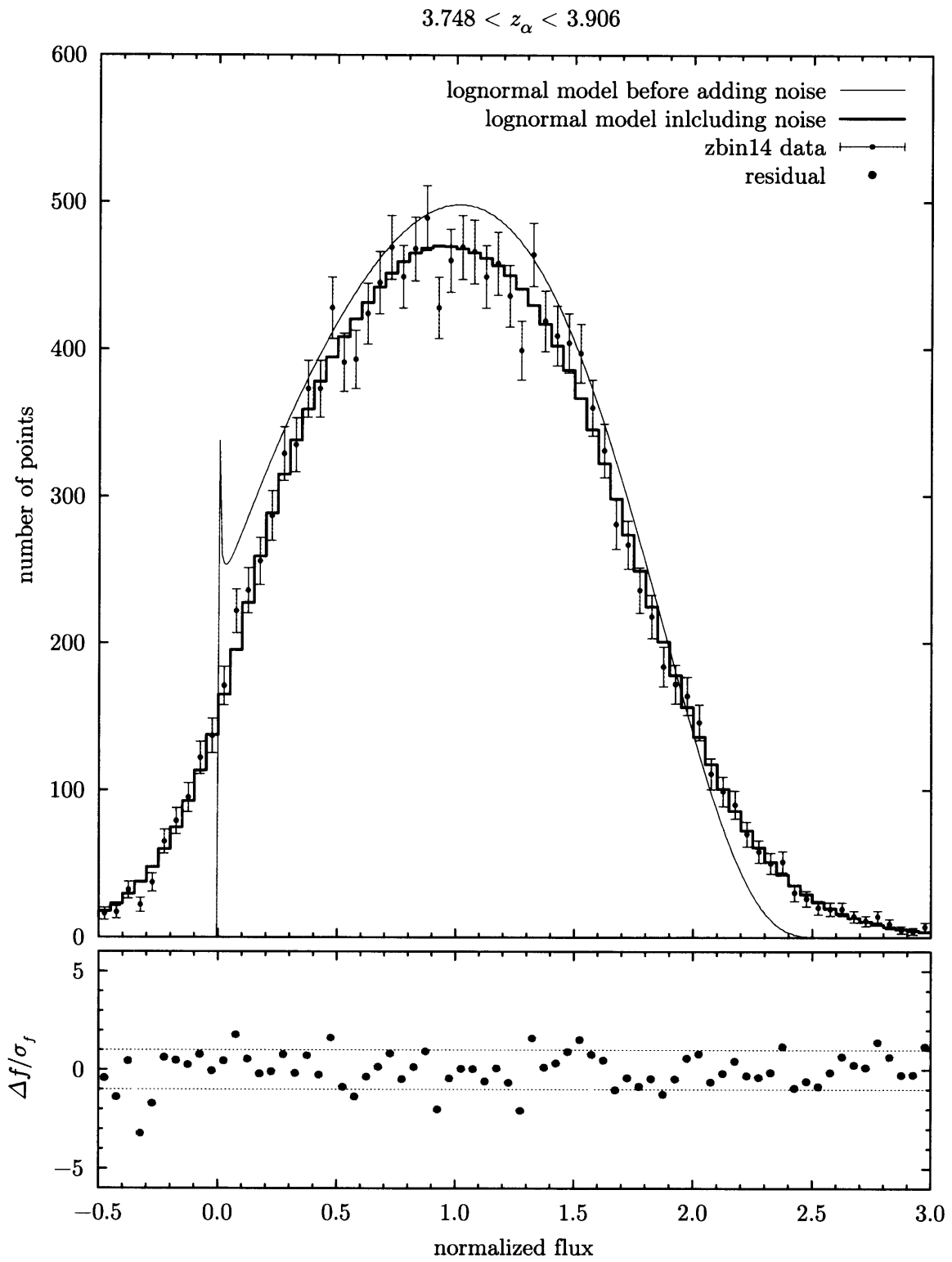


Figure 3-23: The lognormal fit for $z \sim 3.8$.

$3.906 < z_\alpha < 4.070$

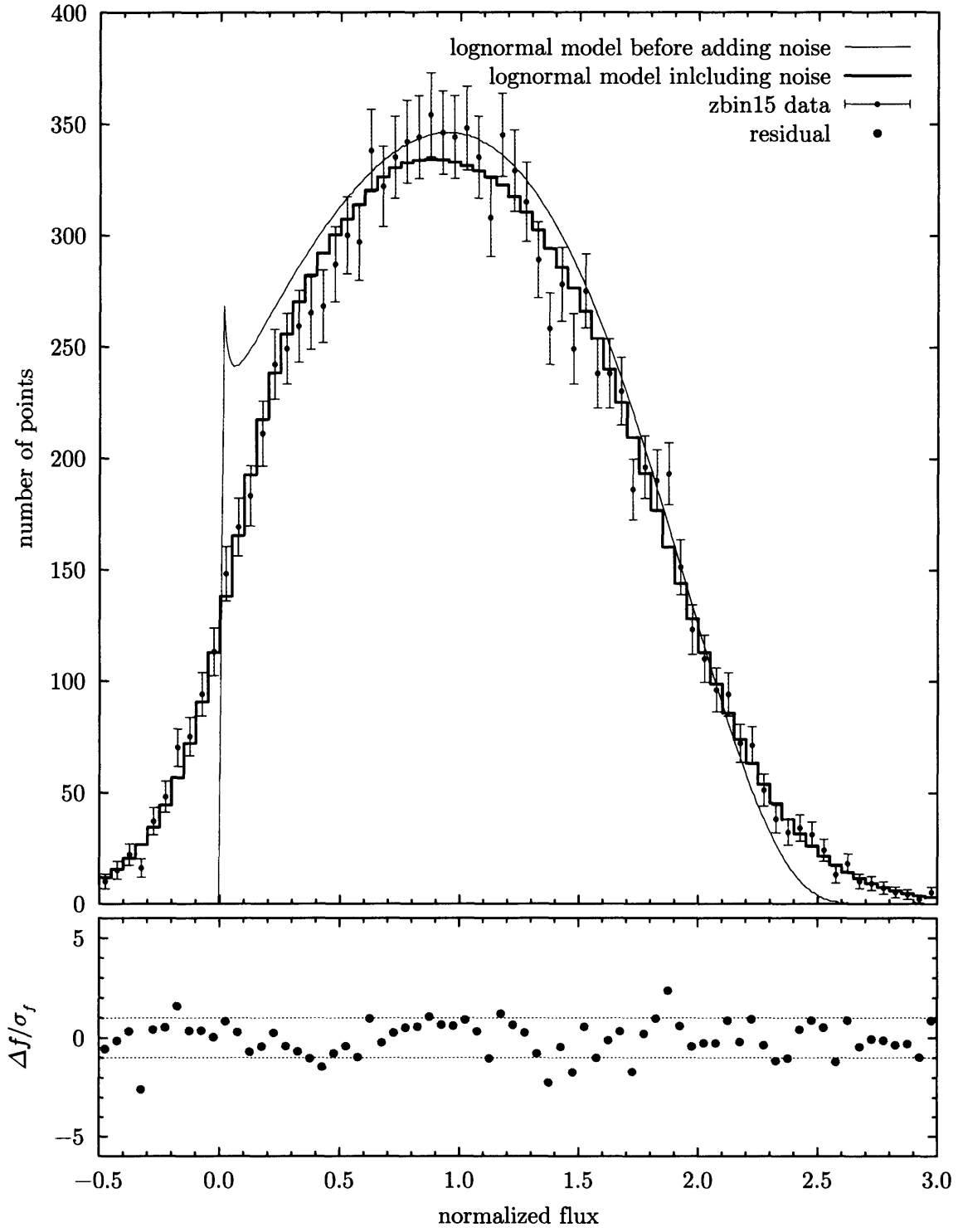


Figure 3-24: The lognormal fit for $z \sim 4.0$.

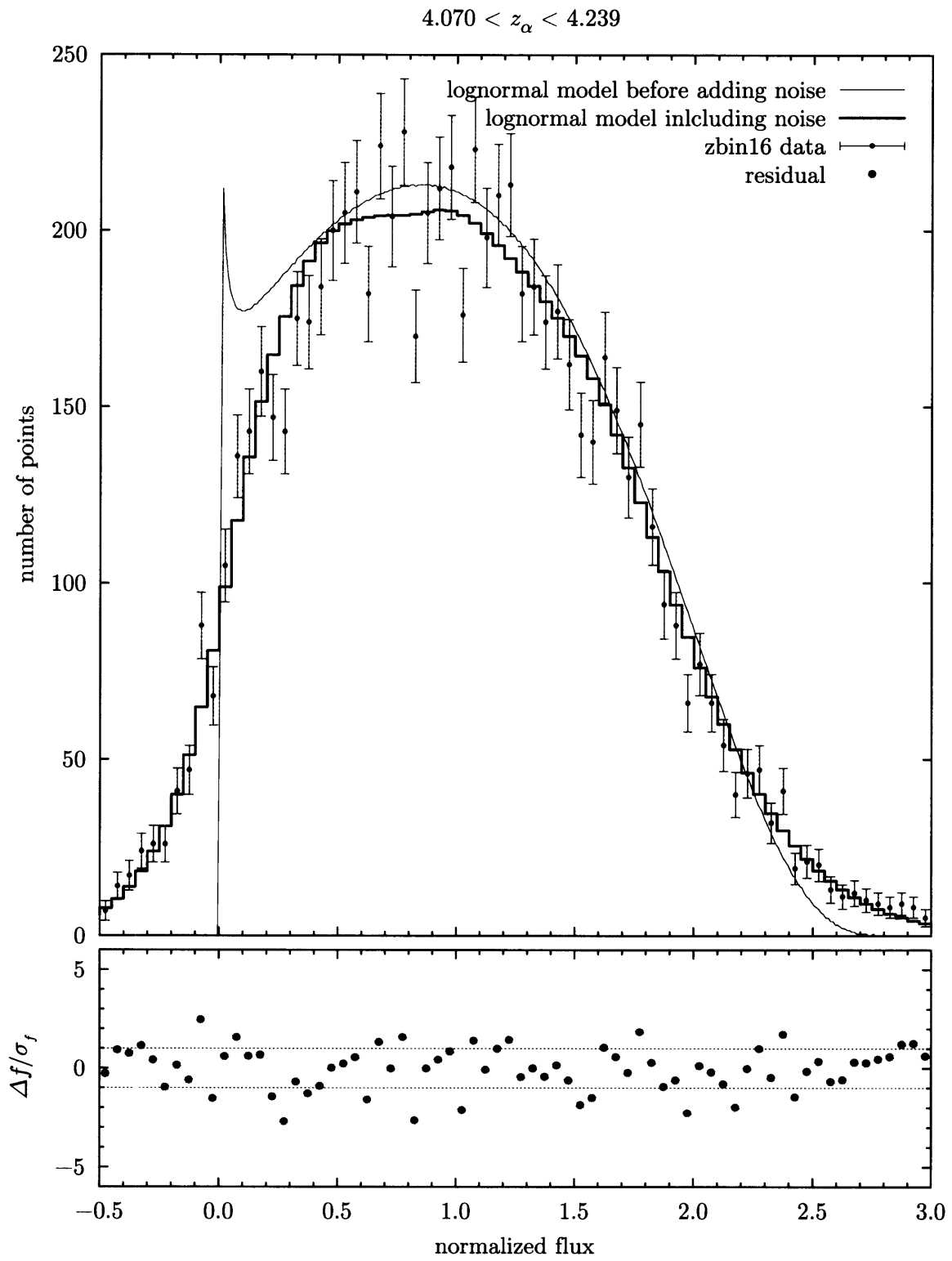


Figure 3-25: The lognormal fit for $z \sim 4.1$.

$4.239 < z_\alpha < 4.413$

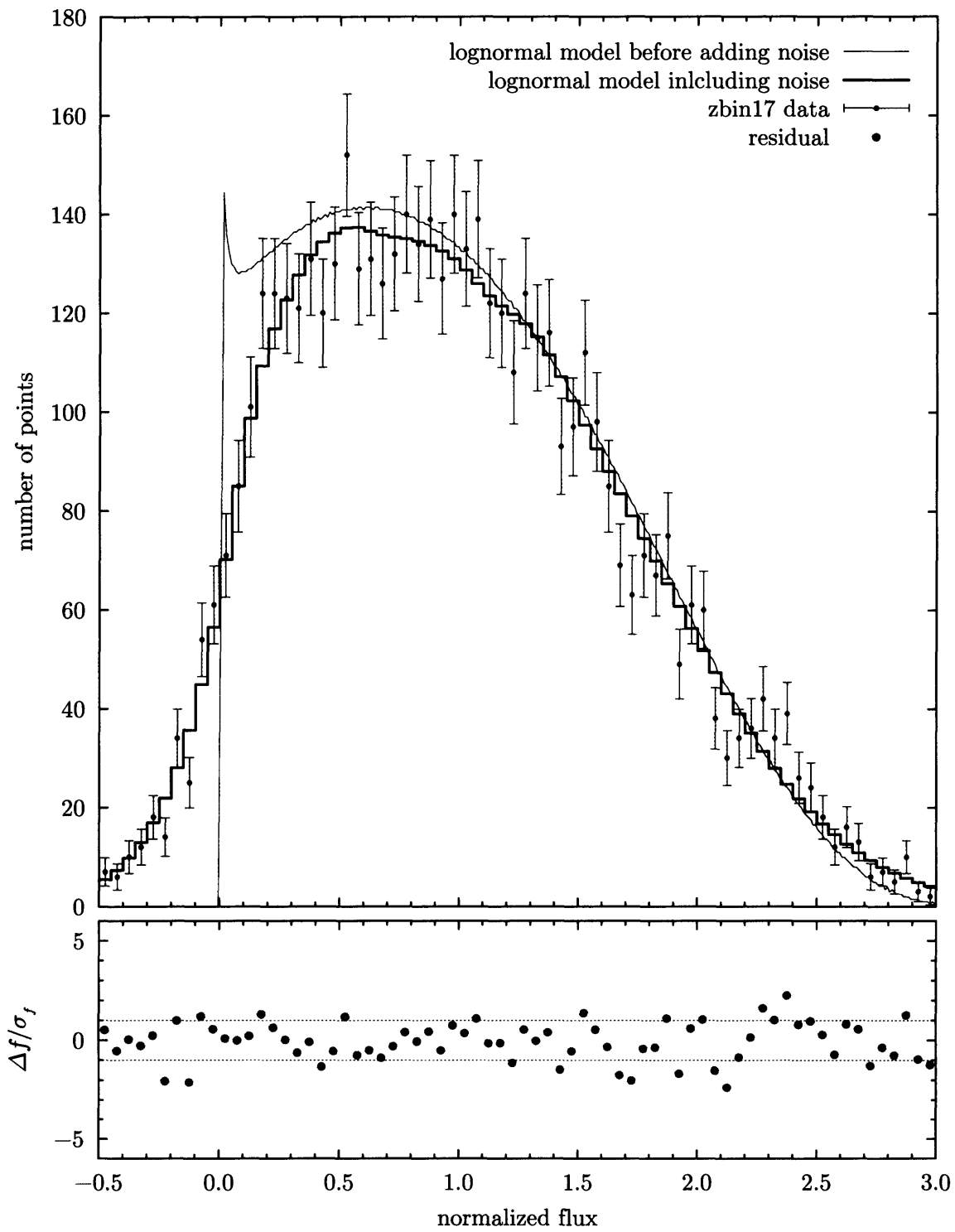


Figure 3-26: The lognormal fit for $z \sim 4.3$.

$4.413 < z_\alpha < 4.594$

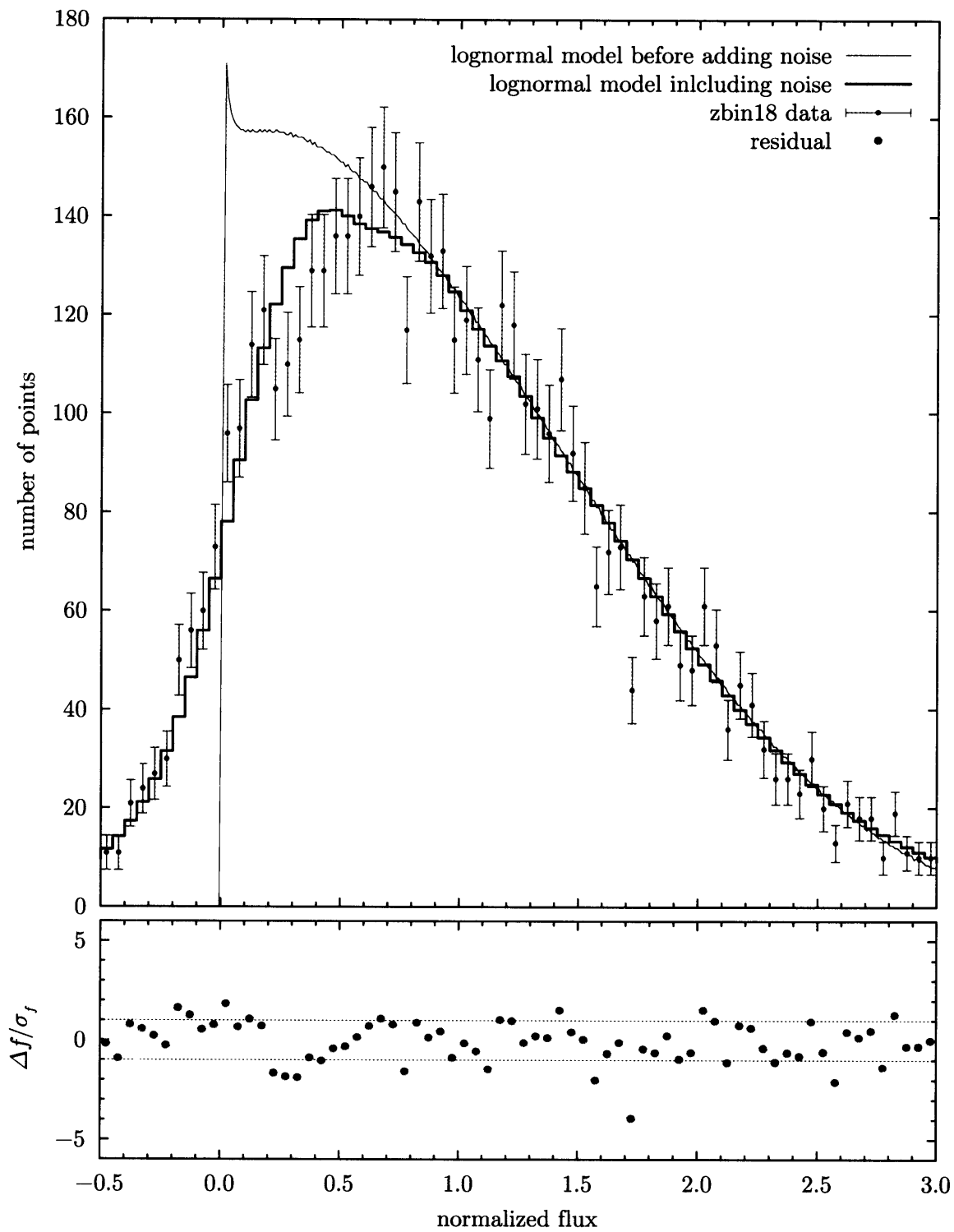


Figure 3-27: The lognormal fit for $z \sim 4.6$.

zbin	$\alpha = 2.00$				$\alpha = 1.53$			
	τ_0	σ_{τ_0}	σ_{\ln}	$\sigma_{\sigma_{\ln}}$	τ_0	σ_{τ_0}	σ_{\ln}	$\sigma_{\sigma_{\ln}}$
01	0.329	0.020	0.385	0.017	0.344	0.020	0.504	0.023
02	0.291	0.012	0.449	0.013	0.310	0.012	0.587	0.017
03	0.313	0.011	0.457	0.012	0.334	0.011	0.597	0.016
04	0.335	0.012	0.456	0.012	0.358	0.012	0.597	0.016
05	0.379	0.013	0.466	0.012	0.405	0.013	0.609	0.016
06	0.412	0.012	0.467	0.011	0.441	0.012	0.611	0.015
07	0.454	0.013	0.452	0.011	0.483	0.013	0.591	0.015
08	0.506	0.014	0.449	0.012	0.539	0.014	0.588	0.016
09	0.559	0.011	0.448	0.008	0.594	0.011	0.585	0.011
10	0.640	0.014	0.436	0.010	0.679	0.014	0.570	0.012
11	0.723	0.016	0.413	0.010	0.762	0.016	0.540	0.013
12	0.798	0.019	0.406	0.011	0.840	0.019	0.531	0.015
13	0.949	0.026	0.382	0.013	0.993	0.026	0.499	0.017
14	1.084	0.042	0.334	0.017	1.122	0.041	0.436	0.022
15	1.169	0.043	0.339	0.018	1.211	0.043	0.444	0.024
16	1.259	0.058	0.338	0.022	1.304	0.058	0.442	0.028
17	1.443	0.075	0.309	0.023	1.486	0.075	0.404	0.030
18	1.834	0.111	0.268	0.024	1.875	0.110	0.350	0.031

Table 3.3: Derived values and errors for τ_0 and σ_{\ln} . The results are given for the two limiting values of α ; to compute τ_0 and σ_{\ln} for some intermediate value of α refer to Eq. (3.15) and the results in Table 3.2.

3.6 Recovering Physical Parameters

Assuming a value for the equation of state parameter α (see Eq. (3.14)) and evaluating Eq. (3.15) for the best fit values of A and B at a given redshift bin gives the derived values of the parameters τ_0 and σ_{\ln} . The results for the two limiting cases of α are listed in Table 3.3. In the region where the lognormal model is a good fit, $z > 3$, we expect these values are actually a measurement of the underlying physical parameters in the model. However, for $z < 3$ where the lognormal model is not a good fit, the derived values of τ_0 and σ_{\ln} should be interpreted with a significant amount of skepticism.

3.6.1 Inferring $\sigma_{\ln}(z)$

Fig. 3-28 shows σ_{\ln} for the two limiting values of α . It is important to note that this parameter in the lognormal model is really an “effective variance” in the model, and cannot be directly related to either the standard cosmological parameter σ_8 or to the actual variance of the underlying of dark matter. It is noteworthy that in the $z < 3$ region where the lognormal model is not a good fit there is a significant change in the behavior of σ_{\ln} , and in fact the slope even changes sign. Changing the value of σ_{\ln} primarily effects the width of the PDF, and apparently modifying the width is the best way to compensate for the departure from lognormality. Also it is important to note that uncertainty in the value of α has a large impact on the uncertainty in σ_{\ln} .

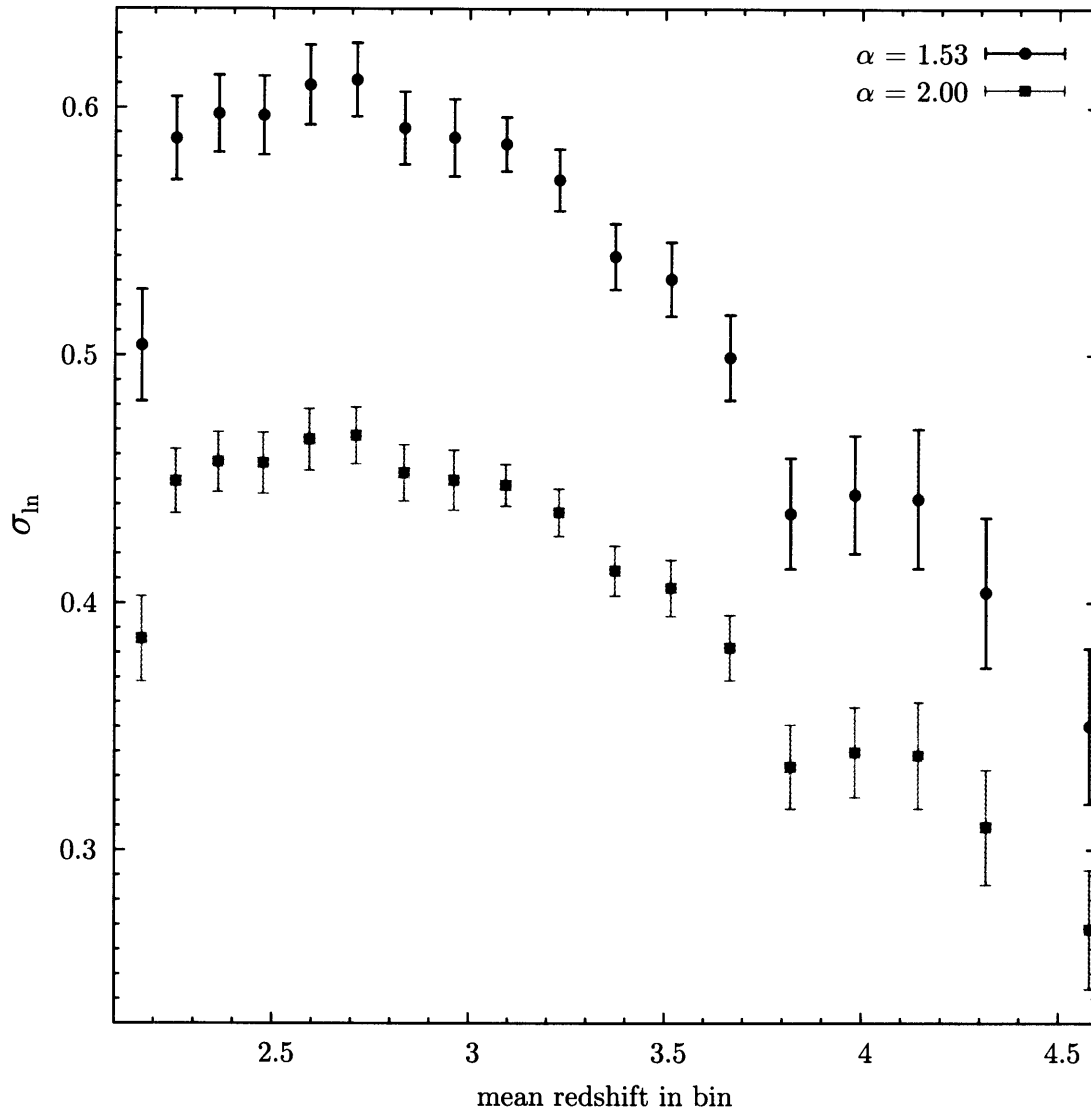


Figure 3-28: Lognormal model parameter σ_{\ln} for the two limiting values of α .

3.6.2 Inferring $\tau_0(z)$

Fig. 3-29 shows τ_0 for the two limiting values of α . A striking feature of this plot is that τ_0 shows no evidence of a change at $z < 3$ where the lognormal model fails. Rather, the function is smooth throughout the range $2.3 < z < 4.6$. With our approach, the parameter τ_0 appears to be easier to constrain than the parameter σ_{\ln} . This results from both weaker dependence on α and from the fact that the fit parameter B has larger uncertainty than the fit parameter A and the particular combination of A and B results in a larger corresponding uncertainty in σ_{\ln} than in τ_0 .

There is a very important distinction between the τ_0 that we infer and most of the optical depth results in the literature derived by careful measurement of the mean flux decrement from continuum normalized QSOs. Because of the nonlinear transformation between flux and optical depth, $f = \exp(-\tau)$, the optical depth resulting from the mean flux is not the

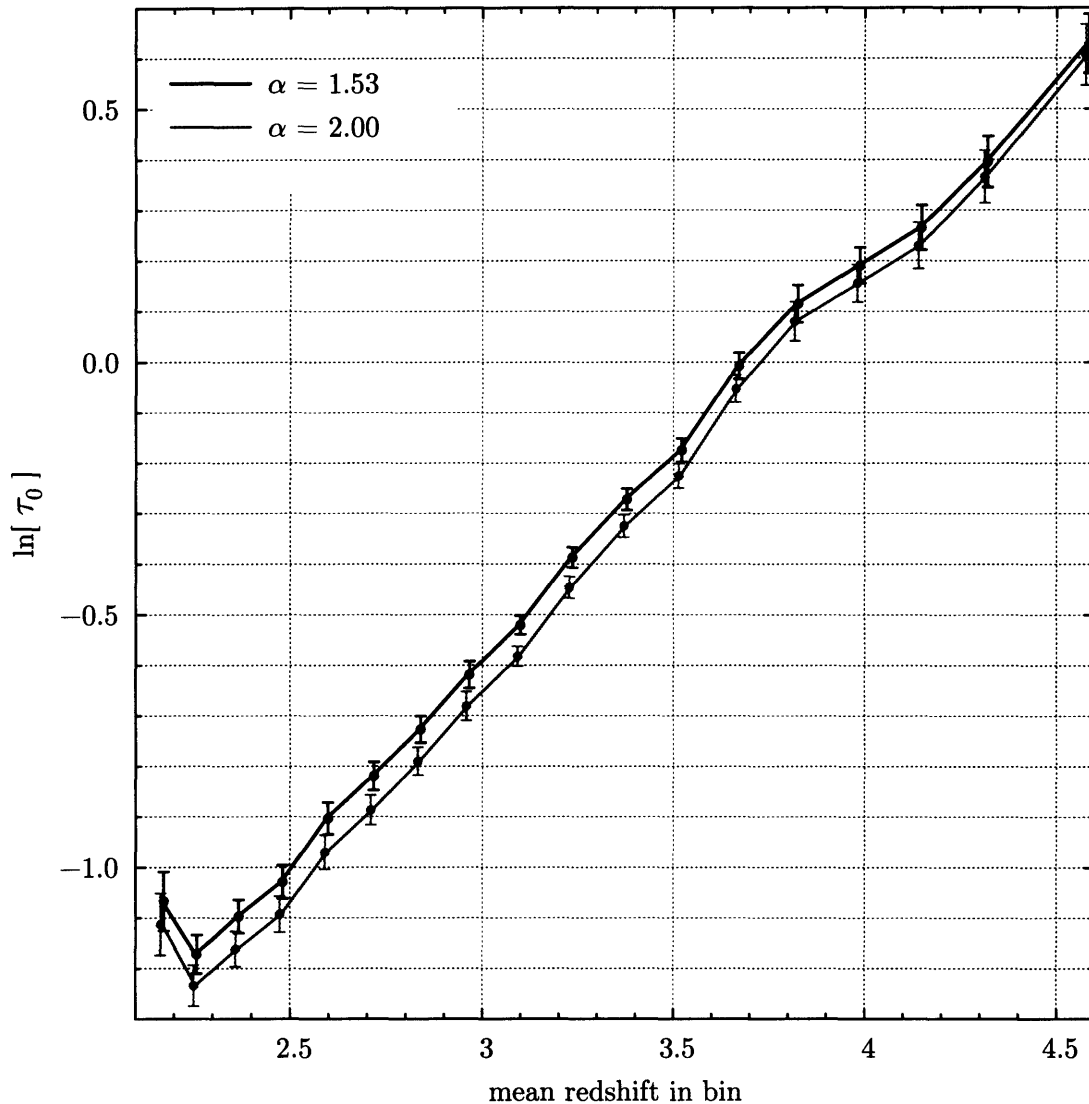


Figure 3-29: Lognormal model parameter τ_0 for the two limiting values of α .

same as the mean optical depth. In our parameterization of the lognormal model, τ_0 is precisely the *optical depth at mean density* (ie, $\tau = \tau_0$ results from $\rho = \langle \rho \rangle$, see Eq. (3.10)). In contrast, calculating the optical depth from the mean flux decrement results in measuring the *effective optical depth*, $\tau_{\text{eff}} = -\ln[\langle f \rangle]$. While these two quantities are approximately the same for $\tau \ll 1$, they are significantly different by $\tau \simeq 1$ which occurs at $z \simeq 3.7$.

We normalized each flux point in the lognormal distributions by the mean of that distribution in order to compare with the normalized SDSS data. However, we do not know what that normalization factor was for the lognormal model at each redshift bin and that is exactly the value of $\langle f \rangle$ which would have been measured from each distribution. This allows us to calculate $\tau_{\text{eff}} = -\ln[\langle f \rangle]$ directly so that we may compare to other measurements of the effective optical depth. Fig. 3-30 shows our calculation of τ_{eff} (red curve) compared to the longstanding power law fit of Press et al. (1993) (blue curve). For comparison, our measurement of τ_0 for the case of $\alpha = 1.53$ (dashed line) from Fig. 3-29 is also plotted

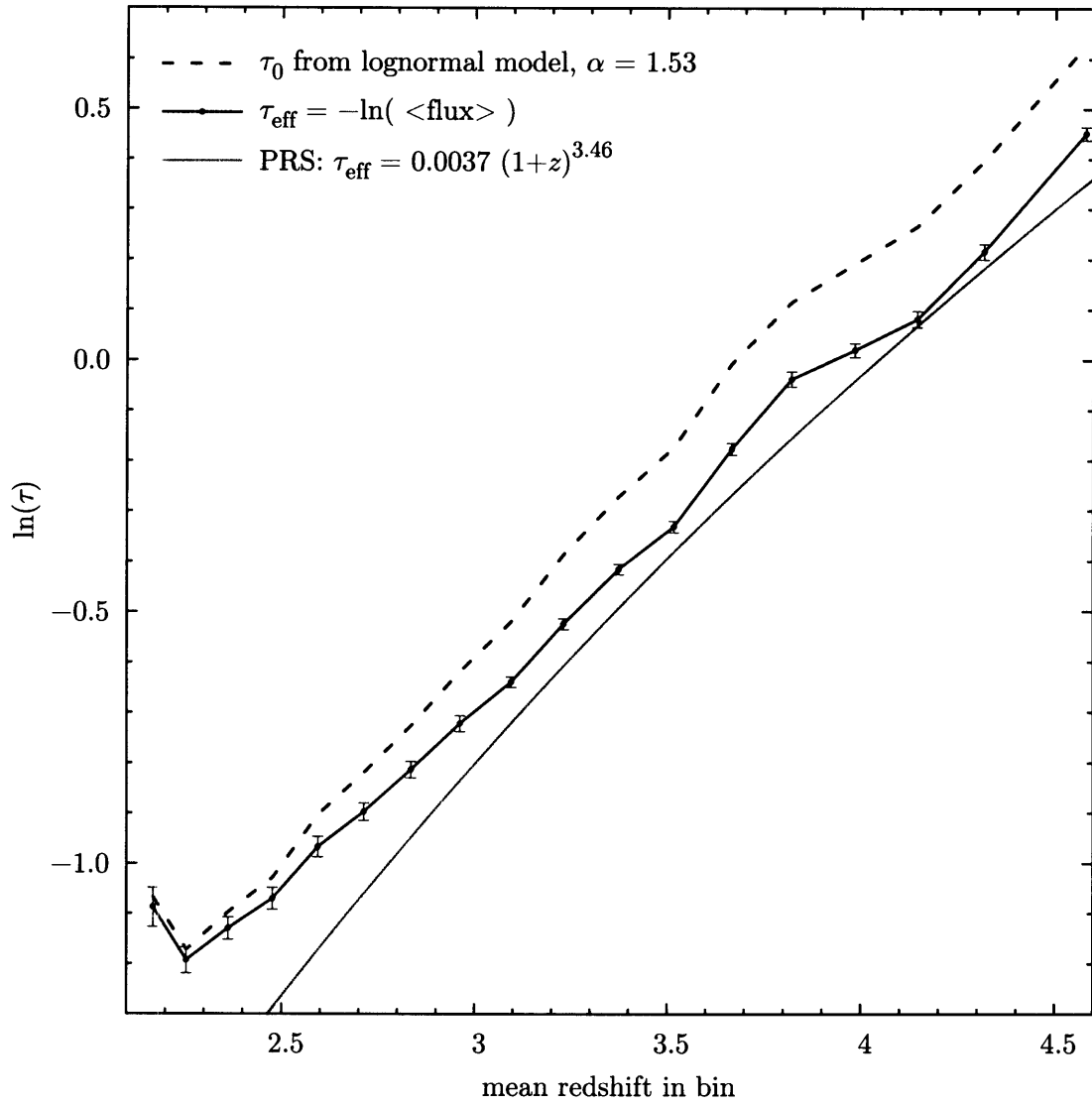


Figure 3-30: τ_0 and τ_{eff} , compared to other measurements.

(the error bars are omitted for clarity). From this comparison the difference between mean optical depth and effective optical depth at large redshifts is apparent.

3.7 Conclusions

The lognormal model is a good fit to the Lyman- α forest flux PDF for $z > 3$. The most significant result we derive from this fit is the redshift dependence of the optical depth at mean density, τ_0 . This physical quantity is necessary to properly normalize the Lyman- α forest power spectrum, and our results provide a new and independent measurement of τ_0 . Our uncertainty in determining τ_0 is between 2% and 6% depending on the redshift, and at this point we are limited by systematic errors and the uncertainty in the parameter α .

It is interesting to consider why the lognormal model fails rather abruptly at $z \simeq 3$; is it an indication of a physical change in the universe at that redshift, or is it simply an artifact of something in the observations? HeII reionization is expected to have occurred somewhere in the rough range of $2 \lesssim z \lesssim 4$, and this transition would heat the IGM and likely imprint a signature into the optical depth at that redshift. Bernardi et al. (2003) found evidence for a dip in τ_{eff} at a redshift of $z \simeq 3.2$, but our optical depth function is very smooth through the entire redshift range and we see no feature near $z \simeq 3.2$. Though it is possible to imagine how the HeII reionization transition could perturb the density distribution and be related to the failure of the lognormal model we see at $z \simeq 3$, it is hard to imagine how it could do so without also imprinting a feature in the optical depth.

The parameter τ_0 is also directly related to the cosmic baryon density, the temperature of the intergalactic medium, and the extragalactic ionizing background. Neither of the latter two have been well measured by other methods, and so measurements of τ_0 provide an important constraint on these quantities fundamental to the physics of the IGM.

Clearly further work is necessary to understand the nature of the departure from log-normality. Including higher order moments in the distribution are a natural next step, but we also need to test for contamination by metal line absorption and Lyman limit systems. Despite the shortcomings at lower redshift, at higher redshifts we are able to describe a huge set of data with just a few parameters and all tests show we characterize the flux PDF at SDSS resolution for $z > 3$. We hope to use these results to make the comparison of simulations of the Lyman- α forest with SDSS observables significantly easier.

Appendix A

FFT Normalization Conventions

Most of these equations are redundant to the equations in chapter 2, but reproduced here all together for completeness and in somewhat more detail.

A.1 Setup

To convert between the usual integrals and discrete sums on the lattice:

$$\int dx f(x) = \sum_x \Delta x f(x) = \left(\frac{b}{Q}\right) \sum_x f(x) \quad (\text{A.1a})$$

$$\int dk f(k) = \sum_k \Delta k f(k) = \left(\frac{2\pi}{b}\right) \sum_k f(k). \quad (\text{A.1b})$$

The Fourier transform conventions are constructed with an arbitrary normalization parameter η carried through to all formulae. Thus, the formulae can be specialized to any particular convention at the end (moreover, it becomes obvious which expressions depend on this convention, and in which it cancels entirely). When $\eta = 1$ these formulae all agree with the conventions used in Alan's notes (and, for now at least, my thesis), while when $\eta = 2\pi$ the formulae follow the more "typical" conventions (where wavenumber always occurs as $k/2\pi$):

$$f(x) = \frac{1}{\eta} \int dk e^{ikx} f(k) = \left(\frac{2\pi}{b\eta}\right) \sum_k e^{ikx} f(k) \quad (\text{A.2a})$$

$$f(k) = \frac{\eta}{2\pi} \int dx e^{-ikx} f(x) = \left(\frac{b\eta}{2\pi Q}\right) \sum_x e^{-ikx} f(x) \quad (\text{A.2b})$$

Double check the normalization:

$$f(x) = \left(\frac{2\pi}{b\eta}\right) \sum_k e^{ikx} f(k) \quad (\text{A.3a})$$

$$= \left(\frac{2\pi}{b\eta}\right) \sum_k e^{ikx} \left[\left(\frac{b\eta}{2\pi Q}\right) \sum_{x'} e^{-ikx'} f(x') \right] \quad (\text{A.3b})$$

$$= \left(\frac{1}{Q}\right) \sum_{x'} Q \delta_{x,x'} f(x') \quad (\text{A.3c})$$

$$= f(x) \tag{A.3d}$$

By definition the mean fluctuations are measured by:

$$\Delta f(k) \equiv \left[\frac{k}{2\pi} \int dx e^{ikx} \langle f(x) f(0) \rangle \right]^{\frac{1}{2}} \tag{A.4a}$$

$$= \left[\frac{k}{2\pi} \frac{b}{Q} \sum_x e^{ikx} \left\langle \left(\frac{2\pi}{b\eta} \right) \sum_{k'} e^{ik'x} f(k') \left(\frac{2\pi}{b\eta} \right) \sum_{k''} f(k'') \right\rangle \right]^{\frac{1}{2}} \tag{A.4b}$$

$$= \left[\frac{2\pi k}{bQ\eta^2} \sum_{k'} \sum_{k''} \sum_x e^{i(k+k')x} \langle f(k') f(k'') \rangle \right]^{\frac{1}{2}} \tag{A.4c}$$

$$= \left[\frac{2\pi k}{bQ\eta^2} \sum_{k'} \sum_{k''} Q \delta_{k,-k'} \langle f(k') f(k'') \rangle \right]^{\frac{1}{2}} \tag{A.4d}$$

$$= \left[\frac{2\pi k}{b\eta^2} \sum_{k''} \langle f(-k) f(k'') \rangle \right]^{\frac{1}{2}} \tag{A.4e}$$

$$= \left[\frac{2\pi k}{b\eta^2} \langle |f(k)|^2 \rangle \right]^{\frac{1}{2}}. \tag{A.4f}$$

A.2 Monte Carlo Calculation

For a complex scalar field $\phi(x, t)$ in one dimension, independent of FFT normalization (the coefficient here is set to make the c, d commutator normalization unity):

$$\phi(x, t) = \frac{1}{\sqrt{b}} \sum_k e^{ikx} \left[c(k)u(k, t) + d^\dagger(-k)u^*(-k, t) \right]. \tag{A.5}$$

The Fourier transform of the field is:

$$\phi(k, t) = \frac{b\eta}{2\pi Q} \sum_x e^{-ikx} \phi(x, t) \tag{A.6a}$$

$$= \frac{\eta\sqrt{b}}{2\pi} \left[c(k)u(k, t) + d^\dagger(-k)u^*(-k, t) \right]. \tag{A.6b}$$

Rewriting this in the form input to the FFT routine:

$$\Im[\phi(k, t)] = \frac{\eta}{2\pi} \sqrt{\frac{b}{2k}} R \left((a_2 - a_4) \cos \theta + (a_1 - a_3) \sin \theta \right) \tag{A.7a}$$

$$\Re[\phi(k, t)] = \frac{\eta}{2\pi} \sqrt{\frac{b}{2k}} R \left((a_1 + a_3) \cos \theta - (a_2 + a_4) \sin \theta \right). \tag{A.7b}$$

Numerical Recipes leaves the normalization to you to apply:

$$\phi(x, t) = \frac{2\pi}{b\eta} FFT[\phi(k, t)]. \tag{A.8}$$

The procedure is to then compare $|\phi(x, t)| \equiv \left(\Re[\phi(x, t)]^2 + \Im[\phi(x, t)]^2 \right)^{\frac{1}{2}}$ to the value of the constant ϕ_{end} to find the time delay field $\tau(x)$. Again the normalization to the Numerical Recipes output is applied by hand:

$$\tau(k) = \frac{b\eta}{2\pi Q} \text{FFT}[\tau(x)]. \quad (\text{A.9})$$

Thus, here is the expression for the final result using Monte Carlo approach:

$$\Delta\tau_{\text{mc}}(k) = \left[\frac{2\pi k}{b\eta^2} \langle |\tau(k)|^2 \rangle \right]^{\frac{1}{2}}. \quad (\text{A.10})$$

Note that η cancels out if you put it in terms of “unnormalized” FFT output. However, the $1/Q$ factor is not a matter of convention, but a necessary normalization which would be built into any standard FFT routine so keep it grouped with the FFT. The factor of $1/N_m$ is simply from replacing the $\langle \text{average} \rangle$ by a sum to make explicit the prescription:

$$\Delta\tau_{\text{mc}}(k) = \left[\frac{2\pi k}{b\eta^2} \frac{b^2\eta^2}{4\pi^2 Q^2} \left(\sum \text{FFT}[\tau(x)]^2 / N_m \right) \right]^{\frac{1}{2}} \quad (\text{A.11a})$$

$$= \sqrt{\frac{kb}{2\pi}} \left[\frac{1}{N_m} \sum_{\text{modes}} \left(\frac{1}{Q} \text{FFT}[\tau(x)] \right)^2 \right]^{\frac{1}{2}}. \quad (\text{A.11b})$$

A.3 Analytic Approach

In this case rather than computing $\phi(x, t)$ directly we work with the RMS value:

$$\phi_{\text{rms}}(t) \equiv \langle \mathbf{0} | \phi^*(x) \phi(x) | \mathbf{0} \rangle^{\frac{1}{2}} \quad (\text{A.12a})$$

$$= b^{-1} \sum_k \sum_{k'} e^{-ikx} e^{ik'x} \langle \mathbf{0} | \left(c_k^\dagger u_k^* + d_{-k} u_{-k} \right) \left(c_{k'} u_{k'} + d_{-k'}^\dagger u_{-k'}^* \right) | \mathbf{0} \rangle \quad (\text{A.12b})$$

$$= b^{-1} \sum_k \sum_{k'} e^{i(k'-k)x} |u_k|^2 \delta_{k,k'} \quad (\text{A.12c})$$

$$= \left(\frac{1}{b} \sum_k \frac{R(k, t)^2}{2|k|} \right)^{\frac{1}{2}}. \quad (\text{A.12d})$$

And its derivative:

$$\dot{\phi}_{\text{rms}}(t) = \frac{1}{\sqrt{2b}} \left(\sum_k \frac{R(k, t)^2}{|k|} \right)^{-\frac{1}{2}} \left(\sum_k \frac{R(k, t) \dot{R}(k, t)}{|k|} \right). \quad (\text{A.13})$$

The correlation in the field $\phi(k, t)$ is:

$$\Delta\phi(k, t) = \left[\frac{2\pi k}{b\eta^2} \langle \phi^*(k) \phi(k) \rangle \right]^{\frac{1}{2}} \quad (\text{A.14a})$$

$$= \left[\frac{2\pi k}{b\eta^2} \frac{b\eta^2}{(2\pi)^2} \langle \mathbf{0} | \left(c_k^\dagger u_k^* + d_{-k} u_{-k} \right) \left(c_k u_k + d_{-k}^\dagger u_{-k}^* \right) | \mathbf{0} \rangle \right]^{\frac{1}{2}} \quad (\text{A.14b})$$

$$= \left[\frac{k}{2\pi} |u(k, t)|^2 \right]^{\frac{1}{2}} \quad (\text{A.14c})$$

$$= \left[\frac{k}{2\pi} \frac{R(k, t)^2}{2|k|} \right]^{\frac{1}{2}} \quad (\text{A.14d})$$

$$= \frac{R(k, t)}{2\sqrt{\pi}}. \quad (\text{A.14e})$$

Put this together to get the result for the analytic approach:

$$\Delta\tau_{\text{ana}}(k) = \frac{\Delta\phi(k, t)}{\dot{\phi}_{\text{rms}}(t)} \quad (\text{A.15a})$$

$$= \frac{R(k, t)}{2\sqrt{\pi}} \sqrt{2b} \left(\sum_k \frac{R(k, t)^2}{|k|} \right)^{\frac{1}{2}} \left(\sum_k \frac{R(k, t) \dot{R}(k, t)}{|k|} \right)^{-1} \quad (\text{A.15b})$$

$$= \sqrt{\frac{b}{2\pi}} R(k, t) \left(\sum_k \frac{R(k, t)^2}{|k|} \right)^{\frac{1}{2}} \left(\sum_k \frac{R(k, t) \dot{R}(k, t)}{|k|} \right)^{-1} \quad (\text{A.15c})$$

This expression is evaluated at a time $t = t_{\text{ana}}$, roughly the mean ending time for inflation in the Monte Carlo simulations.

Lastly, compare the two cases directly. Out of convenience define:

$$\mathcal{A}(t) \equiv \left(\sum_k \frac{R(k, t)^2}{|k|} \right)^{\frac{1}{2}} \left(\sum_k \frac{R(k, t) \dot{R}(k, t)}{|k|} \right)^{-1} \quad (\text{A.16})$$

$$\mathcal{B} \equiv \left[\frac{1}{N} \sum_{\text{modes}} \left(\frac{1}{Q} \text{FFT}[\tau(x)] \right)^2 \right]^{\frac{1}{2}} \quad (\text{A.17})$$

which gives the ratio:

$$\frac{\Delta\tau_{\text{ana}}(k)}{\Delta\tau_{\text{mc}}(k)} = \sqrt{\frac{b}{2\pi}} R(k, t) \mathcal{A}(t) \left[\sqrt{\frac{kb}{2\pi}} \mathcal{B} \right]^{-1} \quad (\text{A.18})$$

$$= \frac{R(k, t)}{\sqrt{k}} \frac{\mathcal{A}(t)}{\mathcal{B}} \Big|_{t=t_{\text{ana}}} \quad (\text{A.19})$$

Since \mathcal{A} and \mathcal{B} are independent of any normalization conventions we see that yes in fact this ratio is also independent of normalization conventions, as must be the case. Furthermore, written in terms of $|u(k, t)| = R(k, t)/\sqrt{2|k|}$ (including modifying the expression in \mathcal{A} accordingly to be expressed in terms of u in place of R , which results in $\mathcal{A}' = \sqrt{2}\mathcal{A}$) the expression is even simpler:

$$\frac{\Delta\tau_{\text{ana}}(k)}{\Delta\tau_{\text{mc}}(k)} = u(k, t) \frac{\mathcal{A}'(t)}{\mathcal{B}} \Big|_{t=t_{\text{ana}}} \quad (\text{A.20})$$

Appendix B

PCA Normalization

The goal is to normalize each QSO by its “mean spectrum” as estimated by examination of the entire sample. This Appendix describes the steps in this procedure.

B.1 Useful Relations

To get the (observed) wavelength of the i^{th} pixel in a SDSS spectrum

$$\lambda_i = 10^{(i \cdot \text{DLOGLAMBDA} + \text{LOGLAMBDA0})} \quad (\text{B.1})$$

where i runs from 0 to `NPIXELS-1`. To shift this to rest wavelength,

$$\Delta \text{LOGLAMBDA0} = -\log_{10}(1 + z_{\text{qso}}). \quad (\text{B.2})$$

B.2 Normalize Each Spectrum by its Median

There is a lot of variation in the brightness of each QSO, so the first step is to rescale each spectrum so that the flux is on a similar scale. For each spectrum we find the median flux value for that spectrum by calculating the median of all points in the range 1270 – 2000Å in rest wavelength, dropping any points with inverse variance equal to zero. We then divide each (entire) spectrum by its median. This is of course only a crude normalization, but the steps in the remainder of this Appendix will refine it. For the i^{th} spectrum, this normalized flux is given by

$$\text{normflux0}[\lambda, i] = \frac{\text{flux}[\lambda, i]}{\text{medianflux0}[i]} \quad (\text{B.3})$$

The notation “`flux`[λ , i]” is shorthand for “the flux value corresponding to the pixel with wavelength λ of the i^{th} spectrum.”

B.3 Construct First Median Spectrum Template

Using the set of `normflux0` spectra, construct a single composite spectrum, `median1`, which is the median flux across all lines of sight as a function of rest wavelength. Throughout

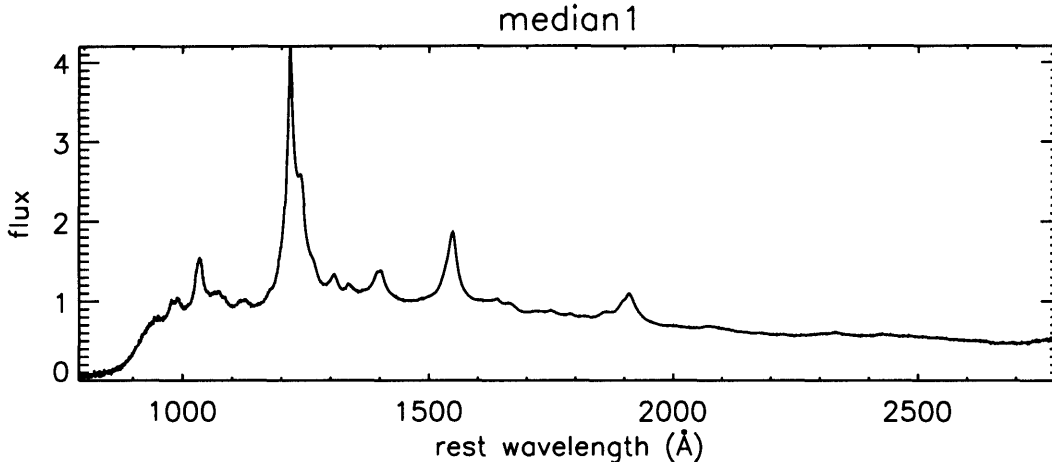


Figure B-1: First median composite, `median1`.

this chapter the symbol λ will refer to *rest wavelength*¹. We will use this composite as a template to fit to in the next section. Again dropping points with inverse variance equal to zero, find the median flux at each rest wavelength λ represented in the QSO sample:

$$\text{median1}[\lambda] = (\text{median of all normflux0 points at that } \lambda). \quad (\text{B.4})$$

Fig. B-1 show a plot of `median1`. Note that this composite spectrum will cover a wider range of rest wavelengths than any individual spectrum since QSOs at different redshifts will cover different ranges of λ .

B.4 Fit Median Template to Remove Tilt and Offset

We now use `median1` as a template which we can fit to each individual spectrum to remove any tilt or normalization. Once we know the tilt we can divide by it to “flatten” each spectrum. The idea here is that by untilting the underlying continuum, the set of spectra will be more homogeneous and thus produce a cleaner result when combined to create the redshift dependent composite in step B.6.

For each spectra we fit `median1` to `normflux0` in log wavelength space, allowing the relative tilt and offset to be free parameters. In other words, we find the the values of A and B which result in the best fit to

$$\text{normflux0}[\lambda, i] = \text{median1}[\lambda] \cdot 10^{A_i} \lambda^{B_i} \quad (\text{B.5})$$

$$\log\left(\frac{\text{normflux0}[\lambda, i]}{\text{median1}[\lambda]}\right) = A_i + B_i \log(\lambda). \quad (\text{B.6})$$

The fit is performed over the continuum portion of the spectrum; we chose the range $1270 < \lambda < 2000\text{\AA}$, identical to the range in section B.2.

For each spectrum we find the values of A and B which result in the best fit to the template. This allows us to then use these values to produce an untilted spectrum, `normflux1`,

¹The rest wavelength λ , the observed wavelength λ_{obs} , and the redshift of the QSO z_{qso} are related via: $\lambda_{\text{obs}}/\lambda = 1 + z_{\text{qso}}$

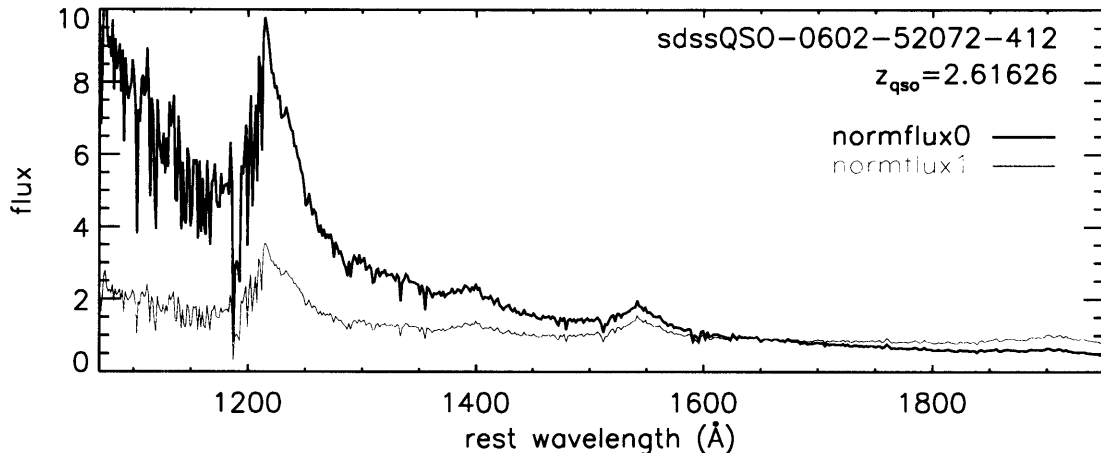


Figure B-2: An example spectrum before and after tilt.

via the transformation

$$\text{normflux1}[\lambda, i] = \frac{\text{normflux0}[\lambda, i]}{\text{tilt1}[\lambda, i]} \quad (\text{B.7})$$

where

$$\text{tilt1}[\lambda, i] = 10^{A_i + B_i \log(\lambda)}. \quad (\text{B.8})$$

An example of a particularly large tilt is shown in Fig. B-2.

B.5 Second Pass at Median Normalization and Fitting

If the previous step revealed a wide variation in the underlying tilt, it would be worth repeating steps B.3 and B.4 again. Using the newly untilted fluxes `normflux1`, again median across all lines of sight as a function of rest wavelength to produce a new median composite (`median2`). This time the composite should be cleaner since the untilted fluxes will be closer to the median at each λ . Now use this template in place of `median1` to fit the tilt and normalization to `normflux0`. In practice, however, `median2` is similar enough to `median1` in the region the fit is done over that this extra iteration is unnecessary. Fig. B-3 shows a plot of the residual between `median2` and `median1`.

B.6 B-spline to Construct Redshift-dependent Template

Up until now we have been fitting the same single template to each spectrum. But we know that in reality the “generic spectrum” of a high redshift QSO will not be the same as that of a low redshift QSO, and that a more accurate template would reflect this. So, now that we have our set of normalized untilted spectra, `normflux1`, we are ready to make this final redshift dependent composite.

The idea is again to align all spectra in rest wavelength, but now also to sort them by redshift. Then rather than collapsing all flux values at some rest wavelength λ to find

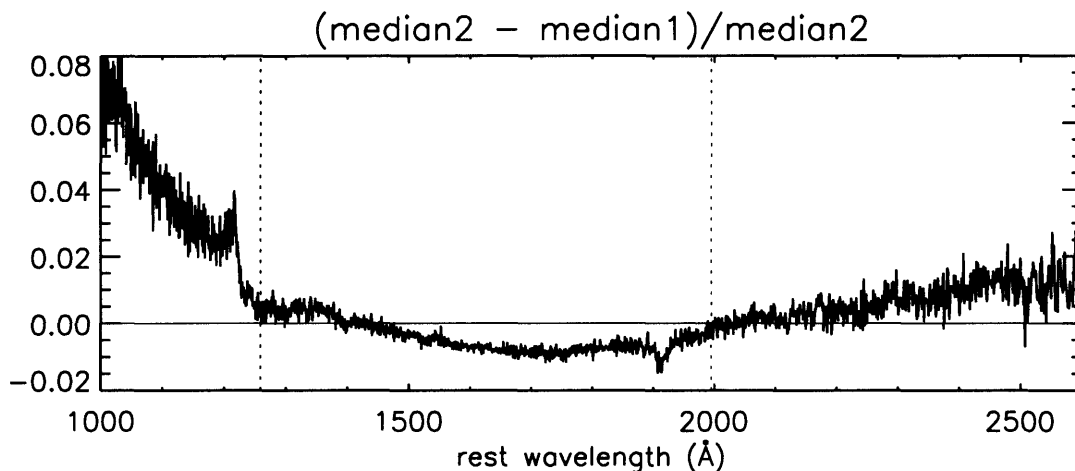


Figure B-3: Difference between creating median composite before untilting (`median1`) and after (`median2`). Note that the fit is only performed over the region $1259 < \lambda < 1995$ Å (in between the vertical dotted lines) where the difference is small.

the median, fit a low order polynomial (we use a quadratic) to the column of flux, as a function of \log *observed* wavelength (interchangeable with the redshift of the QSO). Doing this at each rest wavelength will then give you not just a single value of median flux at that λ , rather it will give you average flux as a function of observed wavelength at that λ . In this way we can form `bspline_median` $[\lambda, i]$. The i^{th} line of this array is analogous to `median1` $[\lambda]$, only now provides a more accurate median template appropriate for the redshift of the i^{th} QSO.

B.7 Third Pass at Fit Tilt and Offset, with B spline Median

Now repeat the procedure in section B.4, using `bspline_median` $[\lambda, i]$ in place of `median1` $[\lambda]$. Also we choose to fit these templates to the original `flux` $[\lambda, i]$ points, rather than to `normflux` $[\lambda, i]$, so that we obtain one overall tilt and offset rather than a third incremental change. This way there is a very simple transformation between the final normalized and untilted spectra and the raw spectra we began with. The new tilts found in this way are `bspline_tilt` $[\lambda, i]$.

B.8 Do PCA Fit

Finally, fit the residual delta:

$$\text{delta}[\lambda, i] = \frac{\text{flux}[\lambda, i]}{\text{bspline_tilt}[\lambda, i] \cdot \text{bspline_median}[\lambda, i]} \quad (\text{B.9})$$

$$\text{deltaivar}[\lambda, i] = \text{invvar}[\lambda, i] \left(\text{bspline_tilt}[\lambda, i] \cdot \text{bspline_median}[\lambda, i] \right)^2 \quad (\text{B.10})$$

$$\text{compositenormalized}[\lambda, i] = 1 + \text{delta}[\lambda, i] \quad (\text{B.11})$$

$$= \frac{\text{flux}[\lambda, i]}{\text{bspline_tilt}[\lambda, i] \cdot \text{bspine_median}[\lambda, i]} \quad (\text{B.12})$$

$$\text{deltaivar}[\lambda, i] = \text{invvar}[\lambda, i] \left(\text{bspline_tilt}[\lambda, i] \cdot \text{bspine_median}[\lambda, i] \right)^2 \quad (\text{B.13})$$

At this point a standard principal component analysis (PCA) fit is performed to find the eigen-spectra in the continuum, and then predict the mean normalization in the forest.

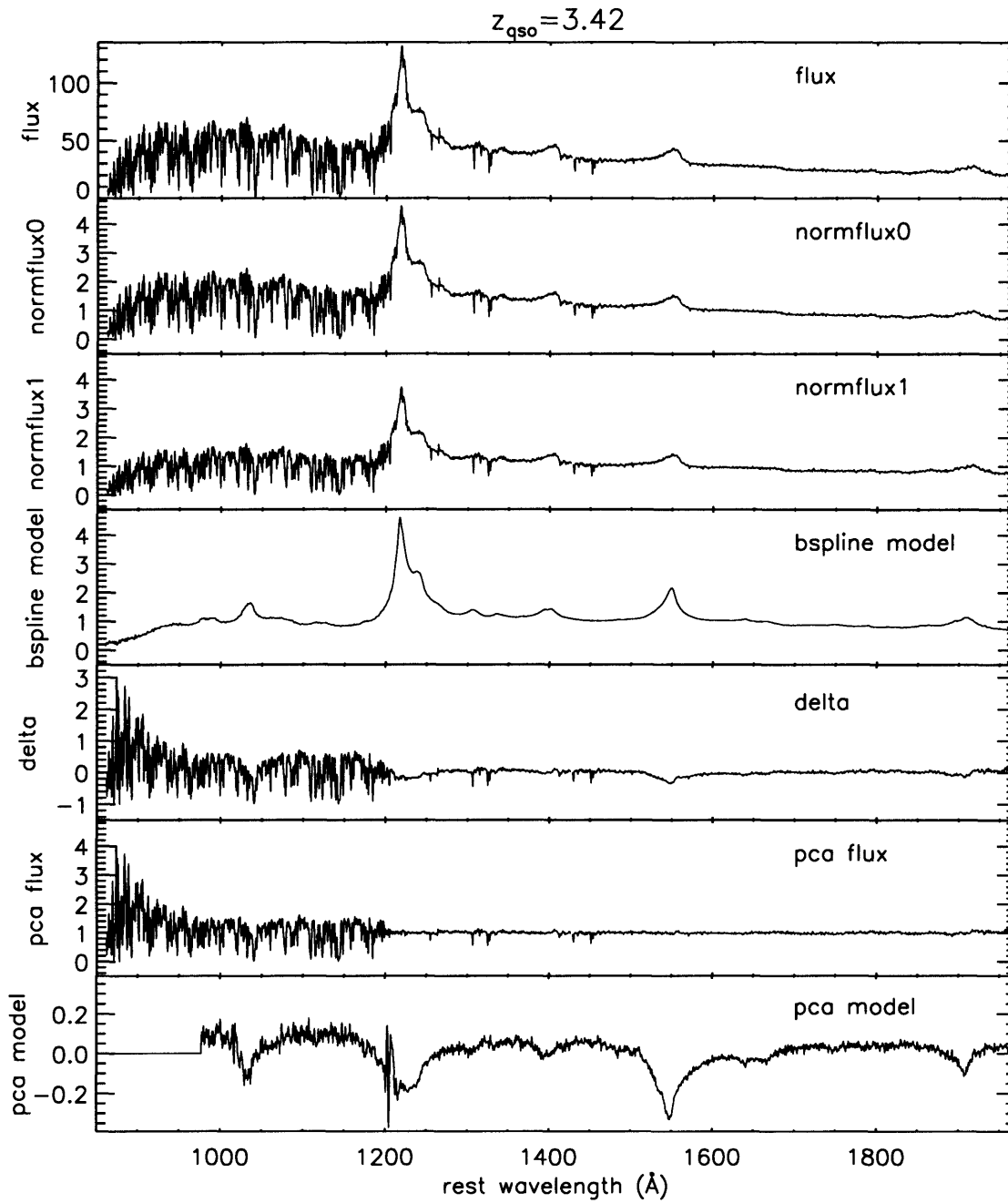


Figure B-4: An example spectrum at each stage in the normalization process.

Bibliography

- K. Abazajian et al. The Second Data Release of the Sloan Digital Sky Survey. *AJ*, 128: 502–512, July 2004.
- Andreas Albrecht and Paul J. Steinhardt. Cosmology for grand unified theories with radiatively induced symmetry breaking. *Phys. Rev. Lett.*, 48:1220–1223, 1982.
- M. Bernardi, R. K. Sheth, M. SubbaRao, G. T. Richards, S. Burles, A. J. Connolly, J. Frieman, R. Nichol, J. Schaye, D. P. Schneider, D. E. Vanden Berk, D. G. York, J. Brinkmann, and D. Q. Lamb. A Feature at $z \sim 3.2$ in the Evolution of the Ly α Forest Optical Depth. *AJ*, 125:32–52, January 2003.
- H. Bi and A. F. Davidsen. Evolution of Structure in the Intergalactic Medium and the Nature of the Ly alpha Forest. *ApJ*, 479:523, April 1997.
- A. S. Bolton, S. Burles, D. J. Schlegel, D. J. Eisenstein, and J. Brinkmann. Sloan Digital Sky Survey Spectroscopic Lens Search. I. Discovery of Intermediate-Redshift Star-forming Galaxies behind Foreground Luminous Red Galaxies. *AJ*, 127:1860–1882, April 2004.
- R. Cen. Testing Cosmological Models with a Ly alpha Forest Statistic: The High End of the Optical Depth Distribution. *ApJ*, 479:L85+, April 1997.
- R. A. C. Croft, D. H. Weinberg, M. Bolte, S. Burles, L. Hernquist, N. Katz, D. Kirkman, and D. Tytler. Toward a Precise Measurement of Matter Clustering: Ly α Forest Data at Redshifts 2-4. *ApJ*, 581:20–52, December 2002.
- M. Dijkstra, A. Lidz, and L. Hui. Beyond Ly α : Constraints and Consistency Tests from the Ly β Forest. *ApJ*, 605:7–13, April 2004.
- N. Y. Gnedin and L. Hui. The Low Column Density Lyman-alpha Forest. *ApJ*, 472:L73+, December 1996.
- A. H. Guth and S. Y. Pi. Fluctuations in the new inflationary universe. *Phys. Rev. Lett.*, 49:1110–1113, 1982.
- Alan H. Guth. The inflationary universe: A possible solution to the horizon and flatness problems. *Phys. Rev.*, D23:347–356, 1981.
- Alan H. Guth and So-Young Pi. The quantum mechanics of the scalar field in the new inflationary universe. *Phys. Rev.*, D32:1899–1920, 1985.
- L. Hui. The Ly- α forest: a cosmic goldmine. In *Evolution of Large Scale Structure : From Recombination to Garching*, pages 368–+, 1999.

- Andrei D. Linde. A new inflationary universe scenario: A possible solution of the horizon, flatness, homogeneity, isotropy and primordial monopole problems. *Phys. Lett.*, B108: 389–393, 1982.
- Andrei D. Linde. Hybrid inflation. *Phys. Rev.*, D49:748–754, 1994.
- P. McDonald, J. Miralda-Escudé, M. Rauch, W. L. W. Sargent, T. A. Barlow, R. Cen, and J. P. Ostriker. The Observed Probability Distribution Function, Power Spectrum, and Correlation Function of the Transmitted Flux in the Ly α Forest. *ApJ*, 543:1–23, November 2000.
- Patrick McDonald et al. The lyman-alpha forest power spectrum from the sloan digital sky survey. 2004.
- A. Nusser and M. Haehnelt. A first step towards a direct inversion of the Lyman forest in QSO spectra. *MNRAS*, 303:179–187, February 1999.
- D. W. Olson. Density perturbations in cosmological models. *Phys. Rev.*, D14:327–331, 1976.
- W. Press, S. Teukolsky, W. Vetterling, and B. Flannery. *Numerical Recipes*. Cambridge University Press, 1992.
- W. H. Press, G. B. Rybicki, and D. P. Schneider. Properties of high-redshift Lyman-alpha clouds. I - Statistical analysis of the Schneider-Schmidt-Gunn quasars. *ApJ*, 414:64–81, September 1993.
- Lisa Randall, Marin Soljatic, and Alan H. Guth. Supernatural inflation: Inflation from supersymmetry with no (very) small parameters. *Nucl. Phys.*, B472:377–408, 1996.
- M. Rauch. The Lyman Alpha Forest in the Spectra of QSOs. *ARA&A*, 36:267–316, 1998.
- D. N. Spergel, L. Verde, H. V. Peiris, E. Komatsu, M. R. Nolta, C. L. Bennett, M. Halpern, G. Hinshaw, N. Jarosik, A. Kogut, M. Limon, S. S. Meyer, L. Page, G. S. Tucker, J. L. Weiland, E. Wollack, and E. L. Wright. First-Year Wilkinson Microwave Anisotropy Probe (WMAP) Observations: Determination of Cosmological Parameters. *ApJS*, 148: 175–194, September 2003.
- N. Suzuki, D. Tytler, D. Kirkman, J. M. O’Meara, and D. Lubin. Relative Flux Calibration of Keck HIRES Echelle Spectra. *PASP*, 115:1050–1067, September 2003.
- M. Tegmark and M. Zaldarriaga. Separating the early universe from the late universe: cosmological parameter estimation beyond the black box. *Phys. Rev.*, D66:103508, 2002.
- D. H. Weinberg. *Cosmology with the lyman-alpha forest*. 1998.
- D. G. York et al. The Sloan Digital Sky Survey: Technical Summary. *AJ*, 120:1579–1587, September 2000.